

**THE APPLICATION OF NMR  
SPECTROSCOPY TO CHARACTERIZATION  
IN CULTURAL HERITAGE**

by

Anna M. Murphy

A dissertation submitted to the Faculty of the University of Delaware in partial fulfillment of the requirements for the degree of Doctor of Philosophy in Chemistry and Biochemistry

Summer 2017

© 2017 Murphy  
All Rights Reserved

**THE APPLICATION OF NMR  
SPECTROSCOPY TO CHARACTERIZATION  
IN CULTURAL HERITAGE**

by

Anna M. Murphy

Approved: \_\_\_\_\_

Murray V. Johnston, Ph.D.  
Chair of the Department of Chemistry and Biochemistry

Approved: \_\_\_\_\_

George H. Watson, Ph.D.  
Dean of the College of Arts and Sciences

Approved: \_\_\_\_\_

Ann L. Ardis, Ph.D.  
Senior Vice Provost for Graduate and Professional Education

I certify that I have read this dissertation and that in my opinion it meets the academic and professional standard required by the University as a dissertation for the degree of Doctor of Philosophy.

Signed:

---

Cecil R. Dybowski, Ph.D.  
Professor in charge of dissertation

I certify that I have read this dissertation and that in my opinion it meets the academic and professional standard required by the University as a dissertation for the degree of Doctor of Philosophy.

Signed:

---

Andrew V. Teplyakov, Ph.D.  
Member of dissertation committee

I certify that I have read this dissertation and that in my opinion it meets the academic and professional standard required by the University as a dissertation for the degree of Doctor of Philosophy.

Signed:

---

Steve Bai, Ph.D.  
Member of dissertation committee

I certify that I have read this dissertation and that in my opinion it meets the academic and professional standard required by the University as a dissertation for the degree of Doctor of Philosophy.

Signed:

---

Silvia A. Centeno, Ph.D.  
Member of dissertation committee

## ACKNOWLEDGMENTS

I would like to thank all who offered help and encouragement as I pursued my doctorate. I would like to thank my undergraduate advisor, Dr. William Dieterle, for his mentorship and encouragement to switch fields of study and to pursue an advanced degree. I thank my graduate advisor, Dr. Cecil Dybowski, for his knowledge and guidance. I would like to thank the other members of my research group, Dr. Fahri Alkan, Dr. Sean Holmes, and Yao Yao. I also thank Dr. Jaclyn Catalano, Dr. Nicholas Zumbulyadis, and Dr. Silvia Centeno for their wisdom on the particulars of ongoing research projects.

I thank the Department of Chemistry and Biochemistry at the University of Delaware for providing an inviting environment for study, research, and collaboration. I thank the members of my dissertation committee for donating their time, insight, and expertise to help me through the doctoral process.

I would like to express heartfelt thanks to my parents, Maryann and Ronald Murphy, and brothers, Darrell, Ronny, and David Murphy, for their continued support throughout my education. Of personal importance, I would like to thank my wonderful fiancé, Joshua Ottaway. His kindness, humor, and unwavering support have served as my greatest source of positivity and a prominent source of motivation through these years.

## TABLE OF CONTENTS

LIST OF TABLES .....	ix
LIST OF FIGURES.....	x
ABSTRACT.....	xv

### Chapter

1	BRIEF INTRODUCTION TO CHEMISTRY AND CULTURAL HERITAGE.....	1
1.1	Pigment Degradation.....	2
1.2	Special Challenges of Analyzing Cultural Heritage Materials.....	4
1.2.1	Materials .....	4
1.2.2	Noninvasive versus Destructive Techniques .....	6
1.3	The Problem of Soap Formation.....	6
1.3.1	Free Fatty Acids .....	8
1.3.2	Transport of Free Fatty Acids and Ions .....	9
1.3.3	The Aggregation of Soaps .....	10
1.4	Application of ssNMR Spectroscopy to Cultural Heritage.....	10
2	SPECTROSCOPIC TECHNIQUES.....	12
2.1	ATR-FTIR Spectroscopy .....	13
2.1.1	Fourier Transform Infrared Spectroscopy .....	13
2.1.2	Attenuated Total Reflectance.....	13
2.2	Single-Crystal X-Ray Diffraction.....	14
2.2.1	Obtaining Crystals.....	15
2.2.2	Checking Crystal Quality.....	15
2.3	Solid State Nuclear Magnetic Resonance Spectroscopy.....	16

2.3.1	General.....	16
2.3.1.1	Energy Levels in a Magnetic Field .....	18
2.3.1.2	Magnetic Shielding .....	19
2.3.1.3	Dipolar Coupling .....	20
2.3.1.4	Vector Model of Excitation and Relaxation Process ...	21
2.3.1.5	Basic Pulse Sequences .....	23
2.3.1.6	Spectrum of a Solid: Observing Chemical Shift Anisotropy .....	25
2.3.2	Carbon-13 NMR Spectroscopy .....	27
2.3.3	Lead-207 NMR Spectroscopy.....	28
2.3.3.1	General .....	28
2.3.3.2	Spin Temperature Alternation .....	30
2.3.3.3	WURST-CPMG Detection.....	30
2.3.3.3.1	Pulse Sequence .....	33
2.3.3.3.2	Analyzing Spectra.....	34
2.3.3.4	Broadband Adiabatic Inversion Cross-Polarization.....	35
2.3.3.5	DNP Enhancement .....	36
2.3.3.5.1	The Solid Effect.....	36
2.3.3.5.2	The Thermal Mixing Effect.....	37
2.3.3.5.3	Application to NMR Pulse Sequences .....	38
2.3.4	Tin-119 NMR Spectroscopy .....	39
3	ANALYSIS OF LEAD SOAPS .....	40
3.1	Preparation of Lead Soaps.....	40
3.2	NMR Spectroscopy of Lead Soaps.....	41
3.2.1	Carbon -13 NMR Spectroscopy .....	42
3.2.2	Lead-207 NMR Spectroscopy.....	45
3.3	FTIR Spectroscopy of Lead Soaps .....	50
3.3.1	Effects of Chain Length in FTIR of Lead Soaps.....	52
3.4	X-Ray Diffraction Analysis of Lead Octanoate .....	53
3.4.1	Synthesis of Lead Octanoate Single Crystals .....	54
3.4.2	Refinement .....	54

4	ANALYSIS OF ZINC SOAPS .....	57
4.1	Introduction .....	57
4.2	Synthesis and Experiment .....	57
4.3	Analysis of Zinc Soaps and ZnO paint .....	58
4.3.1	FTIR Spectroscopy .....	59
4.3.2	Carbon-13 NMR Spectroscopy .....	60
4.4	Implications for Future Work on Zinc Soaps .....	62
5	STUDIES OF PIGMENTS AND MODEL PAINT SYSTEMS.....	63
5.1	Basic Lead White.....	63
5.1.1	Experimental Details .....	65
5.1.1.1	Sample Preparation .....	65
5.1.1.2	Experimental NMR Methods.....	65
5.1.2	Lead Palmitate.....	65
5.1.3	Basic Lead White and DNP NMR Spectroscopy.....	68
5.1.4	DNP NMR Spectroscopy of Paint with Pb Soap Formations .....	72
5.1.5	Conclusions about Lead White Pigment Analysis by DNP- NMR Spectroscopy .....	74
5.2	Lead Tin Yellow Type I.....	75
5.2.1	Experimental Details .....	76
5.2.1.1	Sample Preparation .....	76
5.2.1.2	Experimental NMR Methods.....	76
5.2.1.3	Computational Methods .....	77
5.2.2	Determination of the <sup>207</sup> Pb Chemical-Shift Tensors .....	79
5.2.3	Calculation of <sup>207</sup> Pb Chemical-Shift Tensors .....	82
5.2.4	Determination of <sup>119</sup> Sn Chemical-Shift Tensors .....	84
5.2.5	Reaction of LTY-I with Palmitic Acid .....	86
5.2.6	Conclusions about Lead-Tin Yellow (Type I) .....	88
5.3	Investigating the Effect of Humidity on Soap Formation in Lead White and Zinc White Oil Paints.....	89
5.3.1	Experimental Details .....	90

5.3.1.1	Synthesis and Preparation.....	90
5.3.1.2	Experimental NMR Methods.....	90
5.3.2	A Theoretical Model for Reactive Diffusion in One Dimension	92
5.3.3	Results.....	94
5.3.4	Conclusions about Soap Formation Kinetics in a Paint Film .....	96
6	CONCLUSIONS AND FUTURE DIRECTIONS .....	97
	REFERENCES .....	100
Appendix		
A	PERMISSIONS AND COPYRIGHT .....	111

## LIST OF TABLES

Table 2.1 Main regions of interest in fatty acids and lead soaps <sup>36</sup> .....	13
Table 2.2 Carbon-13 NMR properties <sup>45</sup> .....	28
Table 2.3 Lead-207 NMR properties <sup>45</sup> .....	29
Table 2.4 Tin-119 NMR properties <sup>45</sup> .....	39
Table 3.1 Summary of the <sup>13</sup> C NMR chemical shifts of the lead carboxylates .....	44
Table 3.2 Summary of the chemical-shift tensor components of lead carboxylates....	48
Table 3.3 Experimental details <sup>74</sup> .....	55
Table 3.4 Selected geometric parameters (Å, °) for lead octanoate.....	56
Table 4.1 Assignments of <sup>13</sup> C NMR spectra of (a) Zn octanoate, (b) Zn nonanoate, (c) Zn palmitate, shown in Figure 4.2. (all values in ppm) .....	61
Table 5.1 <sup>207</sup> Pb chemical-shift tensor components (ppm) of basic lead carbonate, determined at 105 K. ....	69
Table 5.2 Selected bond distances (Å) and angles (degree) for the first co- ordination shells of Pb(1) and Pb(2) in Pb <sub>2</sub> SnO <sub>4</sub> .....	80
Table 5.3 Calculated and experimental principal components of the <sup>207</sup> Pb chemical- shift tensors of Pb <sub>2</sub> SnO <sub>4</sub> . ....	83
Table 5.4 Principal components of the <sup>119</sup> Sn chemical-shift tensors of species found in lead-tin yellow I. ....	85
Table 5.5 Normalized mole percentages of lead and tin as determined from SEM- EDS and NMR spectroscopy. ....	86
Table 5.6 NMR signal percentages before and after reaction. ....	87

## LIST OF FIGURES

Figure 1.1 (top) ‘Young Women from the Village’, 1852, by Gustave Courbet. (bottom) Cross-section of a paint sample removed from an area with a bumpy surface texture (indicated by the red arrow in (top)) showing a soap aggregate (~200 $\mu\text{m}$ in diameter) breaking through the dark paint surface. ....	7
Figure 2.1 Schematic depiction of the ATR sample for performing FTIR spectroscopy. ....	14
Figure 2.2 Image of lead octanoate crystals under cross-polarized light. The rainbow effect results from several needle-like crystals overlapping. ....	16
Figure 2.3 Energy diagram for a spin- $\frac{1}{2}$ nucleus, the most commonly studied with NMR ( $^1\text{H}$ , $^{13}\text{C}$ , $^{15}\text{N}$ , $^{31}\text{P}$ ). The energy gap depends on the particular nucleus. Some nuclei, such as $^1\text{H}$ , have a higher spin which corresponds to a higher energy splitting in a given magnetic field. Because of this fact, one can generally examine only a particular nuclear species in a single experiment, which makes the experiment more specific than other kinds of spectroscopy. ....	18
Figure 2.4 Vector diagram for the alignment of the bulk magnetization with the external magnetic field. ....	21
Figure 2.5 1D NMR spectroscopy pulse sequence. ....	24
Figure 2.6 1D experiment for detecting $^{13}\text{C}$ nuclei while decoupling $^1\text{H}$ . ....	24
Figure 2.7 Simplest cross-polarization pulse sequence. ....	25
Figure 2.8 The electronic distribution around a nucleus is described by three distinct axes [left]. Each corresponds to a distinct chemical shift [center]. When spinning at the magic angle, the spectrum collapses into multiple peaks [right] .....	26
Figure 2.9 Spin-temperature alternation (STA) NMR pulse sequence. ....	30

Figure 2.10 Excitation profile for a square 90° pulse (blue), overlain with the typical spectral range for <sup>13</sup> C (red) and a possible range for a single <sup>207</sup> Pb signal (green) .....	31
Figure 2.11 Two <sup>207</sup> Pb STA-MAS NMR spectra of lead azelate collected with the center of excitation at -1000 ppm (blue) and -2200 ppm (red). .....	32
Figure 2.12 Methods of collecting spectra for ultra-widelines include(a) using a sum (blue) of a series of excitation profiles (red) and (b)fitting a theoretical lineshape (blue) to data points of the summation of the echo train from spectra at various excitation frequencies. ....	33
Figure 2.13 WURST-CPMG NMR pulse sequence for broadband excitation. ....	33
Figure 2.14. Excitation shape (red) for WURST-CPMG NMR pulse sequence. ....	34
Figure 2.15 Example of fitting of lead azelate with (a) STA-MAS at 10 and 12 kHz spinning and (b) WURST-CPMG spectra. The final fit shown in (c). ..	35
Figure 2.16 BCP pulse sequence.....	36
Figure 2.17 Electron-nuclear spin energy levels and transitions. ....	37
Figure 2.18 Diagram of the thermal mixing mechanism.....	38
Figure 2.19 Pulse sequence for application of DNP enhancement during the (a) STA/MAS and (b) BCP pulse sequences. ....	38
Figure 3.1 <sup>13</sup> C NMR spectra of (a) lead octadecanoate, (b) lead hexadecanoate, (c) lead undecanoate, (d) lead decanoate, (e) lead nonanoate, (f) lead octanoate, (g) lead heptanoate, (h) lead hexanoate. ....	42
Figure 3.2 Comparison of spectra obtained with direct excitation, STA/MAS at 12 kHz (a and c) with spectra of nonspinning samples obtained with the WURST-CPMG sequence (b and d) for lead palmitate (a and b) and lead stearate (c and d). Each spectrum also shows the simulated fit for the tensor. The decreases in intensity at the centers of (b) and (d) are a result of a spectral artifact due to the placement of the carrier frequency. ....	45
Figure 3.3 <sup>207</sup> Pb NMR spectra of (a) lead octadecanoate, (b) lead hexadecanoate, (c) lead undecanoate, (d) lead decanoate, (e) lead nonanoate, (f) lead octanoate, (g) lead heptanoate, (h) lead hexanoate. ....	46

Figure 3.4 Illustration of the (a) hemi directed and (b) holo directed structures predicted by Shimoni-Livney. ....	50
Figure 3.5 FTIR spectra of (a) palmitic acid, (b) lead palmitate, a basic lead white paint film as (c) a protrusion in the film and (d) the sample paint sample crushed under liquid nitrogen. ....	51
Figure 3.6 Spectra of (a) lead octadecanoate, (b) lead hexadecanoate, (c) lead undecanoate, (d) lead decanoate, (e) lead nonanoate, (f) lead octanoate, (g) lead heptanoate, (h) lead hexanoate. ....	52
Figure 3.7 Molecular diagram with 30% probability ellipsoids. Hydrogen atoms depicted with arbitrary radius. ....	54
Figure 3.8 Pb coordination environment with 30% probability ellipsoids. Symmetry codes: (i) $x+1, y, z$ ; (ii) $-x+1, -y+1, -z+1$ ; (iii) $-x+1, -y, -z+1$ . ....	56
Figure 4.1 FTIR spectra of (a) Zn palmitate, (b) Zn nonanoate, (c) Zn octanoate. ....	59
Figure 4.2 $^{13}\text{C}$ NMR spectra of (a) Zn palmitate, (b) Zn nonanoate, (c) Zn octanoate. ....	60
Figure 4.3. Carbon-13 NMR spectra of ZnO paint reacting with palmitic acid (a) just after mixing, (b) after substantial reaction, and (c) near the end of reaction. ....	61
Figure 5.1 Structure of basic lead white <sup>81</sup> , showing (a) the layered structure of (b) layer A – lead carbonate and (c) layer B – lead hydroxide. ....	64
Figure 5.2 $^{207}\text{Pb}[^1\text{H}]$ CPMAS (a) and $^{207}\text{Pb}[^1\text{H}]$ BCP (b) spectra of lead palmitate, acquired with microwave radiation on and off. In contrast to lead white, the spectra could be easily acquired without stepping the carrier frequency. Simulated lines for the DNP-CPMAS and DNP-BCP spectra are shown at the top. In (a) the MAS rate was $\nu_R = 10$ kHz, the contact time was 10 ms, and 256 scans were acquired with a recycle delay of 8 s; in (b) the adiabatic pulses used for CP and CPMG refocusing were the same as those used for lead white, and 64 scans were acquired with a recycle delay of 8 s. ....	66

- Figure 5.3.  $^{207}\text{Pb}$  SSNMR spectra of lead white. (a)  $^{207}\text{Pb}[^1\text{H}]$  DNP-BCP spectrum (bottom) and its simulated decomposition into signals assigned to the Pb1 and Pb2 sites. The adiabatic inversion (CP) pulse swept over 250 kHz for a period of 20 ms while the refocusing CPMG pulses lasted 50  $\mu\text{s}$  and was swept over 500 kHz. The experimental line shape is composed of eight subspectra, each measured with 64 scans and a recycle delay of 6 s. A single subspectrum acquired with and without the application of microwaves is shown in (b). (c)  $^{207}\text{Pb}$  WCPMG spectrum featuring solely the lead carbonate resonance. This spectrum was acquired at 308 K, using 128 scans and a recycle delay of 8 s. .... 68
- Figure 5.4 The  $^{207}\text{Pb}[^1\text{H}]$  DNP-BCP build-up curves as a function of the CP contact time, measured for the Pb1 and Pb2 sites at 110 K. .... 70
- Figure 5.5 Sections of the  $^{207}\text{Pb}$  WCPMG (a) and  $^1\text{H}$  spin echo (b) spectra of lead white measured at different temperatures. All  $^{207}\text{Pb}$  spectra were obtained using the same conditions as in Figure 5.3, with a recycle delay of 15 s and a greater number of scans: 256 scans at 110 K, 165 K, and at 308 K, 512 scans at 226 K, and 768 scans at 255 K. The  $^1\text{H}$  spin echo spectra were obtained under a static condition, with a half-echo period of 50  $\mu\text{s}$ , a recycle delay of 15 s and 16 scans. The spectra in each column (with the exception of basic lead carbonate at 308 K) were normalized to constant height to eliminate the effect of the varying numbers of scans, Boltzmann polarizations,  $T_1$  relaxation times and RF efficiencies at the different temperatures. .... 72
- Figure 5.6 (a)  $^{207}\text{Pb}[^1\text{H}]$  DNP-BCP spectrum of aged paint film measured at 108 K. Subtracting the signals from lead white results in spectrum (b), revealing the signal from the decomposition products; the arrow shows the signal corresponding to a lead soap. The pulse parameters were identical to those used for lead white, described in Figure 5.3. .... 74
- Figure 5.7 Molecular clusters of lead-tin yellow employed in the computational investigations, lead (dark gray), oxygen (red) and tin (light gray). Cluster I (a) and cluster II (b). .... 78
- Figure 5.8 Structure of  $\text{Pb}_2\text{SnO}_4$  showing the coordination environment around the (a) lead (dark gray) and (b) tin (light gray) sites. Oxygen is shown in red. Pb(1) and Pb(2) are structurally similar, and both would have similar environments with slight differences in bond lengths and bond angles. .... 79

Figure 5.9 (a) Simulated spectrum for each of the individual components in the sample; $\text{Pb}_2\text{SnO}_4$ (blue and green) and the impurity minium (red). (b) $^{207}\text{Pb}$ spectrum of LTY-I obtained with WURST-CPMG, showing four lead species. (The low intensity, $\text{Pb}^{4+}$ , site of minium is assumed based on the presence of the $\text{Pb}^{2+}$ site and the previously published spectrum.) .....	81
Figure 5.10 Experimental $^{119}\text{Sn}$ STA/MAS with proton decoupling spectrum (red) of the LTY-I sample recorded on a 500 MHz magnet, showing unreacted starting material $\text{SnO}_2$ . The percentages of the two tin species were determined using MAS simulations in WSOLIDS with $64\pm 2\%$ for $\text{Pb}_2\text{SnO}_4$ (green) and $36\pm 2\%$ for $\text{SnO}_2$ (blue). .....	85
Figure 5.11 NMR spectra of the LTY-I paint film containing free palmitic acid. (a) $^{13}\text{C}$ MAS NMR spectrum, showing lead palmitate formation by the appearance of peaks at 182.6 and 183.8 ppm. (b) $^{207}\text{Pb}$ WURST-CPMG spectrum, showing in addition to $\text{Pb}_2\text{SnO}_4$ , lead palmitate ( $\delta_{\text{iso}} = -2131$ ppm) and minium ( $\delta_{\text{iso}} = -1102$ ppm). .....	87
Figure 5.12 $^{119}\text{Sn}$ STA/MAS NMR spectra of LTY-I before (red) and after reaction (blue) with palmitic acid in a paint film. ....	88
Figure 5.13 $^{13}\text{C}$ CPMAS spectra (red) of (1) lead palmitate and (2) palmitic acid (A) at the beginning and (B) after the reaction has progressed for one day, with fits (purple) and residuals (pink). ....	91
Figure 5.14 A schematic representation of the geometry assumed for the one-dimensional diffusion model. Where a mobile species (orange) sits on the surface of a paint particle or film (blue line) and must diffuse in to react.....	92
Figure 5.15 The formation of lead or zinc soaps in a sample containing lead white (circles) or zinc white (squares), when exposed to palmitic acid. Experiments were conducted at relative humidities of 90% (red), 60% (purple), and 0% (blue). ....	95
Figure 5.16 The formation of lead palmitate in a paint sample containing lead white, when exposed to palmitic acid at a relative humidity of 60%. The experimental points graphed by amplitude in arbitrary units (with the axis scaled as 100%). The green line is the theoretical dependence of amount of lead palmitate given in equation (11). ....	96

## ABSTRACT

Soap formation in traditional oil paintings occurs when heavy-metal containing pigments, such as lead white,  $2\text{PbCO}_3 \cdot \text{Pb}(\text{OH})_2$ , lead tin yellow type I,  $\text{Pb}_2\text{SnO}_4$ , and zinc oxide,  $\text{ZnO}$ , react with fatty acids in the binding medium. These soaps lead to transparency of paint layers and may form aggregates which protrude through the paint surface damaging the integrity of the artwork. The factors that trigger soap formation and the mechanism(s) of the process are not yet well understood. To elucidate these issues, chemical and structural information is necessary, which can be obtained using solid-state nuclear magnetic resonance (ssNMR) spectroscopy.

Despite their versatility, only a few single-crystal X-ray structures of lead carboxylates exist, due to difficulties with solubility. In particular, the structures of long-chain metal carboxylates have not been reported. There are two types of coordination geometry around lead centers, based on whether the lone electron pair in  $\text{Pb}(\text{II})$  is stereochemically active or inactive. These geometries are commonly referred to as hemidirected and holodirected structures. By studying a series of lead carboxylates, ranging from lead hexanoate (C6) to lead hexadecanoate (C18), with  $^{13}\text{C}$  and  $^{207}\text{Pb}$  solid-state NMR and infrared spectra, and single-crystal X-ray diffraction of two soaps, the series can be divided in two groups based on chain length.

In more modern paintings, due to concerns about toxicity, zinc white eventually replaced lead white as the common base pigment and filler. It was later discovered that zinc white also reacts with oil binders, forming soaps which often

leads to brittle paint which tends to flake. Initial measurements of FTIR and  $^{13}\text{C}$  NMR spectra were performed on several zinc soaps to gain insight into their structure.

The basic lead white pigment has proven challenging to observe by NMR spectroscopy using traditional techniques. Dynamic nuclear polarization (DNP) is used here to enhance the ultra-wideline  $^{207}\text{Pb}$  solid-state NMR spectra, enabling, for the first time, detection of the basic lead carbonate phase of lead white pigment. Variable-temperature experiments revealed that the short relaxation time of the basic lead carbonate phase hinders the acquisition of the NMR signal at room temperature. The DNP enhancement is twice as large for lead palmitate as it is for the basic lead carbonate, permitting detection of the formation of a lead soap in an aged paint film by  $^{207}\text{Pb}$  ssNMR spectroscopy; which may aid in the detection of deterioration products in smaller samples removed from works of art.

Lead–tin yellow type I (LTY-I) has been used by artists from at least the early 15<sup>th</sup> century until the early 18<sup>th</sup> century, which has also been linked to soap formation.  $^{119}\text{Sn}$  and  $^{207}\text{Pb}$  ssNMR spectroscopy were used to characterize the pigment. A combination of NMR techniques and DFT molecular cluster calculations, allowed identification of the individual species in LTY-I and determine their  $^{119}\text{Sn}$  and  $^{207}\text{Pb}$  chemical-shift tensors. The presence of starting materials from the synthesis, minium and tin(IV) oxide, was also verified. Knowledge of the chemical-shift tensor components and the impurities in LTY-I is important for examining the chemistry of degradation processes and soap formation. ssNMR was used to detect reaction between  $\text{Pb}_2\text{SnO}_4$  and added palmitic acid in a model paint sample containing LTY-I.

Finally,  $^{13}\text{C}$  NMR was used to track the formation of lead soaps in a basic lead white paint film under different humidity conditions. Initial fits suggest this process is

diffusion-driven and the reactive event is a first-order reaction, based on the reaction profile tracked over the course of several days.

Modern techniques in solid-state NMR spectroscopy has provided new insights into the local lead geometries in lead soap formations and the reaction process.

## Chapter 1

### **BRIEF INTRODUCTION TO CHEMISTRY AND CULTURAL HERITAGE**

As cultural heritage objects age, they undergo many complex changes that can affect the appearance and structural integrity of the artwork. These changes provide difficult and interesting challenges that require the development and application of new analytical techniques to address preservation properly, without compromising the integrity of the works.

There are many types of degradation that happen as paintings age, some of which are more easily addressed than others. There are mechanical breakdowns such as scratches and tears that occur primarily during moving, which require chemical knowledge of the artwork to fix, effectively to ensure the new materials used are compatible with the old and, as the painting continues to age, will change consistently with the original materials. Physical changes like cussing, where the edges of paint curls up along cracks, and blooms, where cloudy areas appear in the varnish, result from paintings being stored at too low or too high of a humidity level. Even surface grime can cause major issues if it sits for too long, as - over time - it can be absorbed into the surface of the painting and become chemically bound. There are color changes that occur as a result of pigments reacting with the environment. One major problem, common on paintings from the 15<sup>th</sup> to 20<sup>th</sup> century, is the formation of lead soaps which can cause loss of color, transparency, and loss of structural integrity of the paint.

There has been some controversy over what level of intervention is appropriate for the preservation of artwork. Because the value of artwork extends beyond just aesthetic creations, e. g. because they may also be historic objects, there is a desire to preserve some of the changes that occur naturally from aging. An older perspective from Sir George Beaumont, instrumental in the establishment of the National Gallery due to his generous donations<sup>1</sup>, claims

“A good painting, like a good violin, should be brown.”<sup>2</sup>

Some believe these changes that come from age, such as craquelure and discoloration, are an important aspect of the artwork and different levels of degradation are accepted for paintings from different eras<sup>2</sup>. There is little acceptance of large losses from flaking and powdering (friable paint<sup>1</sup>; resulting from insufficient binder). The aspiration to preserve the desirable aspects of aging, while preventing and reversing some aspects, makes the works of art conservators much more complicated.

### **1.1 Pigment Degradation**

Heavy metal pigments used in traditional oil paintings can undergo many changes as they age. Studies have been conducted on a wide range of pigments in attempts to determine the root causes so that environmental changes can be made to stop, or at least slow, these reactions.

The copper pigment azurite, a naturally occurring deep-blue mineral, is left coarse during paint application, as fine grinding increases the index of refraction, resulting in a paler color<sup>3</sup>. The coarse-particle preparation leaves uneven surfaces that can absorb other chemicals, leading to higher reactivity. Azurite is sensitive to acids, such as the fatty acids found in oil paints, causing it to oxidize, turning to green malachite over time<sup>3</sup>. It can also blacken as it oxidizes into tenorite (CuO) as a result

of light exposure when it is more finely ground<sup>4</sup>. When used on documents, azurite pigments turn the paper and make the support brittle<sup>5</sup>, making it difficult to handle historic documents without loss of material.

Studies of chrome yellow pigments by ultraviolet and visible spectroscopy (UV-Vis), Fourier transform infrared spectroscopy (FTIR), and micro X-ray absorption near edge spectroscopy ( $\mu$ -XANES) show that high humidity and temperature have a strong effect on the photo-degradation of Cr(II) to Cr(III)<sup>6</sup>. Cadmium yellow pigments can lighten or darken in different parts of a single painting, such as in Henri Matisse's *Le Bonheur de vivre*<sup>7</sup>. The discolored regions of the painting were studied with  $\mu$ -XANES and FTIR and it was found that areas that darkened by hydrolysis of the oil binder due to acid formed during photodegradation (high CdCl<sub>2</sub>), and that lightened areas resulted from CdSO<sub>4</sub> reacting with CO<sub>2</sub> in the air to form CdCO<sub>3</sub><sup>7</sup>. The Matisse degradation is an example in which the use of commercial paints with complex mixtures of pigments complicates the analysis and degradation of artwork.

There are many examples of lead-based pigments degrading in artwork. Red lead, one of the earliest synthetic pigments, has been shown to convert into lead carbonate when mixed with organic binders<sup>8</sup> and into lead sulfide when in the presence of atmospheric sulfur dioxide<sup>8b</sup>. Lead white, one of the most common pigments in traditional oil paintings, undergoes degradation when irradiated with a laser<sup>9</sup>. The study of photodegradation processes that may happen under this condition is important as use of lasers to clean unwanted surface layers off of artwork has become more popular. The process can reduce the lead white pigment to metallic lead, darkening the artwork.

The broad range of degradation processes possible, all of which are exacerbated under different conditions, makes the appropriate manner of caring for artwork much more complicated. The attempt to remove one form of degradation may contribute to another process, making a very complex chemical problem for conservationists.

## **1.2 Special Challenges of Analyzing Cultural Heritage Materials**

### **1.2.1 Materials**

A wide range of materials is used in the creation of artwork, and artwork has not always been stored and maintained in a consistent manner, making it more difficult to create plans for addressing concerns that will be successful for many works.

Different supports were used, which contribute to the challenges. A range of types of canvas (linen, cotton, hemp, etc.<sup>10</sup>) leads to different textures, some of which absorb excess oil during preparation. A variety of woods have been used, such as European poplar (common in Spain, Italy, and southern Germany<sup>11</sup>) and baltic oak, common in Netherlands, northern France, and Germany<sup>12</sup>. Different types of wood age differently and some produce organic gases<sup>13</sup> as they degrade or contain moisture. Wood supports can even age differently based on what cut of wood is used.

The ground layer of a painting is used to create a uniform base color and a smooth surface. In early work in Italy, the ground layer was commonly prepared as a mixture of animal glue (collagen extracted from animal tissues) and gypsum ( $\text{CaSO}_4 \cdot 2\text{H}_2\text{O}$ ), sometimes with oil<sup>10</sup>. Frequently, large-particle-size gypsum was used as a first layer, topped with layers made from finer ground particles to smooth the

surface. The thickness of the layer, the purity of materials, and the ratio of protein to oil can be seen to vary from work to work. In some works, a red clay base (iron minerals give the color) was used to smooth the surface of the canvas and was covered with a lead white and oil paint to seal it<sup>14</sup>.

Until recently, with modern consistent standards for commercially available paints, artists would often produce their own paint, using their own recipes. Since paints were prepared as used, they vary in composition between batches, even within the same piece. The pigments used by an artist may vary among his/her works either because of the unique production of materials by the artist or because the materials commercially available to the artist are inconsistently produced.

Pigments were traditionally sourced from clays and minerals. Early synthesized pigments include lead white ( $(\text{PbCO}_2)_2\text{PbOH}$ ), red lead ( $\text{PbO}_3$ ), vermilion ( $\text{HgS}$ ), verdigris ( $\text{Cu}(\text{C}_2\text{H}_3\text{O}_2)_2$ ), and lead tin yellow ( $\text{Pb}_2\text{SnO}_4$ ). Early dyes were sourced from things such as insect shells (lac dye from the insect *Laccifer lacca*<sup>15</sup>) or wood (brasilin from brazilwood<sup>16</sup>). Various methods were used for extraction, including precipitation with alum, to create usable pigments. Oils used to make paints might have been sourced from walnut, poppyseed, safflower, or flax (linseed oil) to compose the binder<sup>10</sup>. All oils darken over time, but they have different appearances upon initial drying. Linseed oil is often used as a drier, even if it is not the main oil used. It has a higher concentration of unsaturated fats than others, allowing it to crosslink more effectively. Lead white is often added as a drier in oil paints because the lead acts as a catalyst for the oxidation process<sup>10</sup>.

### **1.2.2 Noninvasive versus Destructive Techniques**

An additional complication to the process of studying art objects for conservation is the desire to minimize damage. Many analytical techniques that could answer complex questions are rejected by the conservation community because they require the removal and/or destruction of large samples of material. There is a strong preference for techniques that can be performed *in situ*, or at the very least require the removal of only very tiny samples (cross-sections taken are near a half millimeter wide) that can be measured by several techniques in series. This limitation requires the development innovative techniques for the examination of cultural heritage materials.

### **1.3 The Problem of Soap Formation**

One of the many degradation processes affecting paintings is the formation of heavy-metal soaps. Paintings, dating from the 15<sup>th</sup> through the 20<sup>th</sup> centuries, are affected by the formation of heavy-metal soaps which alter the structural integrity and appearance of the artwork<sup>17</sup>. The overall process involves: (1) the production of free acids, (2) the transport of the free acids or metal ions through the paint matrix, (3) the reactive event, and (4) the aggregation of soap molecules.

For example, in Gustave Courbet's painting '*Young Women from the Village*' (Figure 1.1 top), a Raman spectrum recorded in an inclusion visible in a paint sample removed from an area that presents a granular surface texture (Figure 1.1 bottom) showed the presence of lead carboxylates.



Figure 1.1 (top) 'Young Women from the Village', 1852, by Gustave Courbet.  
(bottom) Cross-section of a paint sample removed from an area with a bumpy surface texture (indicated by the red arrow in (top)) showing a soap aggregate (~200  $\mu\text{m}$  in diameter) breaking through the dark paint surface.

Soap formation is not restricted to oil paintings; long-chain fatty acid carboxylates of lead, copper, and zinc have been found as degradation products on the surfaces of metallic cultural artifacts, as a result of treatments or contact with organic substances such as animal fats, oils, or leather<sup>18</sup>. They have also been found in ancient pharmaceutical products<sup>19</sup>.

The formation of soaps does not take place in all artworks containing potentially reactive materials. Various theories have suggested that this phenomenon may result from peculiarities inherent in the artist's materials and techniques, from conservation procedures, or from the object's exposure to environmental conditions such as high relative humidity and temperature<sup>17b, 20</sup>. Even though progress has been made in understanding soap formation<sup>20d, 21</sup>, the factors that trigger the process of soap formation, what the mechanisms are, and how the processes can be arrested or prevented are not completely known.

### **1.3.1 Free Fatty Acids**

Linseed oil, the binding medium most frequently used in traditional oil paintings, is composed mainly of triglycerides, triesters of glycerol with various fatty acids. Linseed oil is also used in industrial applications for manufacturing capsules to heal microcracks in epoxy coatings, in alkyl-based paints, as a protective wood coating, as a varnish, in plasticizers, and in the manufacturing of linoleum rubber<sup>22</sup>. The acyl chains in linseed oil correspond primarily to the polyunsaturated C18 fatty acids containing two (linoleic) and three (linolenic) double bonds and, to a lesser extent, one double bond (oleic) and to the saturated C16 (palmitic) and C18 (stearic) acids<sup>23</sup>. As linseed-oil-based paint films age, the glycerides hydrolyze and the initial auto-oxidation of the polyunsaturated fatty acids results in the formation of

hydroperoxides. The hydroperoxides subsequently decompose to yield highly reactive free radicals and eventually cross-links between the fatty chains that consist of C-C and C-O-C bonds. Gradual hydrolysis of the glycerol ester linkages ultimately leads to the formation of an ionomeric matrix of cross-linked alkyl chains with pendant carboxylic acid groups<sup>23b, 24</sup>. The saturated C16 and C18 fatty acid components of a triglyceride cannot undergo cross-linking reactions, instead they are released into the paint matrix, migrate, and react with the heavy metals from the pigments.

### **1.3.2 Transport of Free Fatty Acids and Ions**

Through transport phenomena that are not yet understood, the free fatty acids in the oil binders migrate through the paint film and react with the heavy-metal-containing pigments, such as  $2\text{PbCO}_3 \cdot \text{Pb}(\text{OH})_2$  (lead white) or  $\text{Pb}_2\text{SnO}_4$  (lead-tin yellow type I), to form metal carboxylates.

There is accumulating evidence that aged linseed oil films in oil paintings can be treated as cross-linked ionomeric networks. Tumosa et al.<sup>25</sup> have synthesized ionomers with controlled architecture by adding known amounts of unsaturated free fatty acids to linseed oil, followed by cross-linking at 40-50% RH at ambient temperature for 3.75 years. They have shown that cross-linked ionomeric structures closely mimic the physical and chemical properties of aged paint films. Absorbed water, ions from pigments, free mono- and diacids, carboxylates, potentially free glycerol, and organic solvents can move within this ionomeric matrix.

Two mechanisms for transport in ionomeric materials have been identified<sup>26</sup>. The most prevalent transport mechanism is water-mediated transport<sup>27</sup>, where the motion of ions and small molecules is facilitated by the motion of water. This mechanism is encountered in ion-conducting membranes like Nafion®. The other

mechanism is polymer-mediated ion transport, which is related to the flexibility of the side chains associated with the ions. This behavior has been reported for  $\text{Li}^+$  and  $\text{Na}^+$  ion conductors made of PEO-polyurethane ionomers<sup>28</sup>. A similar mechanism has been proposed for acrylic paint mixtures with polyethylene glycol (PEG), exposed to temperatures above the glass transition temperature of acrylate materials ( $T_g=12^\circ\text{C}$ ) and below the melting point of PEG ( $50^\circ\text{C}$ ), in which the PEG chains move through the matrix until they encounter a nucleation site<sup>29</sup>.

### **1.3.3 The Aggregation of Soaps**

Migration of metal soaps leads to aggregation and the appearance of soap protrusions through the surface of the paintings or to an increased transparency of the paint films, causing the preparatory drawing, the wood or canvas support, and/or the artist's alterations to become visible to the naked eye<sup>17e, 20b, 30</sup>.

Lead soaps may also migrate to the surface of a painting, where they form disfiguring crusts composed of lead carbonates, hydroxychlorides, sulfates, and/or oxalates, presumably by reacting with carbon dioxide and other compounds in the environment<sup>17b, 17d, 20b, 31</sup>. Understanding the mechanism of metal soap formation and particularly the role of migration of different species is a major issue in maintaining the integrity of the world's cultural heritage.

## **1.4 Application of ssNMR Spectroscopy to Cultural Heritage**

Liquid-state NMR spectroscopy has been used to study extractable components of artwork<sup>32</sup>. It has the benefit of working with low concentrations, as is needed with cultural heritage samples, but it has the weakness that only the soluble components of a sample can be studied, rather than all components in the mixture. It also destroys the

sample by saturating it with some solvent and removing relevant materials, so that it can no longer be used for additional analysis by other techniques.

Single-sided NMR, such as obtained with the NMR-MOUSE (mobile universal surface explorer, a registered trademark of RWTH Aachen) allows portable  $^1\text{H}$  NMR measurements in an inhomogeneous magnetic field. It has provided information on diffusion of water in diverse types of materials. In particular, single-sided NMR measurements of water diffusion in acrylic paint films, wall paintings, and other model systems have provided insight into important conservation issues<sup>33</sup>. The NMR-MOUSE<sup>®34</sup> can also measure spin relaxation, which is related to the local dynamics of water in a material. Because it generates depth profiles with a spatial resolution of less than 10  $\mu\text{m}$  up to depths of 25 mm, it can give spatial information about the dynamics<sup>35</sup>.

Solid-state nuclear magnetic resonance (NMR) spectroscopy provides insight into the structure and dynamics of materials, making it an excellent technique for investigating the materials that compose these complex systems. It suffers from low sensitivity, which is especially difficult in the study of nuclei with wide lines, such as lead. Innovative modern experiments can be used to overcome the inherent challenges of these materials as well as instrumental and time limitations.

## Chapter 2

### SPECTROSCOPIC TECHNIQUES

Fourier transform infrared (FTIR) spectroscopy is a popular technique for analysis of paint materials due to high sensitivity, ease of measurement, and options available for non-invasive or minimally invasive measurements. In this work, it is used as a complementary technique to the nuclear magnetic resonance (NMR) spectroscopy.

The crystal structure of materials has a strong impact on their reactive and dynamic properties. One of the early goals of this work was determining the crystal structure of lead soaps. Single-crystal x-ray diffraction gives a high level of detail about the crystal structure of materials, when it is possible to grow a single crystal.

When single crystals cannot be obtained for a material, the structure can be inferred by other means. Solid-state NMR spectroscopy provides a wealth of information about the structure of materials and dynamics in materials. It has not been applied extensively in cultural heritage research due to sample limitations and the need for complex programs for observing certain nuclei. The development of innovative modern experiments allows us to detect interesting trends in materials that would be too difficult to measure by traditional techniques.

## 2.1 ATR-FTIR Spectroscopy

### 2.1.1 Fourier Transform Infrared Spectroscopy

Fourier transform infrared (FTIR) spectroscopy is used to observe the fundamental rotational and vibrational modes of a material. Molecules absorb light at a frequency that matches the vibrational frequencies of its bonds. These energies are most affected by the strength of the bonds and masses of the atoms, allowing certain energy ranges to be commonly associated with certain functional groups. Using palmitic acid as an example, the carboxyl group stretching vibration shifts when it binds to lead, so this can be used as a quick, easy method to check sample purity after synthesis.

Vibrational modes appear in IR when the vibration changes the dipole moment of the molecule. The types of motion involved in IR-active vibrations include: symmetric and antisymmetric stretching, wagging, rocking, twisting, and scissoring. Some common absorbance bands in FTIR of fatty acids are listed in Table 2.1.

Table 2.1 Main regions of interest in fatty acids and lead soaps<sup>36</sup>

Absorption band (cm <sup>-1</sup> )	Assignment
1750	Asymmetric carboxyl stretch, Fatty acid
1515-1540	Asymmetric carboxyl stretch, Lead carboxylate
~720	CH <sub>2</sub> rocking mode
1150-1350	Wagging, twisting in hydrocarbon chain

### 2.1.2 Attenuated Total Reflectance

Attenuated total reflectance is a sampling method used with FTIR that allows samples to be measured in the solid state without special preparation. In this method,

the beam of infrared light passes through the sample stage crystal at an angle that causes the light to reflect off of the sample surface, creating an evanescent wave. (Figure 2.1.) The reflected light beam is collected by the detector after exiting the crystal. The crystal used must have a higher refractive index than the sample material, a common choice being zinc selenide, and the sample material must be kept in close contact with the crystal surface.

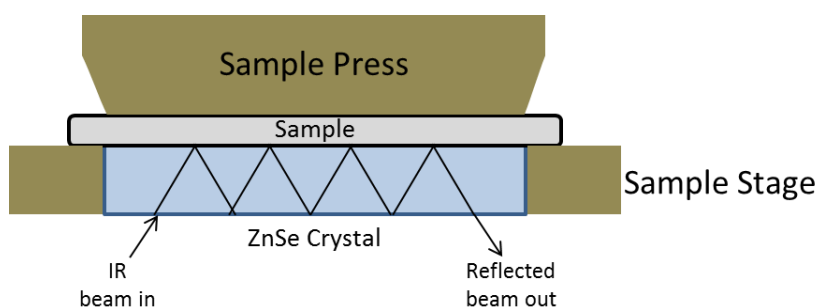


Figure 2.1 Schematic depiction of the ATR sample for performing FTIR spectroscopy.

## 2.2 Single-Crystal X-Ray Diffraction

Structure has important impacts on freedom of movement and reactivity of materials. Crystal structure can vary significantly, even if materials are similar in stoichiometry. Single-crystal X-ray diffraction (XRD) is commonly used to determine crystal structure because it provides detailed information about the connectivity in a molecule, including bond lengths and angles, as well as the geometry of repeating patterns of molecules in the structure of the solid. It uses the pattern of light diffracted off atoms in a crystal to determine the repeating molecular unit. The intensity of light diffracted at each angle is used to produce a three-dimensional picture of the electron density of a solid.

### **2.2.1 Obtaining Crystals**

Frequently when crystals form, several grow together, but with random directions of the crystal axes. X-ray analyses of such materials are not useful because this gives an incoherent picture of the solid being analyzed. A single crystal is required to get a coherent diffraction pattern that represents the true structure of the solid, including the structure of the molecule. There are many methods for growing single crystals, each having its own level of difficulty and success. The success in growing single crystals is dependent of a wide variety of factors including: solvents used, concentration of solute, surface area of crystallization vessel, speed of evaporation and heating, temperature of the room, etc. Determining which conditions works best is only determined by having grown the crystal and requires a bit of luck.

For materials that don't crystallize well, such as long-chain fatty acids, crystals form best by slow evaporation. In this case, the solute is not generally highly soluble in the solvent. The solution is prepared by mixing slightly more solvent than is necessary to dissolve all of the solute. As the solvent evaporates, it no longer holds all of the solute, which allows the solute to start crystalizing. If this process happens sufficiently slowly, the molecules form a single crystal. On the other hand, if this process happens too quickly, the molecules "crash out" of solution as a powder. During crystallization, samples must be left undisturbed, as mixing changes molecular orientation and results in the formation of powdery precipitates or twinned crystals.

### **2.2.2 Checking Crystal Quality**

Crystals are initially checked under a microscope to determine if they are large enough to allow analysis with X-ray diffraction. Among other qualities, they should have a regular shape and well defined edges. Then the crystals are observed with

cross-polarized light. As the polarizer is turned, the crystal changes from dark to light, depending on the orientation. In this examination the appearance of a rainbow effect indicates that the material under observation may not be a single crystal, as shown in Figure 2.2.

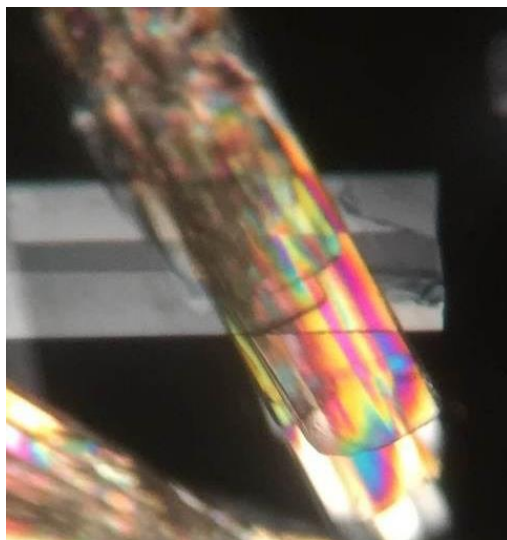


Figure 2.2 Image of lead octanoate crystals under cross-polarized light. The rainbow effect results from several needle-like crystals overlapping.

## **2.3 Solid State Nuclear Magnetic Resonance Spectroscopy**

### **2.3.1 General**

The physical process, paramagnetic relaxation, that makes nuclear magnetic resonance (NMR) spectroscopy possible, was predicted theoretically in 1936 by C. J. Gorter<sup>37</sup>. At the time, he did not connect it to a measurable process. In 1938, NMR was described and measured for the first time by extension of the Stern-Gerlach experiment by Isidor Rabi<sup>38</sup>, who would later receive the 1944 Nobel Prize in Physics

“for his resonance method for recording the magnetic properties of atomic nuclei.<sup>39</sup>” NMR spectra of liquids and solids were first observed in 1946 by two groups, independently: a group at at Harvard University working under E. M. Purcell<sup>40</sup>, and a group at Stanford University working under Felix Bloch<sup>41</sup>. The two men shared the 1952 Nobel Prize “for their development of new methods for nuclear magnetic precision measurements and discoveries in connection therewith.<sup>42</sup>”

Since its discovery, NMR spectroscopy has become one of the most useful tools for solving chemical and physical problems. This technique has proved to be one of the easiest and quickest methods for identifying molecules in the liquid state, through the simple, direct dependence of the chemical shift and coupling on chemical structure. Many samples of interest are solids, the spectra of which contain more information than spectra of the corresponding liquid or solution. However, the presence of many interactions gives complex spectra, often resulting in extremely broad, featureless resonance lines that cannot be easily interpreted in terms of separate interactions, as is done in the spectroscopy of liquids and solutions. The broadening can be attributed to three main interactions: direct dipolar coupling among spins, quadrupolar coupling to electric field gradients at the site of the nucleus, and magnetic-shielding anisotropy arising from distribution of orientations of molecular geometry to the magnetic field. This extra information on molecular structure and motion contained in solid-state NMR spectra must be extracted through advanced instrumentation and experimental techniques.

NMR spectroscopy is applied in a wide variety of fields, most frequently in the identification of organic materials, to determine chemical content, purity of products, and molecular structure of unknown materials. Once the connection between

chemical structure and spectra is determined, NMR can be used to determine phase changes, solubility, conformational exchange, and diffusion.

### 2.3.1.1 Energy Levels in a Magnetic Field

The basic principle behind NMR spectroscopy uses the fact that nuclei are electronically charged particles with spin. When placed in an external magnetic field, the coupling to the magnetic field causes the spin sublevels to have different energies (Figure 2.3). When the sample is in an external field, the nucleus can transfer between those energy states by absorbing or emitting energy. For typical magnetic field intensities, the energy of transition falls in the radio-frequency region of the electromagnetic spectrum. These radio-frequency energy transitions can be measured to give an NMR spectrum of the material under study.

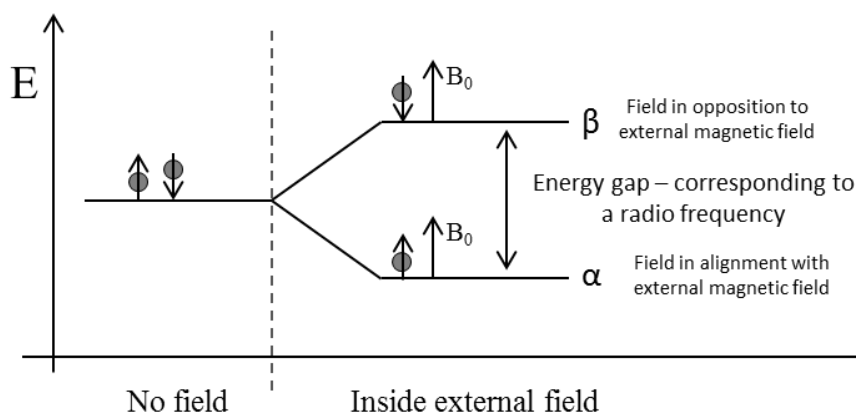


Figure 2.3 Energy diagram for a spin- $1/2$  nucleus, the most commonly studied with NMR ( $^1\text{H}$ ,  $^{13}\text{C}$ ,  $^{15}\text{N}$ ,  $^{31}\text{P}$ ). The energy gap depends on the particular nucleus. Some nuclei, such as  $^1\text{H}$ , have a higher spin which corresponds to a higher energy splitting in a given magnetic field. Because of this fact, one can generally examine only a particular nuclear species in a single experiment, which makes the experiment more specific than other kinds of spectroscopy.

The exact energy where this transition occurs is also dependent on the effective magnetic field at the nucleus. This magnetic field can be affected by many factors, primarily the field produced by electrons in the local chemical environment. This effect is called magnetic shielding. The electronic structure around the nucleus, primarily impacted by what elements are bound to it and how tightly they are bound, has the strongest impact on the resonant frequency. That is what allows this technique to be used in determining chemical structure.

Because the energy exchange is very small and is dependent on the external magnetic field strength, it is reported as the chemical shift relative to some standard material. Chemical shift is defined by:

$$\delta = \frac{\nu - \nu_0}{\nu_0} \quad (1)$$

where  $\nu$  is the frequency measured and  $\nu_0$  is the frequency of some reference material (such as TMS for proton or carbon-13 spectra). The chemical shift defined in this manner gives a specification of the resonance position independent of the magnetic field intensity.

### 2.3.1.2 Magnetic Shielding

Magnetic shielding is a local property of the position of a nucleus. The actual local field created by the development of currents in the electrons surrounding the nucleus by interaction with the externally applied magnetic field does depend on the magnitude of the external magnetic field. More importantly, these induced currents vary from point to point in the molecule, because it involves the interaction of the external field with electrons in different chemical environments. As a result, the total field sensed by the nucleus depends on the nature of the electronic state, particularly in

the near vicinity of the nucleus. This is what gives NMR sensitivity of electronic structure. In the solid state, molecular structure is typically confined over time; as a result, molecules aligned differently relative to the magnetic field have different resonance frequencies. This dependence means the chemical shift describes not only the local density, but also its dependence on geometric parameters such as bond angles.

### **2.3.1.3 Dipolar Coupling**

The local field at the site of a nucleus depends on the presence of other nuclei. In particular, the effective magnetic field due to other nearby nuclei depends on orientation of the spins of neighboring nuclei. This direct coupling is the result of the fact that the magnetic moment of one nucleus may be considered the source of a dipolar field, an effect known as or dipolar coupling. This coupling creates a splitting of the resonance line due to different orientations of spins. As there are usually many nuclear spins in the vicinity, the line is repeatedly split, resulting ultimately in broadening that dominates the spectrum of nuclei in the solid state. For example, the line shape of a  $^{13}\text{C}$  site in a molecule is usually dominated by the many carbon-proton dipolar couplings. For molecules in solution the rapid isotropic tumbling averages the dipolar coupling between spins to zero, which means that, in first order, the dipolar coupling may be neglected in explaining the character of an NMR spectrum. In the solid state, on the other hand, the suppression of the molecular tumbling results in the spectrum's dependence on the dipolar coupling. Fortunately, the effect of dipolar coupling in solids can be suppressed by using specific techniques during measurement, allowing one to detect the effects of interactions such as magnetic shielding. Because dipolar so strongly depends on the distance between nuclear

centers, if one can measure the dipolar coupling between two nuclei, one has a measure of the internuclear distance, which gives information on the structure of a molecule. NMR spectroscopists have developed techniques that allow this measurement under some conditions.

### 2.3.1.4 Vector Model of Excitation and Relaxation Process

Since a nucleus has a magnetic moment because of spin, the Zeeman interaction makes the energy depend on the orientation of the spin relative to the magnetic field. Thus, states in which the spin aligns parallel to the field and antiparallel to the field have different energies. At equilibrium in such a field, the lower-energy state should have excess population over the higher-energy; outside of a magnetic field at equilibrium these two states, being of equal energy, have equal populations. Thus, in a field, a sample has a net bulk magnetization, which is represented by the arrow in Figure 2.4.

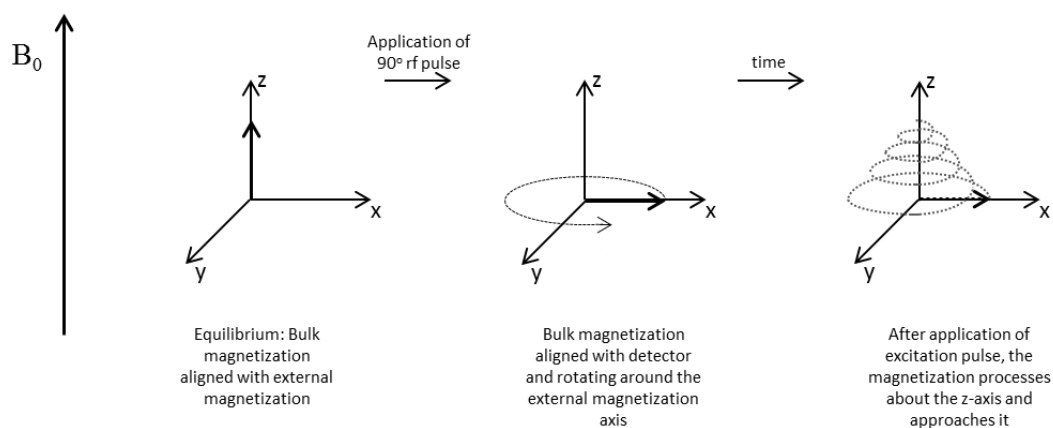


Figure 2.4 Vector diagram for the alignment of the bulk magnetization with the external magnetic field.

On sufficiently short times, one can create nonequilibrium states in which the bulk magnetization is not aligned parallel to the field. If one creates a magnetization that has a projection in the plane perpendicular to the magnetic field, that magnet moment, by the laws of physics, precesses about the direction of the magnetic field. This vectors motion has a specific frequency associated with it, the Larmor frequency. In an external magnetic field,  $B_0$ , the Larmor frequency can be described by:

$$\nu_0 = \frac{\gamma B_0}{2\pi} \quad (2)$$

where  $\nu_0$  is the frequency of absorption observed with NMR spectroscopy. (Of course, one must also remember that the field may also include the effects of the magnetic shielding, as well.) The oscillation of the magnetic moment can be detected by a coil in an electronic circuit sensitive to the appropriate frequencies if the oscillation results in an induced voltage in the coil. For this to work, the coil axis must be maximally perpendicular to the direction of the field about which precession is occurring.

The creation of the so-called transverse magnetization is produced by application of a short oscillating radio-frequency (rf) magnetic field perpendicular to the main field... The magnetization vector moves away from the external field by an angle proportional to the length (time) and intensity of the applied rf pulse. Many different situations can be created by stopping the excitation at various times. The most common ending situation is created by the  $90^\circ$  pulse, where after the application of the radio-frequency excitation the magnetization lies in the x, y plane (Figure 2.4, center), perpendicular to the external field.

Most NMR measurements intend to excite many signals, each at a unique frequency. A strong rf pulse (hard pulse) can move all nuclei away from equilibrium. Some measurements excite only a single signal in a spectrum, done with a weaker rf

pulse (soft pulse). For this effect, the excitation frequency is tailored to the specific signal desired, and a low intensity is used to avoid exciting nearby signals.

Once the magnetization is no longer at equilibrium, it slowly returns to equilibrium, i.e. being aligned along the z-axis (the axis along the field direction) and with zero component perpendicular to the external field. These two processes are independent, and may occur on different time scales. The result of the second process occurs on the shorter time scale, and is detected to separate the frequencies of the various precessing magnetizations, but the magnetic ultimately disappears, usually on the order of seconds or less. While this is happening, one detects this transverse magnetization as described above. The time-dependent transverse magnetization is displays in what is called the “free induction decay” (FID).

It is usually more convenient to spread out the spectrum in frequency space, rather than attempt to determine the frequencies in the time domain. The FID is treated mathematically with Fourier transformation, which results in a display of the same information in the more-convenient form of intensity versus frequency of oscillation, the NMR spectrum.

### **2.3.1.5 Basic Pulse Sequences**

Figure 2.5, below, shows the simplest pulse sequence used for acquisition of 1D NMR spectra. There is a relaxation time that allows the bulk magnetization to align with the external magnetic field. How much time is necessary for the nuclei to relax varies among materials and can range from milliseconds to days. There is a hard, square,  $90^\circ$  pulse of rf radiation to excite the nuclei, moving the bulk magnetization from the z-axis into the x,y-plane. When the pulse ends, the nuclei relax towards equilibrium, giving an rf signal which is recorded as the FID.

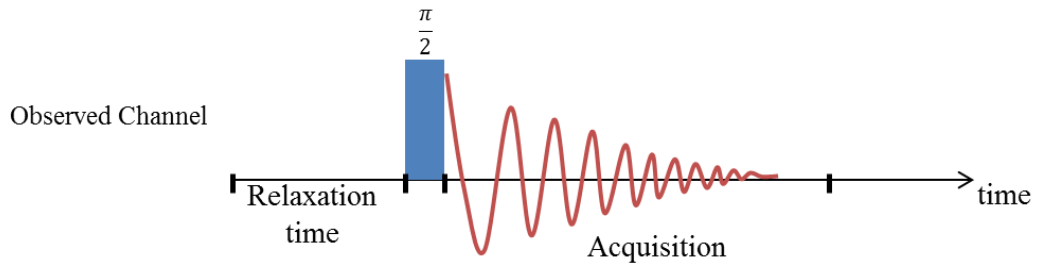


Figure 2.5 1D NMR spectroscopy pulse sequence.

For many experiments, more than one nucleus is involved. This requires the use of more than one rf channel, each tuned to different nuclei. This experiment is common for  $^{13}\text{C}$  NMR experiments, in which application of rf excitation to decouple the  $^1\text{H}$  nuclei simplifies the resulting spectrum by suppressing the effect of coupling between protons and carbons. The decoupled experiment is run using the same experiment on the observed channel as above, but while using rf excitation on the coupled nuclei to effect decoupling.

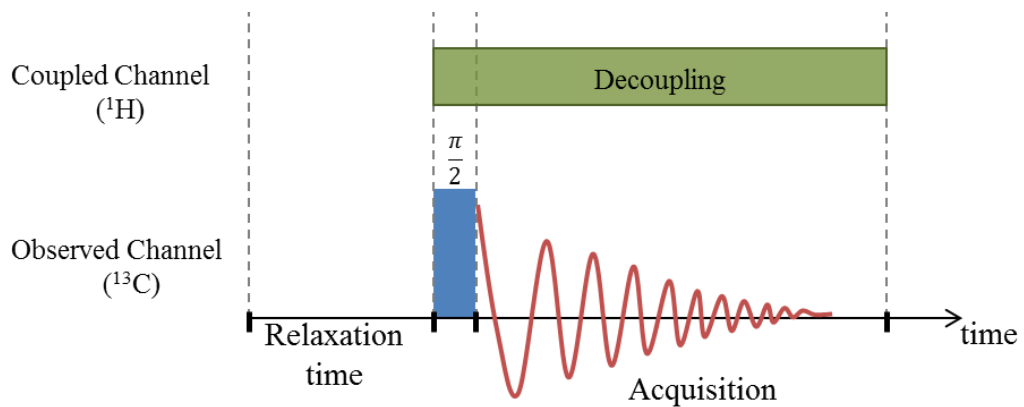


Figure 2.6 1D experiment for detecting  $^{13}\text{C}$  nuclei while decoupling  $^1\text{H}$ .

Some nuclei, such as  $^{13}\text{C}$  or  $^{15}\text{N}$ , suffer from low signal due to low gyromagnetic ratio. This problem can be addressed by the use of cross polarization<sup>43</sup> (CP), which transfers magnetization from a high-gyromagnetic-ratio nucleus, usually  $^1\text{H}$ , to a low-gyromagnetic ratio nucleus. Magnetization transfer occurs by applying rf pulses at the frequency for both nuclei, fulfilling the Hartmann-Hahn condition<sup>44</sup>. The simplest cross-polarization experiment is shown in Figure 2.7.

There are many variation on the cross-polarization step, but all techniques designed to enhance the magnetization in this manner involve the step of creating the transverse magnetization of the first spin, transferring information to the second spin, and then detecting the signal (usually with decoupling to avoid the effects of dipolar coupling).

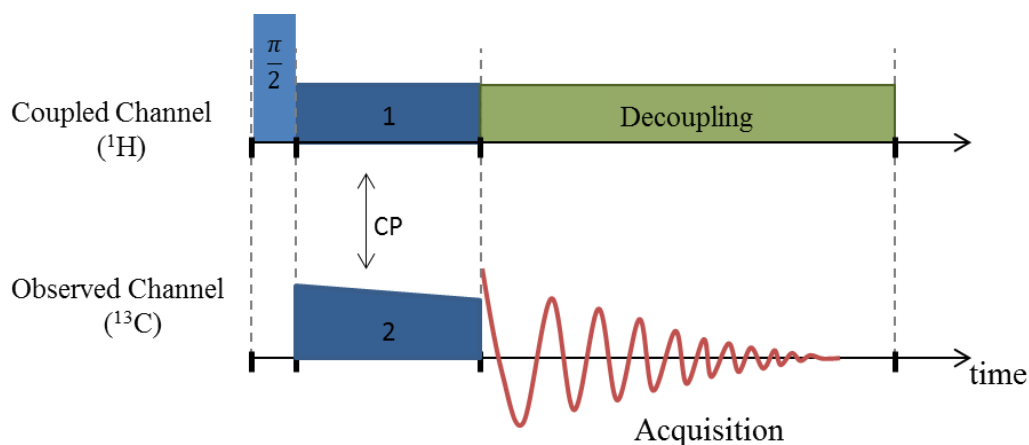


Figure 2.7 Simplest cross-polarization pulse sequence.

### 2.3.1.6 Spectrum of a Solid: Observing Chemical Shift Anisotropy

Solid-state NMR gives insight into the structure of materials that can be obtained by other means only with difficulty. NMR spectra of solids become more

complex than the spectra of the same material in solution, but have the benefit of producing additional structural information. Very often, one has the spectrum of a random orientational distribution of crystallites, rather than the spectrum of a single crystal. Thus, one is faced with interpreting the spectroscopy of a more complex system based on the spread of the resonance due to differences in the magnetic shielding for different orientations of the molecular structure in the magnetic field.

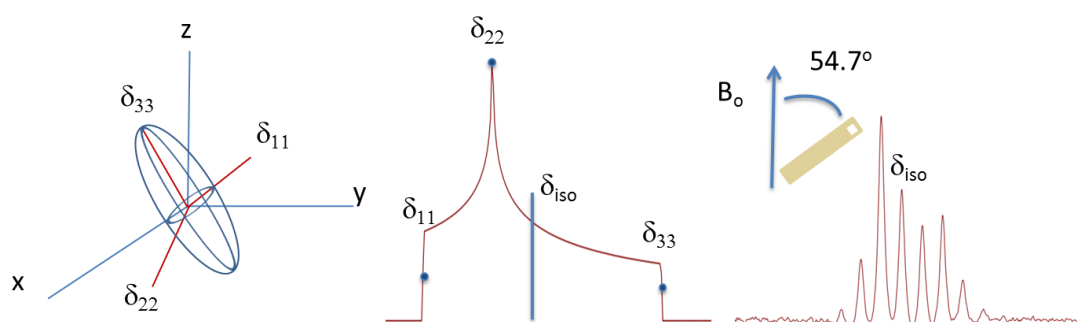


Figure 2.8 The electronic distribution around a nucleus is described by three distinct axes [left]. Each corresponds to a distinct chemical shift [center]. When spinning at the magic angle, the spectrum collapses into multiple peaks [right]

The signal from a polycrystalline sample takes on a distinct shape based on the three dimensional electronic distribution. Because the magnetic shielding is different when each unique axis of the nuclear magnetic shielding tensor is aligned along the field direction, the resonance is usually not a single sharp line, but a band characterized by the range of magnetic shieldings possible for a particular site, as shown in Figure 2.8. The band depends on what chemical shift is observed for a particular nuclear site. There are three unique chemical shifts, identifiable in the band

shape. These occur for alignment of three specific axes, known as the chemical-shift tensor's principal axes, along the magnetic field direction. In a powder, the molecules are aligned randomly in the magnetic field, giving a distribution of chemical shifts. The average of these three principal components of the chemical tensor is the isotropic shift, which is the same as the isotropic average chemical shift observed in a liquid-state NMR experiment, where molecular tumbling averages the magnetic moment around a nucleus. The span, defined by the difference between the two extreme chemical-shift principal components:

$$\Omega = \delta_{33} - \delta_{11} \quad (3)$$

describes the largest distortion of the electronic density around the nucleus. The skew, defined by:

$$\kappa = \frac{3(\delta_{22} - \delta_{iso})}{\Omega} \quad (4)$$

describes the asymmetry of the electronic density.

If the sample is spinning at the magic angle during so-called MAS experiments, one sees a signal that is an array of separate peaks. The distance between peaks is the spinning rate. No matter the spinning rate, the isotropic shift is at the same position, making it easy to distinguish from the other peaks by carrying out experiments at several different spinning speeds. This property gives an advantage to MAS experiments during data collection, as the signal builds up more quickly since it is collected in the narrower peaks.

### 2.3.2 Carbon-13 NMR Spectroscopy

All  $^{13}\text{C}$  spectra presented here were recorded at 11.75 tesla (500.13 MHz proton frequency; 125.76 MHz carbon-13 frequency) with a standard Bruker 4 mm

probe. Carbon-13 chemical shifts were referenced to tetramethylsilane through an external reference of glycine at 176 ppm.  $^{13}\text{C}$  spectra were acquired using cross-polarization and with magic angle spinning at 12 kHz. During acquisition, proton decoupling with a rf field having a strength of 62.5 kHz was used to suppress dipolar couplings. The 90-pulse width was 4  $\mu\text{s}$ , with a recycle delay of 5s.

Table 2.2 Carbon-13 NMR properties<sup>45</sup>

Property	Value
Spin	$\frac{1}{2}$
Natural abundance	1.1%
Gyromagnetic ratio	$6.7283 \cdot 10^7 \text{ rad T}^{-1} \text{ s}^{-1}$
Standard reference material	tetramethylsilane (TMS) at 0 ppm
Typical chemical shift range	0 to 200 ppm

### 2.3.3 Lead-207 NMR Spectroscopy

#### 2.3.3.1 General

All  $^{207}\text{Pb}$  spectra were recorded at 11.75 tesla (104.63 MHz lead-207 frequency) with a standard Bruker 4 mm probe. Lead-207 chemical shifts were referenced to tetramethyllead through an external reference of lead nitrate at -3491 ppm at 298 K<sup>46</sup>. A plot of spinning speed versus the isotropic chemical shift of lead nitrate was obtained to compensate for the temperature increase due to spinning.  $^{207}\text{Pb}$  spectra were acquired using direct excitation and high-power decoupling, with spin-temperature alternation and magic-angle spinning (STA/MAS) at 11 and 12 kHz to obtain isotropic chemical shifts. Acquisition parameters for these experiments included a  $\pi$  pulse width of 8.5  $\mu\text{s}$  and a delay of 1 ms. High-power proton decoupling

(SPINAL-64 at 100 kHz) was used to suppress dipolar couplings. The recycle delay was 5 s and 40,000 scans were acquired.

$^{207}\text{Pb}$  WURST-CPMG spectra of samples were recorded using the parameters of MacGregor et al.<sup>47</sup> WURST pulse widths were 50  $\mu\text{s}$ , with pulse shapes created via the shape tool in Topspin 3.1. Seventy-five Meiboom–Gill loops were acquired for the WURST-CPMG experiments, with a 200  $\mu\text{s}$  echo, and a sweep range of 0.5 MHz in all cases. The recycle delay was 7 s. High-power proton decoupling (CW at 100 kHz) was used to suppress dipolar couplings. Multiple WURST-CPMG spectra were collected at different carrier frequencies by shifting the carrier frequency a multiple of the spikelet separation (981.934 ppm) from spectrum to spectrum. Each spectrum was the result of coadding 10 240 scans. The collected spectra were superimposed to form the final spectrum.

Table 2.3 Lead-207 NMR properties<sup>45</sup>

Property	Value
Spin	1/2
Natural abundance	22.6%
Gyromagnetic ratio	$5.54 \cdot 10^7 \text{ rad T}^{-1} \text{ s}^{-1}$
Standard reference material	tetramethyl lead
Typical chemical shift range	-6200 to 10000 ppm

The analysis of the  $^{207}\text{Pb}$  chemical-shift tensors was performed by fitting the WURST-CPMG envelope. The values of the isotropic chemical shifts were determined from STA/MAS spectra, in some cases with the help of DFT calculations. Fits to the WURST-CPMG envelopes were aided by simulation of the powder pattern with the program WSOLIDS.<sup>48</sup>

### 2.3.3.2 Spin Temperature Alternation

Heavy metal NMR experiments, for nuclei such as lead or tin, can suffer from acoustic ringing, which distorts the line shape of the material of interest at times. The addition of spin-temperature alternation (STA) minimizes the effects of this acoustic ringing of the probe circuits<sup>46</sup>. This pulse sequence takes advantage of the fact that the probe ringing will be consistent regardless of the excitation pulse. The sequence, shown in Figure 2.9, uses a  $180^\circ$  pulse in every other pulse to flip the sign of the sample signal, leaving the ringing signal the same. When this second spectrum is subtracted from the first, the sample signal adds and the probe ringing gradually adds out.

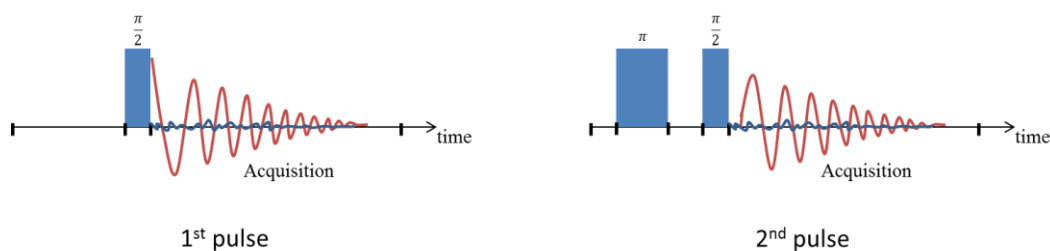


Figure 2.9 Spin-temperature alternation (STA) NMR pulse sequence.

### 2.3.3.3 WURST-CPMG Detection

<sup>207</sup>Pb NMR spectroscopy presents special challenges because of the number of materials with very broad signals. The square excitation pulse used for experiments with most materials (for example, those experiments where one primarily detects <sup>13</sup>C and <sup>1</sup>H) does not create even excitation over a broad enough range for many lead-containing materials. See Figure 2.10. Due to instrument power limitations, the broadest excitation range created on modern instruments stops at approximately 1000 ppm around the carrier frequency. This range is usually sufficient to excite the entire

range of a carbon spectrum with minimal error in intensity at the edges of the spectrum. For many lead materials, where a single signal can cover several thousand ppm, this excitation range can cause a large distortion in the spectrum.

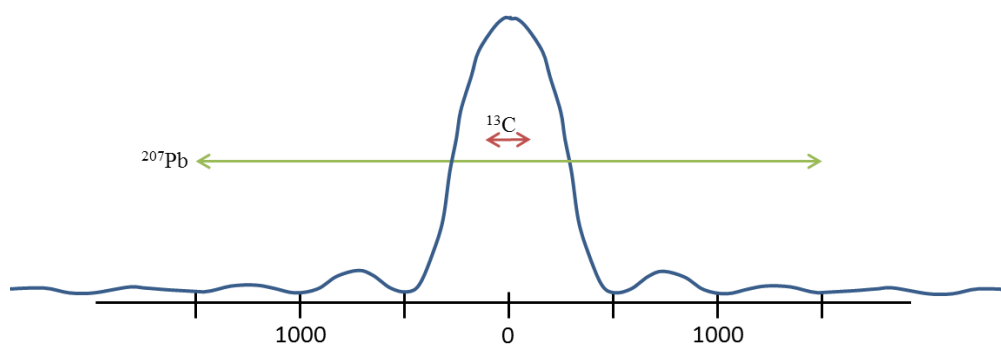


Figure 2.10 Excitation profile for a square  $90^\circ$  pulse (blue), overlain with the typical spectral range for  $^{13}\text{C}$  (red) and a possible range for a single  $^{207}\text{Pb}$  signal (green)

As an example of the problem of nonuniform excitation, Figure 2.11 shows spectra obtained when a powder sample of lead azelate is excited using rf excitation centered at two different frequencies. Since uniform excitation of the powder pattern is not achieved in either spectrum, one cannot fit the MAS sideband pattern to obtain chemical-shift information. Careful study of multiple MAS spectra can be used to determine the isotropic chemical shift, but an alternate method is needed to determine other chemical-shift tensor components.

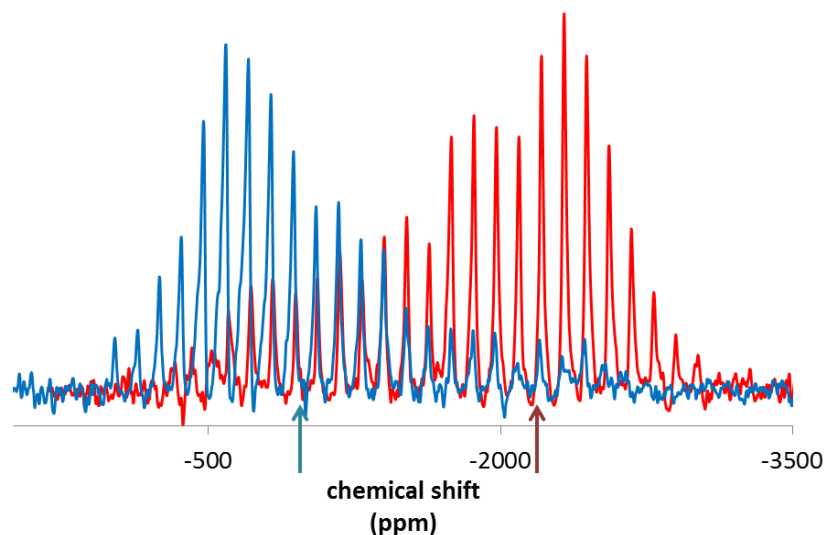


Figure 2.11 Two  $^{207}\text{Pb}$  STA-MAS NMR spectra of lead azelate collected with the center of excitation at -1000 ppm (blue) and -2200 ppm (red).

To combat the challenge of excitation distribution in traditional methods, several approaches have been used. One method uses collection of many spectra to create the equivalent of a wider, even excitation profile as shown in Figure 2.12a. In this method, each subsequent spectrum is collected with a shifted central frequency, spaced so that the sum of excitation gives a flat profile. This can produce a spectrum with a fairly accurate line shape, but there can be distortions that complicate interpretation and require calculations. Another method uses the sum of echo intensities for a series of experiments with varied excitation frequencies to create a profile of the line shape. This experiment results in a spectrum with very low resolution, which is challenging for accurate assignments in samples with multiple signals or for comparing the line shapes of materials with only small differences in their chemical-shift tensors. Both of these methods present the problem of balancing the importance of long acquisition time versus low spectral resolution.

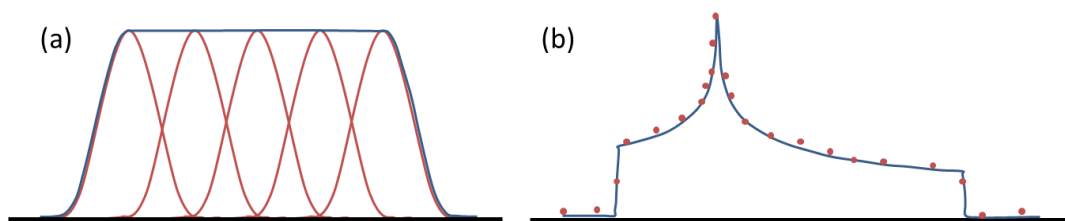


Figure 2.12 Methods of collecting spectra for ultra-widelines include (a) using a sum (blue) of a series of excitation profiles (red) and (b) fitting a theoretical lineshape (blue) to data points of the summation of the echo train from spectra at various excitation frequencies.

More recently, a method for addressing this issue was introduced by Schurko et al<sup>49</sup>, called Wideband Uniform-Rate Smooth-Truncation Carr-Purcell Meiboom-Gill (WURST-CPMG) spectroscopy, which provides relatively short acquisition times with good spectral resolution.

### 2.3.3.3.1 Pulse Sequence

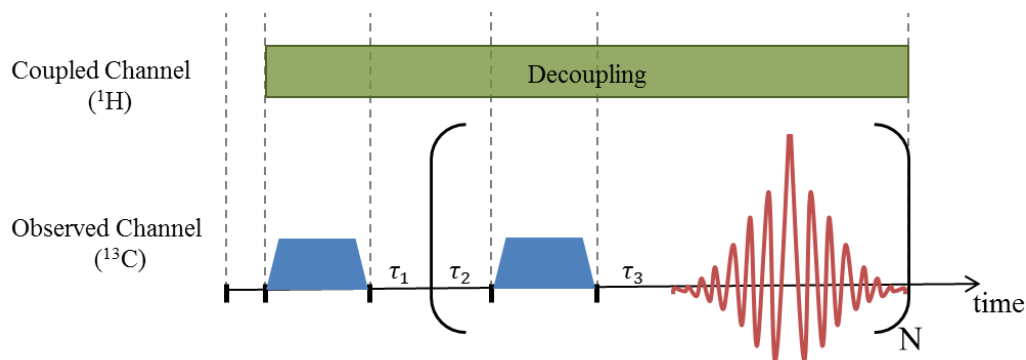


Figure 2.13 WURST-CPMG NMR pulse sequence for broadband excitation.

The WURST-CPMG pulse sequence<sup>49</sup>, shown in Figure 2.13, uses a 90° excitation pulse followed by a series of 180° refocusing pulses to broaden the uniform excitation range of an NMR experiment. A schematic depiction of the resulting excitation shape is shown in Figure 2.14.

The CPMG component of the sequence serves to increase the intensity of the resulting signals after the initial excitation. There is a repeated application of a 180° rf pulse followed by additional acquisition of signal. Because the signal is collected so many times while the noise on each scan remains constant, the signal-to-noise ratio increases, in some cases the enhancement is up to 30 times that of conventional spin-echo experiments<sup>50</sup>.

The WURST component is a type of chirp pulse. The chirp pulse replaces a traditional hard, square pulse with a pulse having controlled phase and amplitude. The WURST class<sup>51</sup> of chirp pulses uses a complex phase modulation to sweep a range of frequencies with a constant transmitter frequency.

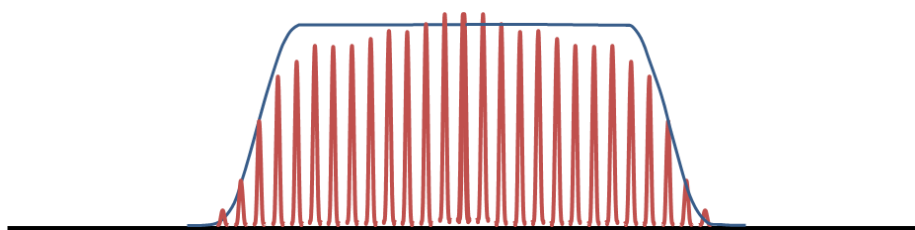


Figure 2.14. Excitation shape (red) for WURST-CPMG NMR pulse sequence.

#### 2.3.3.3.2 Analyzing Spectra

The WURST-CPMG NMR experiment produces a spikelet spectrum which can be used to evaluate the chemical-shift parameters. For very broad materials, the

accumulated spectrum is composed of a superposition of a series of spectra with different offsets for excitation. For the most accurate fit, the isotropic chemical shift is determined from multiple MAS spectra; the  $\delta_{11}$  and  $\delta_{33}$  are determined from the final WURST-CPMG spectrum. The three values are used to calculate the  $\delta_{22}$ , span, and skew. The WURST-CPMG spectrum is used to evaluate the accuracy of the calculated spectrum (from WSolids<sup>48</sup>).

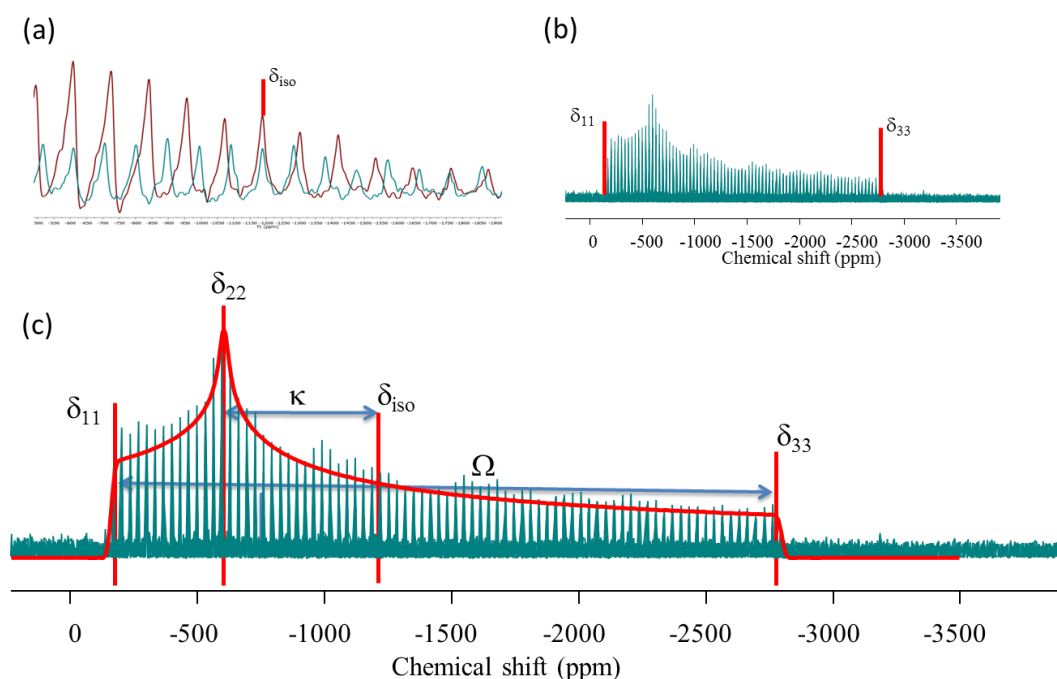


Figure 2.15 Example of fitting of lead azelate with (a) STA-MAS at 10 and 12 kHz spinning and (b) WURST-CPMG spectra. The final fit shown in (c).

#### 2.3.3.4 Broadband Adiabatic Inversion Cross-Polarization

Cross-polarization is effective at creating a large increase in signal-to-noise ratio for NMR spectroscopy of low gyromagnetic ratio nuclei, but the excitation is not

able to excite across very wide powder patterns, such as those seen for many  $^{207}\text{Pb}$  NMR resonances. Broadband adiabatic inversion cross-polarization (BCP) was developed by Harris et al.<sup>52</sup> as a method of applying cross-polarization to nuclei with large chemical-shift anisotropies. This sequence uses an adiabatic chirped rf sweep instead of a square pulse for the contact pulse, allowing broadband conversion for nuclei with large chemical-shift anisotropy.

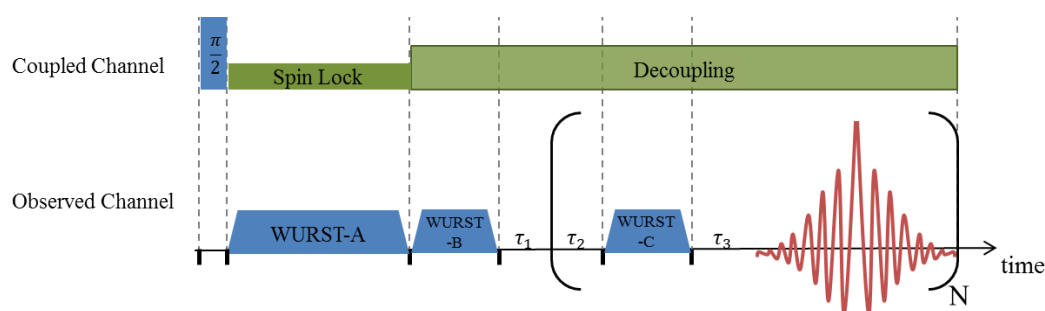


Figure 2.16 BCP pulse sequence

### 2.3.3.5 DNP Enhancement

Dynamic nuclear polarization (DNP) uses microwave radiation of a sample during the NMR measurement to transfer the high polarization of electrons to coupled NMR-active nuclei. There are several mechanisms by which this polarization transfer occurs, but for solids, this mostly comes from the solid effect and the thermal mixing effect.

#### 2.3.3.5.1 The Solid Effect

The solid state effect occurs when a molecule is irradiated with a frequency:

$$\omega = (\omega_e \pm \omega_n) \quad (5)$$

where  $w_e$  and  $w_n$  are the electron and nuclear Larmor frequencies, respectively. This excitation causes the electron and nuclear spins to undergo either flip-flip or flip-flop transitions<sup>53</sup>, illustrated in Figure 2.17. The efficiency of this effect depends on the electron-nuclear dipolar interaction.

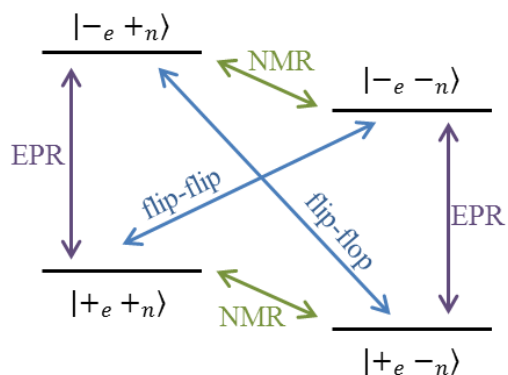


Figure 2.17 Electron-nuclear spin energy levels and transitions.

### 2.3.3.5.2 The Thermal Mixing Effect

The thermal mixing effect occurs when the EPR linewidth is on the order or larger than the proton Larmor frequency<sup>53</sup>. Microwave irradiation at a frequency near the center of the EPR line results in energy being absorbed or emitted by the electron dipolar system (EDS). Then, a thermal contact between the EDS and the nuclear Zeeman system causes nuclear spin flip. The efficiency of this effect depends on the polarization gradient from the microwave irradiation and the degree of thermal contact in the system.

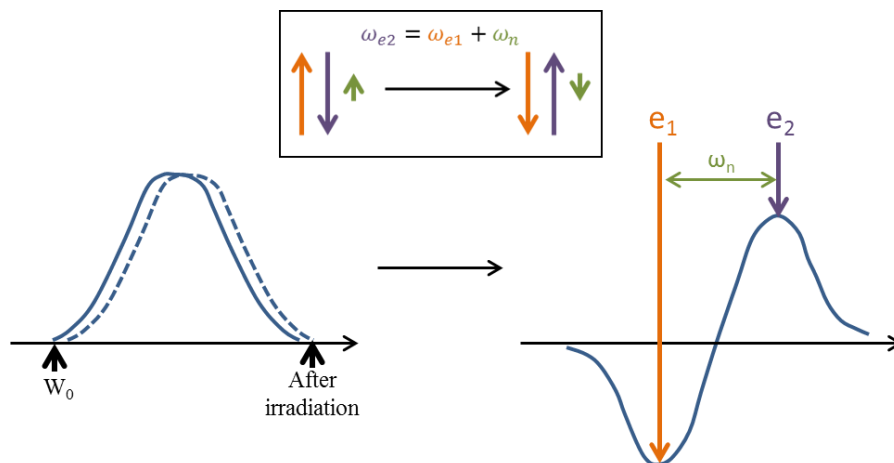


Figure 2.18 Diagram of the thermal mixing mechanism

### 2.3.3.5.3 Application to NMR Pulse Sequences

DNP can be applied to NMR experiments by adding microwave irradiation of the sample before and throughout the normal pulse sequence, as shown in Figure 2.18.

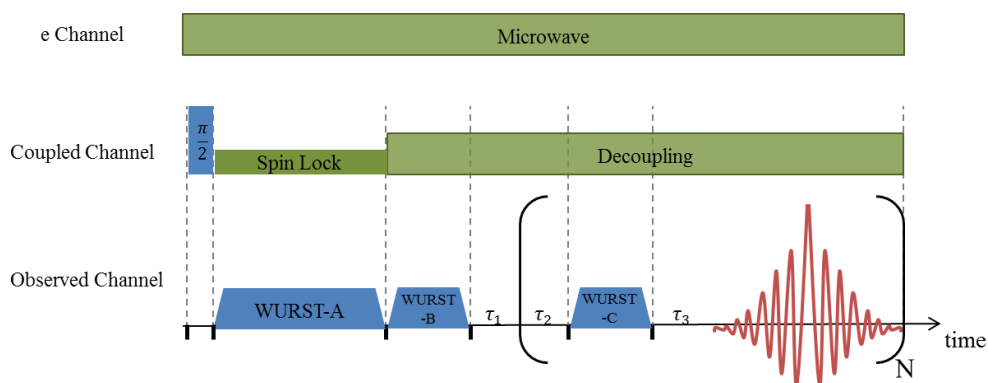


Figure 2.19 Pulse sequence for application of DNP enhancement during the (a) STA/MAS and (b) BCP pulse sequences.

Combining DNP and BCP results in a large enough enhancement of the  $^{207}\text{Pb}$  NMR signal that materials which could not be measured previously, such as basic lead white, can be examined. The feasibility of the DNP-BCP approach has been demonstrated for  $^{195}\text{Pt}[^1\text{H}]$  SSNMR in platinum-containing metal-organic frameworks<sup>54</sup> and for  $^{35}\text{Cl}[^1\text{H}]$  SSNMR in pharmaceuticals<sup>55</sup>.

### 2.3.4 Tin-119 NMR Spectroscopy

$^{119}\text{Sn}$  ssNMR spectra were recorded at 11.75 tesla (186.50 MHz  $^{119}\text{Sn}$  frequency) with a standard Bruker 4 mm probe.  $\text{SnCl}_2$  in HCl was used as a secondary external reference, the isotropic chemical-shift being -388.1 ppm relative to tetramethyltin<sup>56</sup>. Tin-119 spectra were acquired using direct excitation with STA/MAS at 5 and 12 kHz spinning with 1024 and 564 scans, respectively. Acquisition parameters for these experiments included a  $\pi$  pulse width of 5.2  $\mu\text{s}$  and a delay of 1 ms. High-power proton decoupling (SPINAL-64 at 100kHz) was used to suppress dipolar couplings. The recycle delay was 5 s.

Table 2.4 Tin-119 NMR properties<sup>45</sup>

Property	Value
Spin	1/2
Natural abundance	8.58
Gyromagnetic ratio	$-10.0138 \cdot 10^7 \text{ rad T}^{-1} \text{ s}^{-1}$
Standard reference material	tetramethyl tin
Typical chemical shift range	-2500 to 3000 ppm

The  $^{119}\text{Sn}$  chemical-shift tensors were determined using the isotropic chemical shift determined by spinning at 12 kHz and fitting the spinning sideband pattern from a spectrum at 5 kHz using HBA 3.1<sup>48</sup>. From the fits, the relative mole percentage of each species was determined.

## Chapter 3

### ANALYSIS OF LEAD SOAPS

In order to fully understand the process of lead soap formation, it is important to investigate the structural properties of the product. Because it is difficult to grow single crystals of lead carboxylates to obtain a structure directly, structural information must be inferred through a technique sensitive to small changes in structure.  $^{207}\text{Pb}$  ssNMR spectroscopy provides a probe into the local structure around the lead center of lead soaps. Combined with  $^{13}\text{C}$  NMR and FTIR spectroscopies to obtain information about the extended structure, parallels can be drawn between materials. Once there are correlations between certain groups of materials, more easily crystallized materials can be used to infer structure in the rest of the group.

#### 3.1 Preparation of Lead Soaps

Eight lead carboxylates were synthesized: lead palmitate, lead stearate, lead undecanoate, lead decanoate, lead nonanoate, lead octanoate, lead heptanoate, lead hexanoate. The lead octanoate was synthesized by methods adapted from previously published protocols<sup>18, 57</sup>.

The lead carboxylates were synthesized from equimolar amounts of lead nitrate dissolved in 20 mL of water and the corresponding acid dissolved in 50 mL of ethanol. The two solutions were mixed with an equimolar amount of potassium hydroxide and reacted for 20 min at 80°C. The reaction was cooled to room

temperature, filtered, and washed with water, methanol, ethanol, and acetone. The resulting material was dried in an oven at 100°C for 1 hour to remove excess water.

### **3.2 NMR Spectroscopy of Lead Soaps**

Lead NMR spectroscopy's sensitivity to local structure makes it ideal for determining structures of materials that are hard to obtain as single crystals. The chemical shift for lead materials can be sensitive to very small changes in the arrangement of bonding orbitals. These changes can frequently be correlated to changes observed in carbon NMR. Carbon-13 NMR spectra are collected to give details about conformational changes in the extended structure of a material.

### 3.2.1 Carbon -13 NMR Spectroscopy

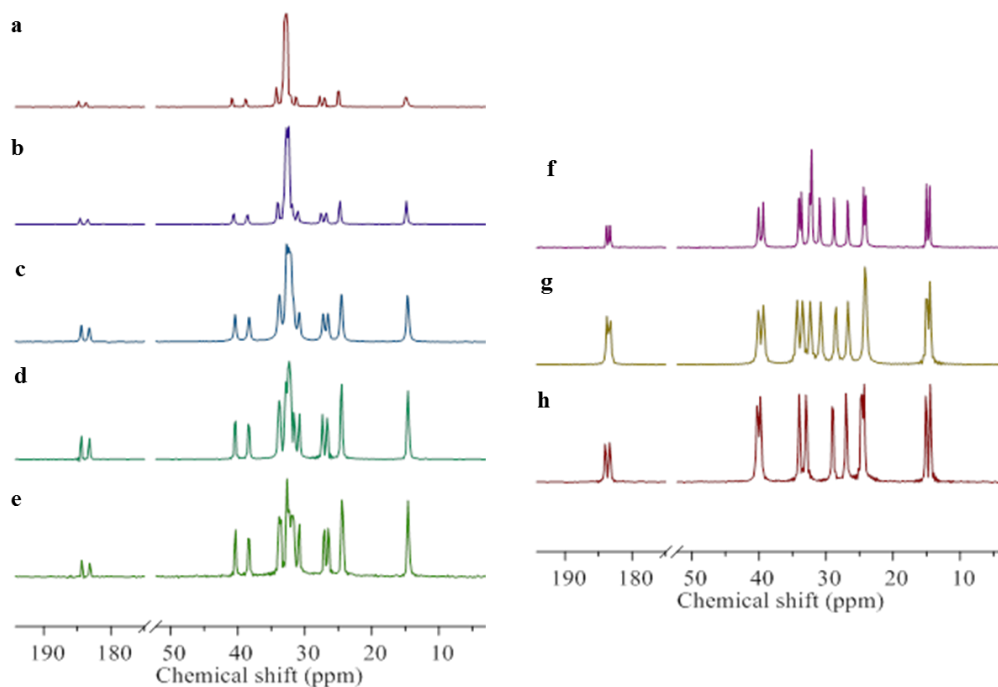


Figure 3.1  $^{13}\text{C}$  NMR spectra of (a) lead octadecanoate, (b) lead hexadecanoate, (c) lead undecanoate, (d) lead decanoate, (e) lead nonanoate, (f) lead octanoate, (g) lead heptanoate, (h) lead hexanoate.

The  $^{13}\text{C}$  NMR spectra of lead soaps, shown in Figure 3.1, indicate two possible geometries for the coordination of the fatty acid chains to the lead ion. These geometries are indicated by the doubling of the carboxyl group resonance and the alpha carbon resonance for all the lead soaps. The presence of two conformers is in agreement with the published crystal structure of lead heptanoate<sup>58</sup> that shows two fatty acid chains in the asymmetric unit, as well as previously published  $^{13}\text{C}$  NMR spectra of lead decanoate and lead stearate<sup>59</sup>. There is a difference in the amplitude of

splitting between the long- and short-chain soaps, summarized in Table 3.1. The long chain soaps have carboxyl group splittings of 1.13 to 1.25 ppm and the short chain soaps have splittings from 0.5 to 0.69 ppm. A similar group difference appears in the splittings of the alpha carbon.

The resonances of carbons further down the chain are split to varying degrees. These splittings of the carbon signals result not from differences in coordination geometry, but from differences in distortion in the chains. For the short-chain soaps, the splitting in the methyl region of the spectrum indicates a difference in the chain-end conformations. There is no apparent splitting of the methyl resonances of the long chain carboxylates.

Table 3.1 Summary of the  $^{13}\text{C}$  NMR chemical shifts of the lead carboxylates

	C1	C2	C3	Next to methyl	Methyl group
Lead hexanoate	183.99, 183.34	40.25, 39.81	29.00, 27.00	24.68, 24.35	15.06, 14.44
Lead heptanoate	184.60, 184.10	40.93, 40.20	29.39, 27.58	25.01	15.85, 15.36
Lead octanoate	183.82, 183.32	40.07, 39.38	28.80, 26.75	24.38, 24.11	15.02, 14.54
Lead nonanoate	183.91, 182.73	39.92, 37.93	26.65, 26.05	24.00	14.17
Lead decanoate	184.41, 183.20	40.39, 38.37	27.36, 26.67	24.53	14.62
Lead undecanoate	184.40, 183.22	40.40, 38.32	27.25, 26.54	24.53	14.67
Lead hexadecanoate	184.57, 183.42	40.58, 38.53	27.51, 26.79	24.73	14.82
Lead octadecanoate	184.80, 183.68	40.85, 38.81	27.79, 27.07	24.98	14.91

### 3.2.2 Lead-207 NMR Spectroscopy

A combination of  $^{207}\text{Pb}$  NMR pulse sequences was necessary to determine the NMR parameters of the lead carboxylates, due to the large chemical-shift span. A comparison of spectra for lead stearate and lead palmitate, obtained with direct excitation, STA/MAS at 12 kHz to those obtained with the WURST-CPMG sequence<sup>60</sup>, is shown in Figure 3.2. Similar line shapes are achieved using both pulse sequences; however, the spectrometer time is greatly reduced from two days for the STA/MAS experiment to 4 hours for the WURST-CPMG experiment. The greater advantage of the WURST-CPMG experiment is for the shorter chain carboxylates, as the wide powder patterns cannot be easily excited with conventional techniques.

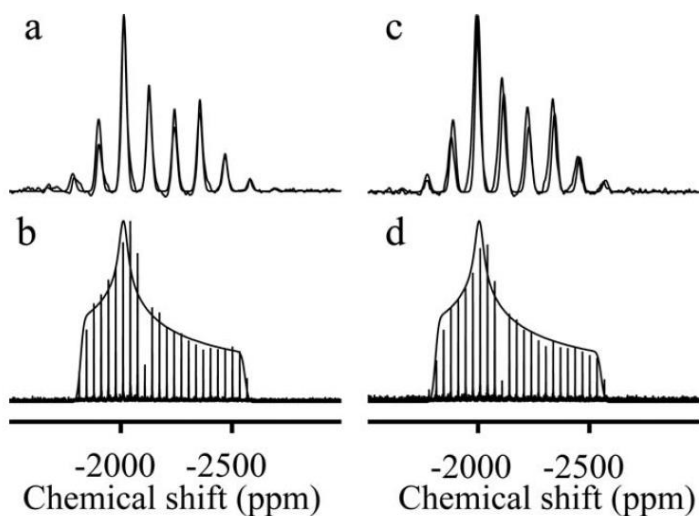


Figure 3.2 Comparison of spectra obtained with direct excitation, STA/MAS at 12 kHz (a and c) with spectra of nonspinning samples obtained with the WURST-CPMG sequence (b and d) for lead palmitate (a and b) and lead stearate (c and d). Each spectrum also shows the simulated fit for the tensor. The decreases in intensity at the centers of (b) and (d) are a result of a spectral artifact due to the placement of the carrier frequency.

In determining the chemical-shift tensors of nuclei in these materials, both STA/MAS experiments and WURST-CPMG experiments are used. The STA/MAS experiment allows the most accurate measurement of the isotropic chemical shift. The STA/MAS experiment was recorded at two different spinning speeds to confirm which central band corresponded to the isotropic shift, and those measured values were averaged. The WURST-CPMG experiments were used to determine the edges of the chemical shift envelope,  $\delta_{11}$  and  $\delta_{33}$ .

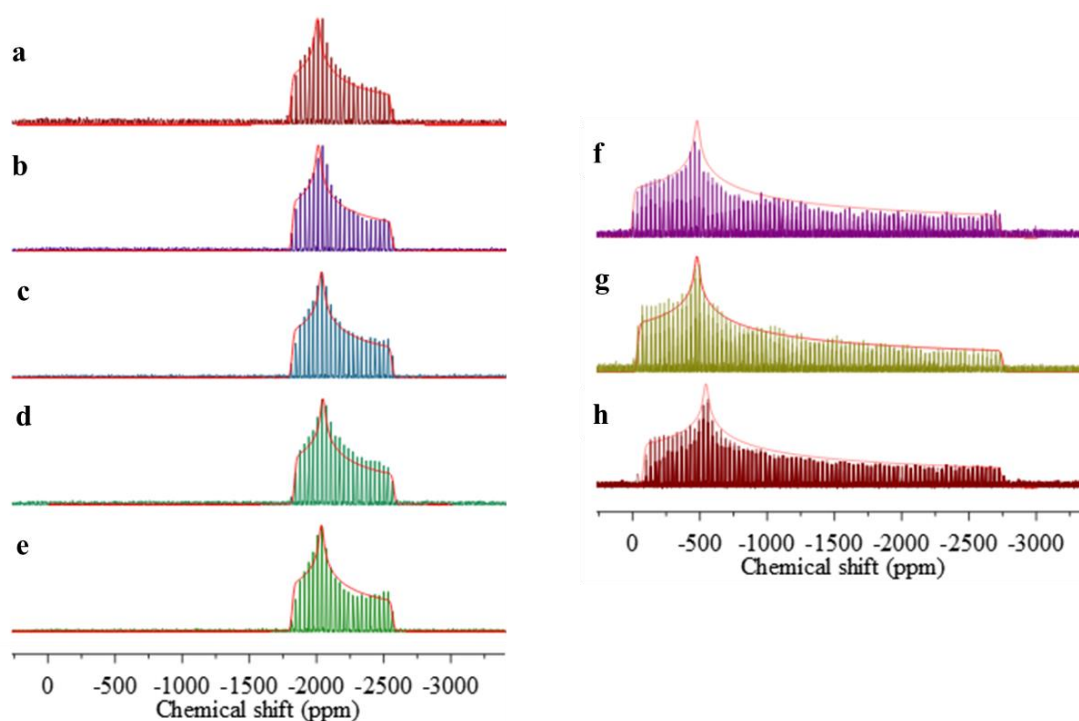


Figure 3.3  $^{207}\text{Pb}$  NMR spectra of (a) lead octadecanoate, (b) lead hexadecanoate, (c) lead undecanoate, (d) lead decanoate, (e) lead nonanoate, (f) lead octanoate, (g) lead heptanoate, (h) lead hexanoate.

The local environment around the lead site in the long-chain carboxylates differs from the environment around the lead site in short-chain carboxylates, as shown by the lead WURST-CPMG spectra in Figure 3.3. The principal components of the chemical-shift tensors are summarized in Table 3.2. The similarity between spectra of C11, C16, and C18 suggest similar spectra for C12 – C15, but we did not examine these materials. Each  $^{207}\text{Pb}$  spectrum is fit with a single chemical-shift tensor, indicating a single lead site in each unit cell.

The parameters for the  $^{207}\text{Pb}$  NMR tensors place lead carboxylates into two subgroups, matching the  $^{13}\text{C}$  NMR and FTIR data. Long-chain carboxylates have relatively narrow spans, around 750 ppm, suggesting a symmetric, evenly distributed arrangement of the ligands. Short-chain carboxylates have large spans, around 2700 ppm, suggesting a strongly asymmetric arrangement of ligands. There is a similar difference between the isotropic chemical shifts: the long-chain group has isotropic shifts around -2125 ppm and the short-chain group has isotropic shifts around -1100 ppm. There is also a correlation of the skews. Short-chain soaps show skews in the range of 0.65-0.70 and long-chain soaps show skews in the range of 0.42-0.48. These values are outlined in Table 3.2.

Table 3.2 Summary of the chemical-shift tensor components of lead carboxylates.

	$\delta_{11}$ (ppm)	$\delta_{22}$ (ppm)	$\delta_{33}$ (ppm)	$\delta_{\text{iso}}$ (ppm)	$\Omega$ (ppm)	$\kappa$
Lead hexanoate	$-100 \pm 3$	$-533 \pm 8$	$-2745 \pm 5$	$-1126 \pm 3$	$2645 \pm 6$	$0.67 \pm 0.01$
Lead heptanoate	$-40 \pm 8$	$-480 \pm 10$	$-2750 \pm 5$	$-1090 \pm 3$	$2710 \pm 9$	$0.68 \pm 0.01$
Lead octanoate	$0 \pm 4$	$-469 \pm 8$	$-2740 \pm 5$	$-1070 \pm 3$	$2740 \pm 6$	$0.66 \pm 0.01$
Lead nonanoate	$-1819 \pm 3$	$-2035 \pm 5$	$-2565 \pm 7$	$-2140 \pm 3$	$746 \pm 8$	$0.42 \pm 0.02$
Lead decanoate	$-1836 \pm 5$	$-2047 \pm 6$	$-2575 \pm 8$	$-2153 \pm 4$	$739 \pm 9$	$0.43 \pm 0.03$
Lead undecanoate	$-1818 \pm 3$	$-2036 \pm 5$	$-2570 \pm 7$	$-2141 \pm 3$	$752 \pm 8$	$0.42 \pm 0.02$
Lead hexadecanoate	$-1820 \pm 3$	$-2013 \pm 5$	$-2560 \pm 3$	$-2131 \pm 3$	$740 \pm 4$	$0.48 \pm 0.02$
Lead octadecanoate	$-1810 \pm 3$	$-2007 \pm 6$	$-2555 \pm 3$	$-2124 \pm 4$	$745 \pm 4$	$0.47 \pm 0.03$

Several studies have shown a similar segregation in assignments in heavy metal NMR correlated with crystal structure. Two birefringent lead-gold cyanide complexes, analyzed by Katz et al.<sup>57b</sup>, showed a dependence on stereochemical activity in the lead spans, skews, and isotropic shifts. Briand et al.<sup>61</sup> found that large spans and skews in lead-207 chemical shift tensors could be attributed to the presence of a stereochemically active lone pair, based on measurements of 4-substituted pyridine adducts of lead thiolates.

The differences in <sup>207</sup>Pb NMR parameters of the lead carboxylates in each group primarily result from differences in  $\delta_{11}$  and  $\delta_{22}$ , the least-shielded components. The value of  $\delta_{33}$  is similar for all of the lead carboxylates. In the longer chain carboxylates, the  $\delta_{11}$  and  $\delta_{22}$  are ~1500 ppm more shielded than in the short-chain. This observation indicates a difference in Pb coordination geometry, which is also reflected in the NMR properties of the carboxyl carbons. The coordination geometries around the metal ions of copper octanoate and copper decanoate change similarly, as implied by comparison of Raman spectra<sup>62</sup> of the materials.

The precise point in the progression of carboxylate structures with chain length where this transition long-chain and short-chain behavior occurs depends on how one chooses to examine the materials. These ssNMR experiments display the change in conformation occurring between C8 and C9. Studies with other techniques display this change at a different point. Ellis et al.<sup>63</sup>, conducted infrared and X-ray studies and concluded that this transition occurs between C12 and C14. Differential thermal analysis (DTA) experiments, conducted by Adeosun and Sime<sup>64</sup>, detect a number of intermediate liquid crystalline phases, with the transition of coordination behavior occurring between C8 and C12 with C10 displaying an intermediate behavior. It

should be noted that those studies only investigated the members of the series with an even number of carbons. This may influence the conclusions if, as suggested by Arenas et al.<sup>65</sup>, the packing of the chains of Pb carboxylates of C9-C12 is effected by the thermal history of the sample. Thermal history showed no effect for Pb carboxylates longer than C13 or less than C8, based on lack of difference in Raman spectra of recrystallized and premelted samples.

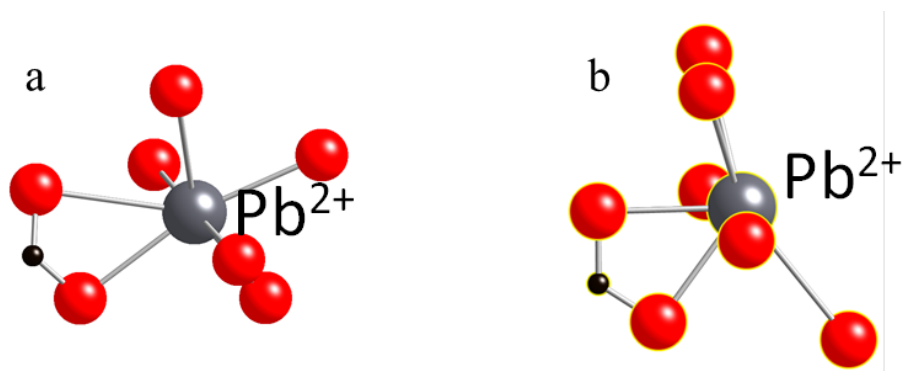


Figure 3.4 Illustration of the (a) hemi directed and (b) holo directed structures predicted by Shimoni-Livney.

### 3.3 FTIR Spectroscopy of Lead Soaps

FTIR spectroscopy was used to analyze the same series of lead carboxylates because it is a more heavily documented technique, with the advantage of requiring much smaller samples, in application to paint degradation studies. The low-frequency bands have been shown to be sensitive to alkyl chain packing<sup>63</sup>. Progression bands associated with the wagging and twisting of the hydrocarbon chain have been used to estimate the ratio of different length carboxylates present in a mixed lead soap sample<sup>66</sup>.

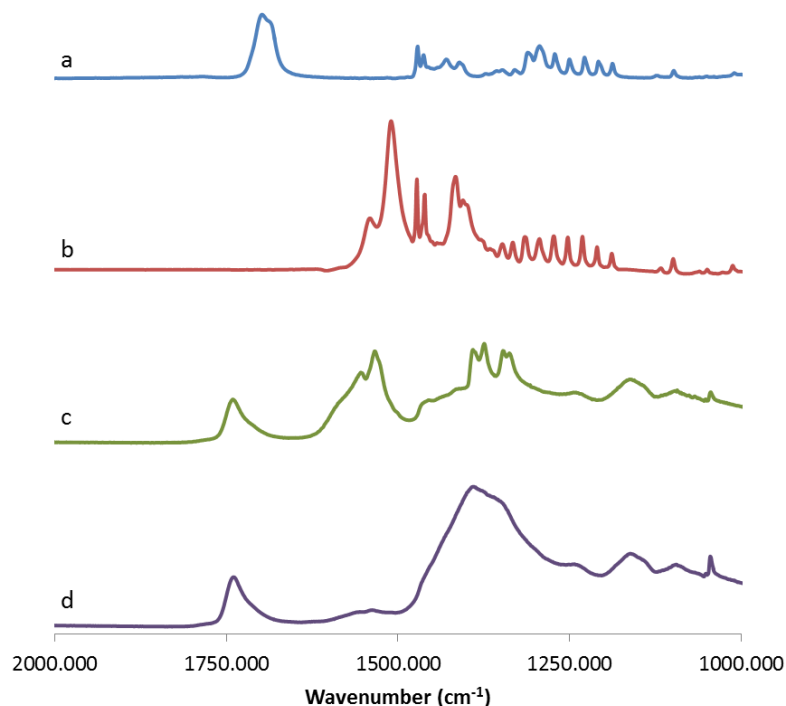


Figure 3.5 FTIR spectra of (a) palmitic acid, (b) lead palmitate, a basic lead white paint film as (c) a protrusion in the film and (d) the sample paint sample crushed under liquid nitrogen.

FTIR provides a minimally invasive technique for observing the presence of lead soaps forming in a painting. The carboxylic acid stretch band is shifted considerably when bound to a lead ion, as shown in Figure 3.5. This same change can be observed in a paint film, with broadening resulting from the presence of several types of carboxylates in the drying oil, or of an amorphous film or ionomer. Figure 3.5, part c and d, show the difference between lead soaps found and measured on a protrusion versus spread through the paint film where the signals broaden even further. The paint in Figure 3.5c was measured directly on a soap aggregate, so the signal at

1530  $\text{cm}^{-1}$  is rather large. The paint in Figure 3.5d was crushed, spreading the small amount of soap through the paint, lowering the signal of the soap to where it is barely detectable.

### 3.3.1 Effects of Chain Length in FTIR of Lead Soaps

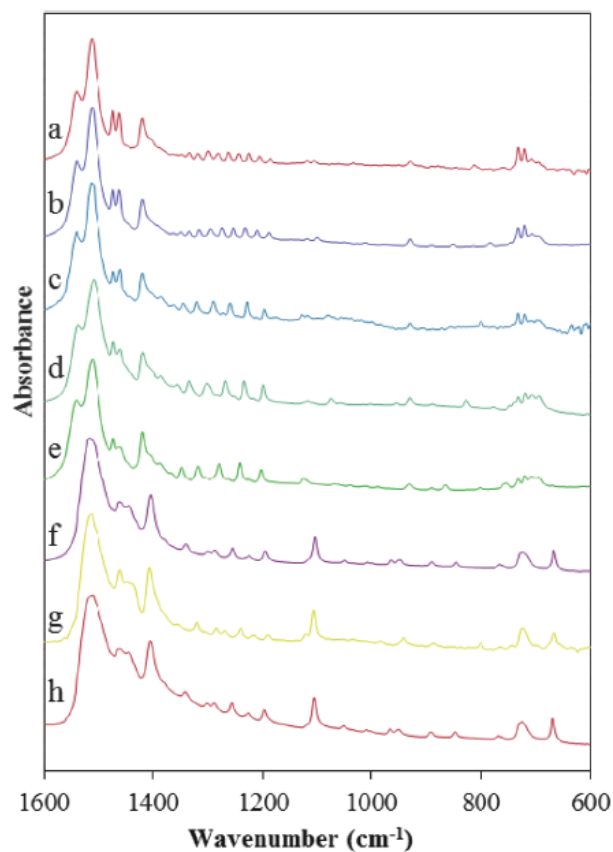


Figure 3.6 Spectra of (a) lead octadecanoate, (b) lead hexadecanoate, (c) lead undecanoate, (d) lead decanoate, (e) lead nonanoate, (f) lead octanoate, (g) lead heptanoate, (h) lead hexanoate.

The FTIR results for the lead carboxylates are consistent with the NMR data. The data can be split into two subgroups, long-chain soaps (C9-C18) and short-chain soaps (C6-C9). In the asymmetric carboxylate stretch, the short-chain lead soaps show a single broad peak centered around  $1525\text{ cm}^{-1}$ , while the long-chain lead soaps show a doublet at  $\sim 1515$  and  $1540\text{ cm}^{-1}$ . The short-chain soaps also show a single feature around  $720\text{ cm}^{-1}$  for the  $\text{CH}_2$  rocking mode, while the long-chain soaps each show multiple features. The long-chain soaps show progression bands in the region from  $1150$  to  $1350\text{ cm}^{-1}$ . These progression bands result from the wagging and twisting of the hydrocarbon chain, so it can be strongly affected by tight packing in a solid material. The shorter carboxylates do not display consistent features in this region, suggesting a difference in chain motions.

### 3.4 X-Ray Diffraction Analysis of Lead Octanoate

The solid-state structures of a number of lead carboxylates have been previously reported: lead formate<sup>67</sup>, lead acetate trihydrate<sup>68</sup>, lead propionate<sup>69</sup>, lead butyrate<sup>70</sup>, lead pentanoate<sup>69</sup>, lead hexanoate<sup>69</sup>, and lead heptaonate<sup>71</sup>, and lead nonanoate<sup>72</sup>. The single-crystal X-ray diffraction structures or neutron diffraction structures of other higher homologues such as lead palmitate and lead stearate have, to our knowledge, not been reported, presumably because of inherent amphipathicity challenging solvent-based crystallization.

The NMR results above have been interpreted in terms of the local environment of the lead ion. In the lower homologues (C8 and shorter), the broad line shapes appearing in the NMR spectra indicate strong anisotropic magnetic-shielding interactions, whereas the NMR spectra of the higher homologues (C9 and longer) suggest a much less anisotropic electronic environment. The difference has been

suggested to be an indicator of structural differences<sup>73</sup>. The NMR spectroscopy of lead octanoate suggests that its structure should be similar to the shorter-chain homologues than to the longer-chain homologues.

### 3.4.1 Synthesis of Lead Octanoate Single Crystals

Lead octanoate was synthesized by methods adapted from previously published protocols<sup>18,57</sup>, discussed in Section 3.1. Single crystals were obtained by slow evaporation of a saturated solution prepared from 10.4 mg of lead octanoate in 20 mL of toluene.

### 3.4.2 Refinement

Crystal data, data collection and structure refinement details are summarized in Table 3.3. Hydrogen atoms were assigned geometrically calculated positions with  $C-H = 0.98 - 1.00$  Å, and  $U_{iso}(H) = 1.2 U_{eq}(C)$  or  $1.5 U_{eq}(C)$  for methyl hydrogen atoms.

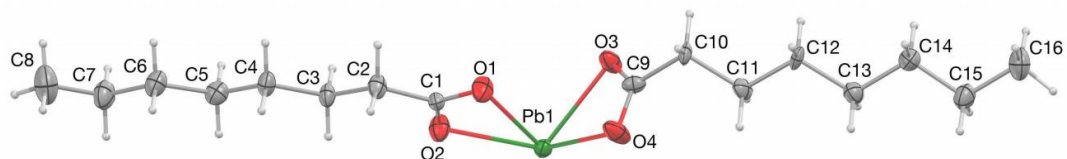


Figure 3.7 Molecular diagram with 30% probability ellipsoids. Hydrogen atoms depicted with arbitrary radius.

Table 3.3 Experimental details<sup>74</sup>

Crystal data	
Chemical Formula	C <sub>16</sub> H <sub>30</sub> O <sub>4</sub> Pb
<i>M</i> <sub>r</sub>	493.59
Crystal system, space group	Triclinic, Pī
Temperature (K)	200
<i>a</i> , <i>b</i> , <i>c</i> (Å)	4.8283 (2), 7.2464 (3), 25.6666 (12)
α, β, γ (°)	87.826 (1), 85.425 (1), 89.334 (1)
<i>V</i> (Å <sup>3</sup> )	894.48 (7)
<i>Z</i>	2
Radiation type	Mo Kα
μ (mm <sup>-1</sup> )	9.44
Crystal size (mm)	0.56 x 0.53 x 0.04
Data collection	
Diffractometer	Bruker AXS APEX
Absorption correction	Multi-scan APEX3 (Bruker, 2015)
<i>T</i> <sub>min</sub> , <i>T</i> <sub>max</sub>	0.327, 0.746
No. of measured, independent and observed [ <i>I</i> > 2σ( <i>I</i> )] reflections	22006, 4188, 3933
<i>R</i> <sub>int</sub>	0.040
(sin θ/λ) <sub>max</sub> (Å <sup>-1</sup> )	0.654
Refinement	
R[F <sup>2</sup> > 2σ(F <sup>2</sup> )], wR(F <sup>2</sup> ), <i>S</i>	0.040, 0.138, 1.05
No. of reflections	4188
No. of parameters	192
H-atom treatment	H-atom parameters constrained
Δρ <sub>max</sub> , Δρ <sub>min</sub> (e Å <sup>-3</sup> )	2.85, -2.62

Although the asymmetric unit shows, as expected, the lead cation and two octanoate carboxylate anions (Figure 3.7), a close inspection of the coordination sphere of the lead ion (Table 3.4 and Figure 3.8) reveals seven Pb—O close atom contacts. Further, the O-atoms are not uniformly distributed but instead show a gap roughly coplanar with O1<sup>i</sup>, O3 and O4<sup>iii</sup>, typical of hemidirected lead coordination

similar to the structure reported for lead heptanoate<sup>58</sup>. This distinction between the structural motifs supports the idea that the difference in the solid-state <sup>207</sup>Pb NMR spectroscopy results from the difference in coordination geometry<sup>73</sup> around the lead site.

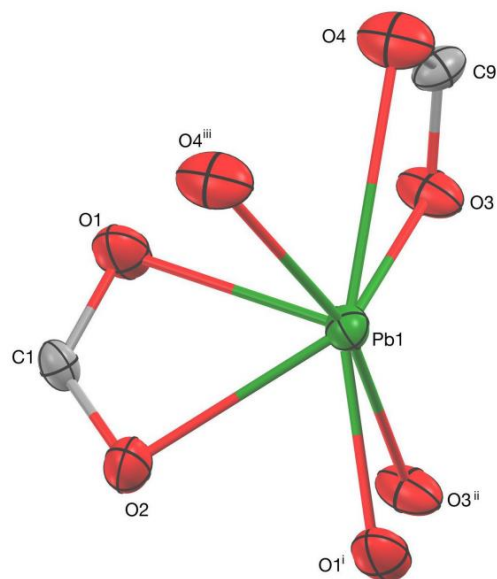


Figure 3.8 Pb coordination environment with 30% probability ellipsoids. Symmetry codes: (i)  $x+1, y, z$ ; (ii)  $-x+1, -y+1, -z+1$ ; (iii)  $-x+1, -y, -z+1$ .

Table 3.4 Selected geometric parameters ( $\text{\AA}$ ,  $^\circ$ ) for lead octanoate

Pb1 – O1	2.454 (5)	Pb1 – O3	2.586 (5)
Pb1 – O1 <sup>i</sup>	2.944 (5)	Pb1 – O4	2.757 (5)
Pb1 – O2	2.412 (5)	Pb1 – O4 <sup>iii</sup>	2.605 (5)
Pb1 – O3 <sup>ii</sup>	2.544 (5)		
O3 <sup>ii</sup> – Pb1 – O4 <sup>iii</sup>	164.7 (2)	O4 – Pb1 – O1 <sup>i</sup>	143.12 (16)
O3 – Pb – O1 <sup>i</sup>	151.96 (17)		

Symmetry codes: (i)  $x+1, y, z$ ; (ii)  $-x+1, -y+1, -z+1$ ; (iii)  $-x+1, -y, -z+1$ .

## Chapter 4

### ANALYSIS OF ZINC SOAPS

#### 4.1 Introduction

In the 19<sup>th</sup> century<sup>75</sup>, zinc oxide (ZnO) became available for commercial use. Its eventual popularity, until it began being replaced by titanium white in the early 20<sup>th</sup> century<sup>75</sup>, stemmed from growing concern about the toxicity of lead materials. Zinc oxide was a safe alternative that met artist's primary needs. There was a period of overlap of use due to the traditional use of basic lead white.

Although there are benefits to the use of zinc oxide over basic lead white, there are drawbacks involving the structural integrity of the paint. Zinc oxide paints can be quite brittle<sup>76</sup>, leading to some artwork containing a zinc oxide base layer chipping as the paint ages. Zinc oxide has also been linked to soap formation<sup>77</sup>, similar to lead soaps, disrupting the surface and changing the color of artwork. Because of the issue of paint chipping in zinc based paints, there is a growing interest in the mechanisms of aging in zinc oxide paints.

#### 4.2 Synthesis and Experiment

Zinc soaps were prepared by mixing zinc nitrate ( $\text{Zn}(\text{NO}_3)_2$ ) in aqueous solution with the desired fatty acid in ethanol solution. The two solutions were heated to 80°C, with stirring to dissolve the solids, then mixed. The mixture was allowed to

react for one hour. The resulting solids were filtered and washed with water, ethanol, methanol, and acetone.

The soaps were then recrystallized from ethanol. The soaps were dissolved in ethanol at 80°C. Once all solids had dissolved, the solution was moved to an ice bath to encourage rapid crystallization. After fully cooling, the solids were filtered and washed with water, ethanol, methanol, and acetone. The samples were placed in a 90°C oven overnight to dry. The zinc palmitate required a second recrystallization to improve purity.

Zinc oxide paints were prepared by crushing the pigment to make it finer. Linseed oil was added to the pigment and mixed until uniform. The paint was spread on glass slides in a thin layer. The slides were placed in an oven at 40°C for 4 months. The paint samples were crushed at cryogenic temperatures in liquid nitrogen in a mortar and pestle to create samples for NMNR analysis.

### **4.3 Analysis of Zinc Soaps and ZnO paint**

Zinc soaps do not appear to follow the same trends as lead soaps for correlations between metal carboxylate crystal structure and carboxylate chain length. In lead soaps, the change in the symmetry of the structure around the central atom changes between octanoate and nonanoate, as observed with NMR spectroscopic parameters and IR spectroscopic parameters, as well as X-ray structural analysis. In the zinc soaps prepared here, there is little apparent difference between zinc octanoate and zinc nonanoate by NMR spectroscopy. These two materials do display differences from zinc palmitate. If there is a single change in crystal structure between the short and long chain zinc carboxylates, it likely occurs at a different chain length in the fatty acid series.

### 4.3.1 FTIR Spectroscopy

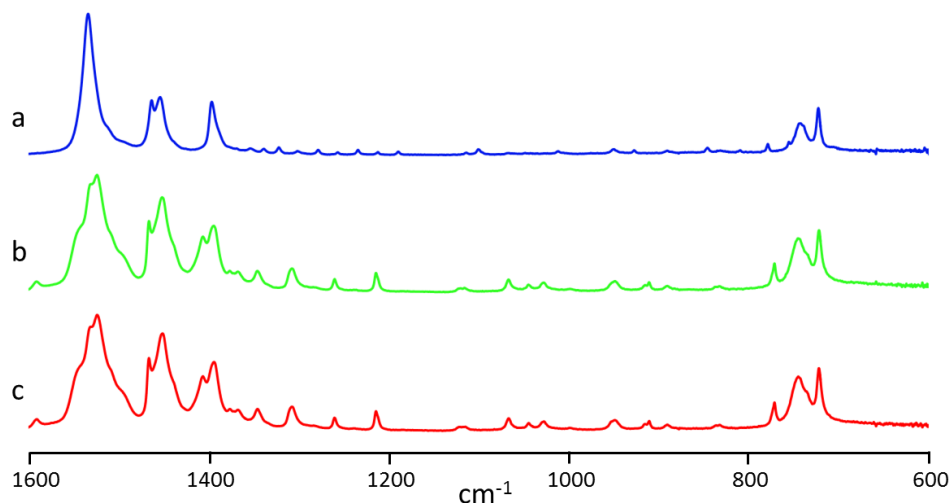


Figure 4.1 FTIR spectra of (a) Zn palmitate, (b) Zn nonanoate, (c) Zn octanoate.

The IR spectra of the zinc carboxylates are shown in Figure 4.1. The asymmetric carboxylate stretch appears as a singlet at  $1534\text{ cm}^{-1}$  for zinc palmitate, but as a multiplet, between  $1544\text{--}1525\text{ cm}^{-1}$ , for zinc octanoate and nonanoate. The position of the asymmetric stretch for the short-chain zinc carboxylates is more similar to that of the palmitate than it is for the analogous lead materials. Unlike the lead soaps, all of these compounds have consistent progression bands in the range of  $1150\text{--}1350\text{ cm}^{-1}$ . The presence of these progressions indicates the long-range order packing of the fatty acids is less affected by chain length for zinc soaps than it is for lead soaps.

### 4.3.2 Carbon-13 NMR Spectroscopy

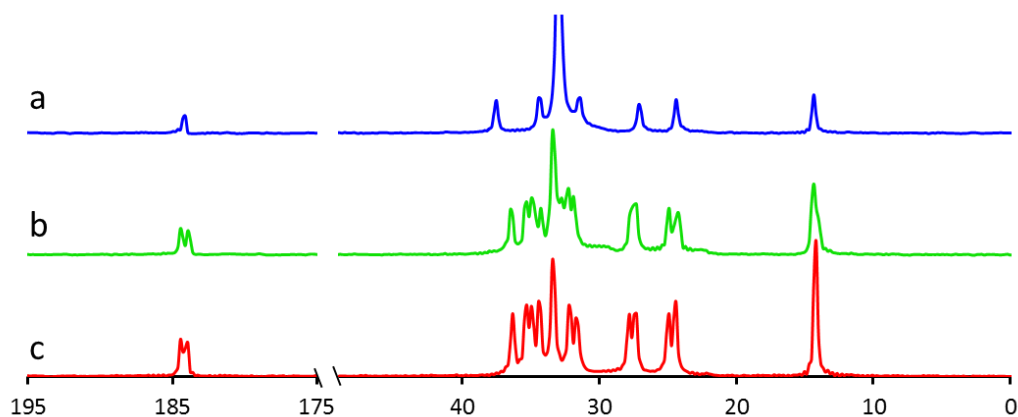


Figure 4.2  $^{13}\text{C}$  NMR spectra of (a) Zn palmitate, (b) Zn nonanoate, (c) Zn octanoate.

The carbon-13 NMR spectra of the zinc soaps are shown in Figure 4.2. Unlike the lead soaps, the carboxylate signal is a singlet for some of the zinc soaps. The short chain, zinc octanoate and nonanoate, show splitting at the carboxylate group indicating multiple possible geometries around the zinc atom. The splitting continues down-chain for the short carboxylates. In the zinc palmitate, the carboxylate signal is a single peak representing a higher symmetry around the zinc center. There is no splitting at the methyl group for the three zinc soaps in this study, showing that the two chains associated with a zinc ion have identical structures at the end.

Table 4.1 Assignments of  $^{13}\text{C}$  NMR spectra of (a) Zn octanoate, (b) Zn nonanoate, (c) Zn palmitate, shown in Figure 4.2. (all values in ppm)

	C1	C2	C3	Methyl group
Zinc Palmitate	184.1	27.1	24.4	14.4
Zinc Nonanoate	184.4, 183.9	27.4	24.9, 24.3	14.3
Zinc Octanoate	184.4, 183.9	27.8, 27.4	24.9, 24.4	14.2

The carboxylate signal of zinc palmitate appearing as a sharp singlet is beneficial for using  $^{13}\text{C}$  NMR spectroscopy to study reactivity. It is clearly separated from the palmitic acid signal, as shown in Figure 4.3, and can be easily used for quantitative measurement of the extent of reaction of the acid over the period of several days.

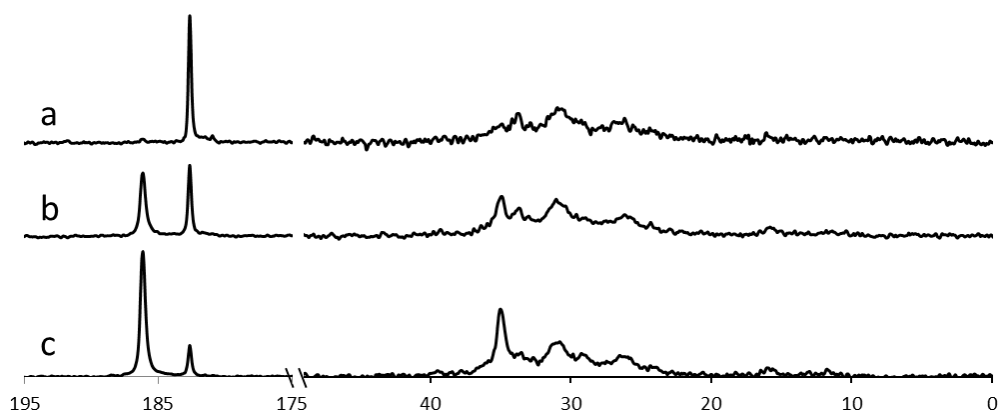


Figure 4.3. Carbon-13 NMR spectra of ZnO paint reacting with palmitic acid (a) just after mixing, (b) after substantial reaction, and (c) near the end of reaction.

#### 4.4 Implications for Future Work on Zinc Soaps

These spectra show that there may be a chain-length dependent effect in crystal formation or crystal packing of zinc soaps, similar to that in lead soaps. The full zinc carboxylate series needs to be studied to determine the nature of the chain-length dependence. In attempting to grow single crystals of zinc octanoate and nonanoate, there is a qualitative difference in the crystals formed using different solvents, which could indicate multiple structures possible for some zinc carboxylates. This aspect of the material's reactivity needs to be investigated.

Zinc(II) forms several different coordination geometries, in some cases dependent on the size of the ligand. There are examples of tetrahedral and octahedral geometries for heterocyclic ether, acid and amide complexes<sup>78</sup>, and trigonal bipyramid geometry for zinc acetylacetonate complexes<sup>79</sup>. It is possible that the central geometry is strongly dependent on ligand size, which may be reflected in the various structures formed by zinc soaps.

## Chapter 5

### STUDIES OF PIGMENTS AND MODEL PAINT SYSTEMS

#### 5.1 Basic Lead White

Basic lead white, which consists primarily of basic lead carbonate,  $2\text{PbCO}_3 \cdot \text{Pb}(\text{OH})_2$ , was one of the first artificially produced pigments in antiquity and the white colorant of choice in paintings until recently. The earliest known recorded recipe for its preparation was by Theophrastus, around 300 BCE<sup>80</sup>. Lead white is the pigment most strongly associated with the formation of lead soaps in oil-based paintings.

Despite the importance of basic lead carbonate, its crystal structure has only recently been solved using powder X-ray diffraction data<sup>81</sup>. It consists of two distinct hexagonal layers of Pb atoms (labeled A and B), stacked along [001] in a [BAA]<sub>n</sub> arrangement, where layer A is composed of Pb (Pb1 site) and CO<sub>3</sub>, and layer B is composed of Pb (Pb2 site) and OH. Consequently, there are twice as many Pb1 sites as Pb2 sites.

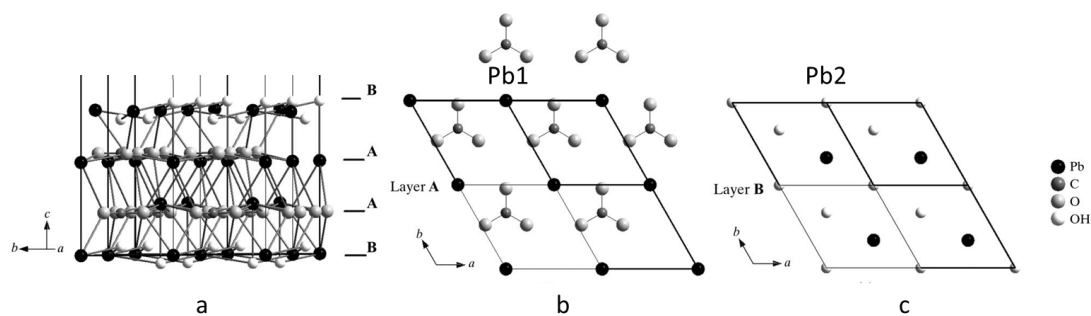


Figure 5.1 Structure of basic lead white<sup>81</sup>, showing (a) the layered structure of (b) layer A – lead carbonate and (c) layer B – lead hydroxide.

Previous attempts to study the structure of lead white (containing mainly the basic lead carbonate) by  $^{207}\text{Pb}$  SSNMR have been unsuccessful. Typically, only the significant (often up to 15% by weight) lead carbonate impurity is observed. This phase is easily detected at room temperature by directly excited MAS spectroscopy<sup>82</sup>, as well as by static  $^{207}\text{Pb}$  SSNMR experiments<sup>21c</sup>, due to its small CSA (see Figure 5.3c) and has been erroneously identified as originating from the carbonate layer of the basic lead carbonate<sup>82</sup>.

Recent progress in dynamic nuclear polarization (DNP), including instrumental improvements<sup>83</sup>, the introduction of biradical polarizing agents<sup>84</sup>, and advances in theory<sup>85</sup>, has impressively enhanced SSNMR's sensitivity, especially in the area of materials science. DNP has enabled the observation of species at low concentrations that were not accessible by conventional SSNMR in biomolecules, in polymers, and on the surfaces of catalysts, to cite a few examples<sup>86</sup>. DNP's sensitivity enhancement holds promise of the application of SSNMR to other dilute and severely mass-limited samples, such as archaeomaterials and other objects of cultural significance.

## 5.1.1 Experimental Details

### 5.1.1.1 Sample Preparation

Basic lead carbonate was purchased from Sigma Aldrich. An aged paint film was prepared by mixing lead white with 22% linseed oil, by weight. The paint was spread on glass slides and cured at room temperature for three months before it was scraped off and kept in a sealed clear jar under laboratory conditions for four years. Before the NMR measurements, the aged sample was ground under liquid nitrogen.

### 5.1.1.2 Experimental NMR Methods

All SSNMR experiments<sup>87</sup> were performed at Iowa State University in the group of Marek Pruski at 9.4 T (400 MHz for  $^1\text{H}$  and 83.7 MHz for  $^{207}\text{Pb}$ ) on a Bruker Biospin AVANCE III DNP-SSNMR spectrometer, equipped with a 263 GHz gyrotron and a low-temperature MAS probe. The samples were wet with a 16 mM solution of the TEKPol biradical<sup>84a</sup> in a 1,1,2,2-tetrachloroethane:methanol-d4 96:4 mixture, and packed in 3.2-mm sapphire rotors. Static wide-line  $^{207}\text{Pb}[^1\text{H}]$  DNP-BCP experiments were performed at a temperature of  $110 \pm 5$  K.  $^{207}\text{Pb}[^1\text{H}]$  DNP-CPMAS spectra were measured at  $105 \pm 5$  K. Conventional (non-DNP) static  $^{207}\text{Pb}$  WCPMG experiments were carried out at several temperatures ranging from 110 K to 308 K. The chemical shifts were referenced to tetramethyl lead at room temperature using a solution of DSS (4,4-dimethyl-4-silapentane-1-sulfonic acid) and the universal referencing scale<sup>88</sup>. Detailed experimental conditions are given in the figure captions.

## 5.1.2 Lead Palmitate

Lead palmitate was used to assess the performance of DNP, as its smaller span ( $740 \pm 4$  ppm) compared to that of lead white, enables the performance of CPMAS to

be assessed alongside BCP. The DNP-enhanced  $^{207}\text{Pb}[^1\text{H}]$  CPMAS and BCP spectra of lead palmitate are shown in Figure 5.2, along with their corresponding simulated spectra based on the previously published chemical-shift tensor parameters<sup>57a</sup>.

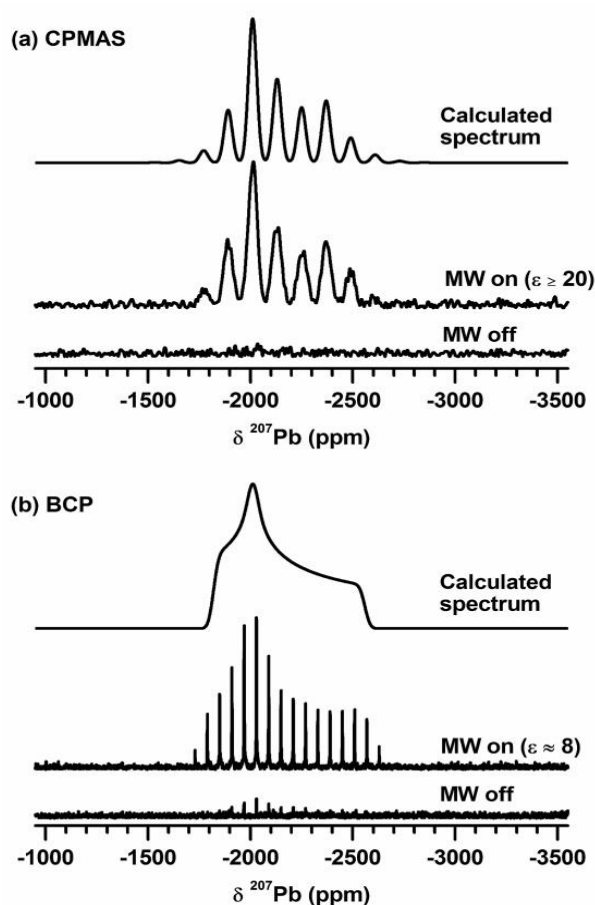


Figure 5.2  $^{207}\text{Pb}[^1\text{H}]$  CPMAS (a) and  $^{207}\text{Pb}[^1\text{H}]$  BCP (b) spectra of lead palmitate, acquired with microwave radiation on and off. In contrast to lead white, the spectra could be easily acquired without stepping the carrier frequency. Simulated lines for the DNP-CPMAS and DNP-BCP spectra are shown at the top. In (a) the MAS rate was  $\nu_R = 10$  kHz, the contact time was 10 ms, and 256 scans were acquired with a recycle delay of 8 s; in (b) the adiabatic pulses used for CP and CPMG refocusing were the same as those used for lead white, and 64 scans were acquired with a recycle delay of 8 s.

Both experiments lead to sizeable enhancements of the  $^{207}\text{Pb}$  SSNMR spectra. The observed enhancement factors are  $\varepsilon \geq 20$  and  $\varepsilon \approx 8$  for the CPMAS and BCP experiments, respectively. The enhancement factor is approximately a factor of 2 greater for the lead soap than it is for lead white, which can, at least in part, be attributed to the higher proton density of the alkyl chain compared to the  $\text{Pb}(\text{OH})_2$  layer.

### 5.1.3 Basic Lead White and DNP NMR Spectroscopy

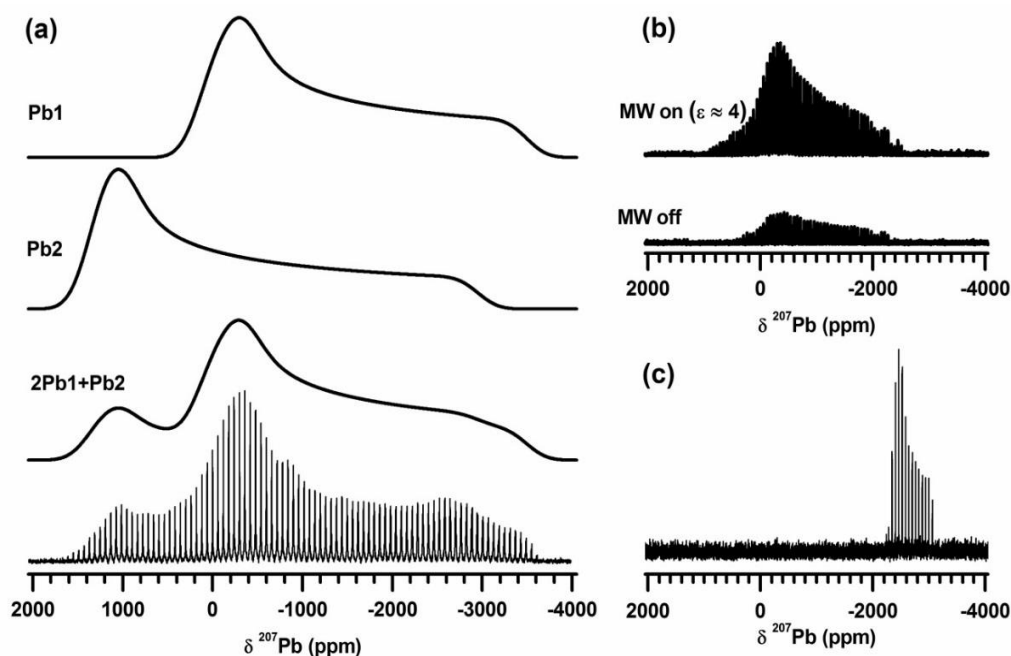


Figure 5.3.  $^{207}\text{Pb}$  SSNMR spectra of lead white. (a)  $^{207}\text{Pb}[^1\text{H}]$  DNP-BCP spectrum (bottom) and its simulated decomposition into signals assigned to the Pb1 and Pb2 sites. The adiabatic inversion (CP) pulse swept over 250 kHz for a period of 20 ms while the refocusing CPMG pulses lasted 50  $\mu\text{s}$  and was swept over 500 kHz. The experimental line shape is composed of eight subspectra, each measured with 64 scans and a recycle delay of 6 s. A single subspectrum acquired with and without the application of microwaves is shown in (b). (c)  $^{207}\text{Pb}$  WCPMG spectrum featuring solely the lead carbonate resonance. This spectrum was acquired at 308 K, using 128 scans and a recycle delay of 8 s.

Table 5.1  $^{207}\text{Pb}$  chemical-shift tensor components (ppm) of basic lead carbonate, determined at 105 K.

Pb site	$\delta_{11}^a$	$\delta_{22}^a$	$\delta_{33}^a$	$\delta_{\text{iso}}$	$\Omega$	$\kappa$
Pb (1)	160	-310	-3500	-1216	3660	0.74
Pb (2)	1400	1050	-2950	167	4350	0.84

<sup>a</sup>The uncertainty in each tensor component ( $\delta_{11}$ ,  $\delta_{22}$ , and  $\delta_{33}$ ; which are ordered as:  $\delta_{11} \geq \delta_{22} \geq \delta_{33}$ ) is estimated to be  $\sim 10$  ppm, which gives an estimated uncertainty in the isotropic shift ( $\delta_{\text{iso}} = (\delta_{11} + \delta_{22} + \delta_{33})/3$ ) of  $\sim 10$  ppm. The estimated uncertainty in the span ( $\Omega \approx \delta_{11} - \delta_{33}$ ) is  $\sim 14$  ppm. The uncertainty in the skew ( $\kappa \approx 3(\delta_{22} - \delta_{33})/\Omega$ ) is  $\sim 0.03$ .

The  $^{207}\text{Pb}$  DNP-BCP spectrum of lead white is shown in Figure 5.3a. The spectrum spans more than 5000 ppm, and has been acquired in a piecewise manner using the variable offset cumulative spectrum (VOCS) method<sup>89</sup>. In agreement with the crystallographic data for basic lead carbonate, the spectrum is reproduced well when fit to two sites, having distinct chemical-shift parameters (Figure 5.3a and Table 5.1), with an intensity ratio of  $\sim 2:1$ . From this intensity ratio the two components are straightforwardly assigned to the abovementioned Pb1 (lead carbonate layer, A) and Pb2 (lead hydroxide layer, B) sites in the crystal structure. These two sites feature different cross-polarization rates, which reflect their respective proximities to hydrogen atoms. Although the precise hydrogen positions are currently unknown, the Pb2 sites are expected to reside closer to the hydroxyl moieties than the Pb1 sites (The relevant Pb1–O and Pb2–O distances are reported to be 2.36 Å and 1.95 Å, respectively<sup>81</sup>.) and are thus expected to have faster CP kinetics. The BCP signal intensities as a function of the contact time, measured for the highest-intensity singularity for each site, are shown in Figure 5.4. The CP build-up rate is faster for Pb2, further supporting the signal assignment.

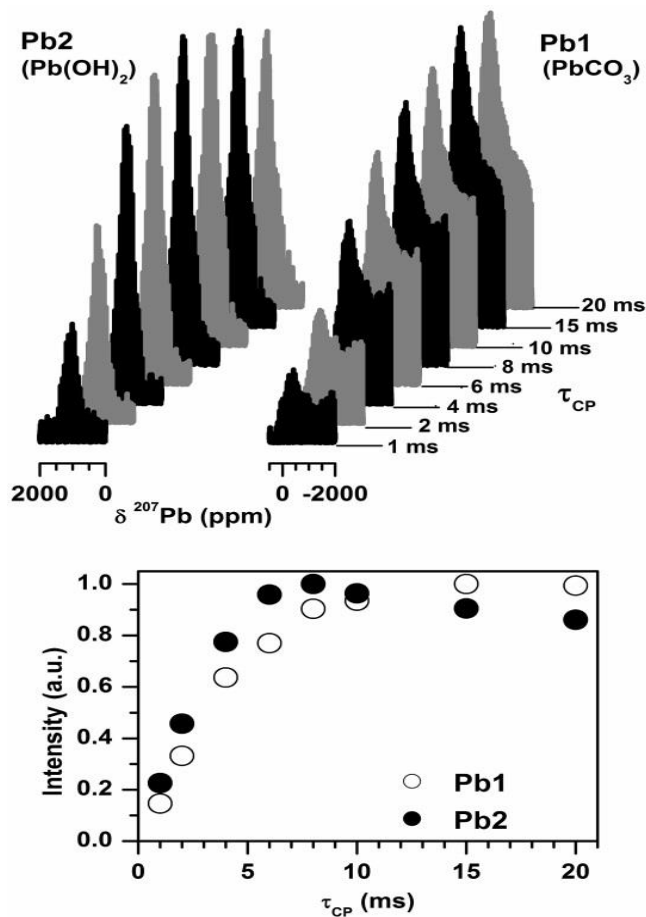


Figure 5.4 The <sup>207</sup>Pb[<sup>1</sup>H] DNP-BCP build-up curves as a function of the CP contact time, measured for the Pb1 and Pb2 sites at 110 K.

The relatively low DNP enhancement factor of  $\epsilon \sim 4$ , estimated by comparing the signal intensity in the presence and absence of microwave irradiation (Figure 5.3b), is caused by the difficulty to satisfy the cross-effect condition in static samples<sup>54, 85b</sup>, and the nonporous nature of the material, which forces dependence on spin diffusion to polarize the bulk of the particles<sup>90</sup> The use of a <sup>207</sup>Pb[<sup>1</sup>H] CPMAS technique, both with and without the application of microwaves, suppresses the signals from <sup>207</sup>Pb nuclei in hydrogen-free regions of the sample, namely lead carbonate. In

agreement with previous work, this lead carbonate phase is readily detected by a  $^{207}\text{Pb}$  WCPMG experiment (Figure 5.3c), carried out at 308 K using a direct-excitation scheme without the application of DNP. Attempts to perform a similar BCP measurement at 308 K yielded no signal for either phase.

To investigate the disappearance of basic lead carbonate signals near room temperature, a series of  $^{207}\text{Pb}$  WCPMG spectra were collected at five temperatures ranging from 110 K to 308 K (Figure 5.5a). As the temperature is elevated, the spikelets from the lead white phase broaden and eventually disappear in the baseline, demonstrating that the lack of signal is due to a decrease of  $T_2$  of the Pb1 and Pb2 sites. Concurrently, the line width of the  $^1\text{H}$  signal decreases with increasing temperature (Figure 5.5b), suggesting that the accelerated decoherence of the  $^{207}\text{Pb}$  magnetization is attributable to increased mobility in the solid<sup>43</sup>. A possible way to detect both the basic lead carbonate and lead carbonate signals in a single experiment might be the measurement of the  $^{207}\text{Pb}$  WCPMG spectrum at low temperature using a biradical-free sample. The sensitivity of such an experiment is much lower than that of a DNP-BCP experiment (for Pb1 and Pb2 by a factor of  $\sim 30$ , in terms of experimental time), making it impractical for size-limited samples.

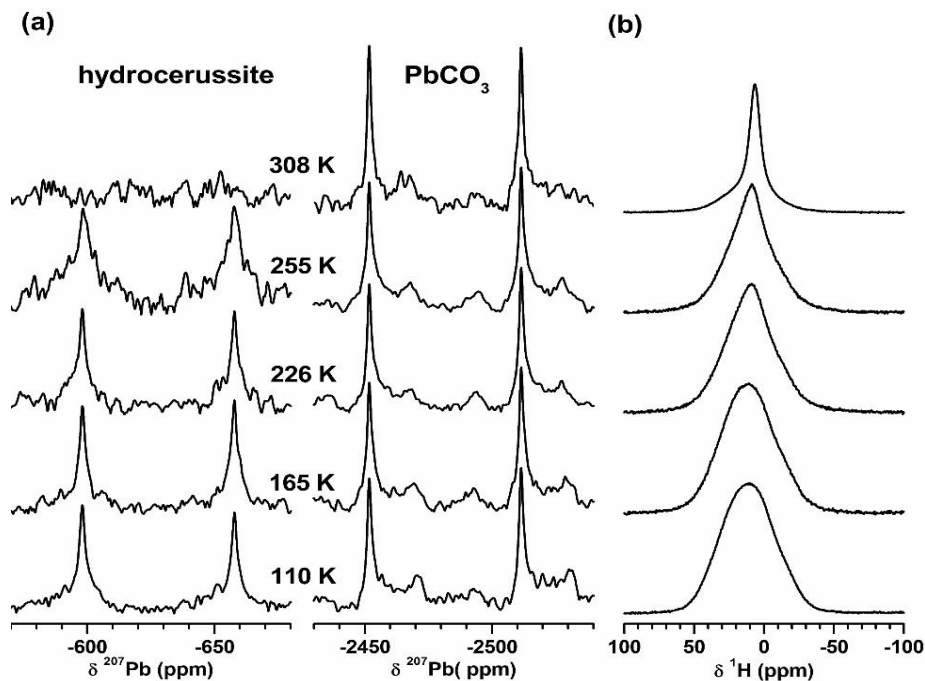


Figure 5.5 Sections of the  $^{207}\text{Pb}$  WCPMG (a) and  $^1\text{H}$  spin echo (b) spectra of lead white measured at different temperatures. All  $^{207}\text{Pb}$  spectra were obtained using the same conditions as in Figure 5.3, with a recycle delay of 15 s and a greater number of scans: 256 scans at 110 K, 165 K, and at 308 K, 512 scans at 226 K, and 768 scans at 255 K. The  $^1\text{H}$  spin echo spectra were obtained under a static condition, with a half-echo period of 50  $\mu\text{s}$ , a recycle delay of 15 s and 16 scans. The spectra in each column (with the exception of basic lead carbonate at 308 K) were normalized to constant height to eliminate the effect of the varying numbers of scans, Boltzmann polarizations,  $T_1$  relaxation times and RF efficiencies at the different temperatures.

#### 5.1.4 DNP NMR Spectroscopy of Paint with Pb Soap Formations

Previous attempts at observing the formation of lead soaps in aged paint films using  $^{207}\text{Pb}$  SSNMR were unsuccessful, primarily due to the low amounts of lead soaps present, as well as the aforementioned lead carbonate impurity. DNP-BCP may be the ideal  $^{207}\text{Pb}$  SSNMR technique for this application, given that 1) it completely

suppresses the signal from the lead carbonate phase and 2) it selectively enhances the signal from the lead soap.

Figure 5.6a shows the  $^{207}\text{Pb}[^1\text{H}]$  DNP-BCP spectrum of a lead white/linseed oil (78/22 wt%) paint film that had been aged for four years at room temperature and relative humidity to mimic the natural aging process of traditional lead oil paints. The aged film primarily displays the spectrum of basic lead carbonate, with a superimposed signal that we assign to decomposition products. By subtracting the spectrum of lead white from that of the aged film, the spectrum of the decomposition products is isolated (Figure 5.6b). Although a large fraction of that signal may be attributed to lead carbonate, now detectable by CP due to the proton-rich oil matrix, small additional contributions are still discernible (indicated by the grey arrow in Figure 5.6b) which agree with the CS tensor parameters of Pb palmitate (see Figure 5.2) and other lead carboxylates<sup>91</sup>. Although this weak signal does not allow a definitive assignment, its position and breadth suggests the formation of long-chain lead carboxylates during the paint aging process.

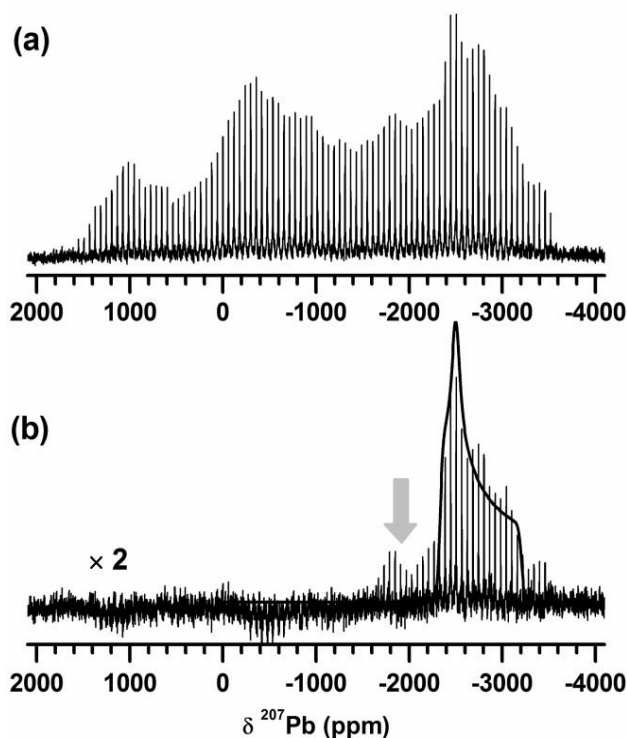


Figure 5.6 (a)  $^{207}\text{Pb}[^1\text{H}]$  DNP-BCP spectrum of aged paint film measured at 108 K. Subtracting the signals from lead white results in spectrum (b), revealing the signal from the decomposition products; the arrow shows the signal corresponding to a lead soap. The pulse parameters were identical to those used for lead white, described in Figure 5.3.

### 5.1.5 Conclusions about Lead White Pigment Analysis by DNP-NMR Spectroscopy

DNP-enhanced  $^{207}\text{Pb}$  ssNMR measurements allowed observation, for the first time, of  $^{207}\text{Pb}$  ssNMR signals from the basic lead carbonate phase in the lead white pigment. In agreement with crystallographic data, the spectral fitting reveals the existence of two Pb sites with an intensity ratio of  $\sim 2:1$ , corresponding to the carbonate and hydroxide layers. Additionally, the DNP enhancement in a common lead soap (lead palmitate) is twice as large as that for basic lead carbonate, which facilitates its detection in aged paint films. This new methodology allows detection,

also for the first time, of the formation of a lead soap in an aged paint film by  $^{207}\text{Pb}$  SSNMR spectroscopy. These insights could not have been obtained by conventional SSNMR methodology.

## 5.2 Lead Tin Yellow Type I

Lead tin yellow type 1 (LTY-I) was a very common pigment from the 15<sup>th</sup> to early 18<sup>th</sup> centuries<sup>92</sup> consisting of lead and tin oxides. This pigment is a common source of lead ions<sup>17b</sup>, second only to basic lead white, in the formation of lead soaps. In recent years, characterizing the reactivity of lead stannate,  $\text{Pb}_2\text{SnO}_4$ , with fatty acids has been increasingly recognized as a key issue in understanding soap formation in paintings<sup>17b,93</sup>.

LTY-I is prepared by heating a mixture of massicot (orthorhombic  $\text{PbO}$ ) or minium ( $\text{Pb}_3\text{O}_4$ ) with tin(IV) oxide ( $\text{SnO}_2$ ). Depending on the manufacturing conditions, this process may lead to mixtures of tin oxides. Commercial sources report the empirical formula of the pigment as  $\text{PbSn}_x\text{O}_y$ . It is not clear whether this ambiguous stoichiometry implies the presence of distinct phases or a solid solution. A similar ambiguity exists concerning the pigment as used in works of art.

Single crystals of  $\text{Pb}_2\text{SnO}_4$  have been grown<sup>94</sup>, and powder X-ray diffraction and Raman data have been published<sup>95</sup>, showing scant information on the existence and nature of more complex phases. Yet, it is these minor components that are assumed to react with the free fatty acids in the binding medium of oil paintings<sup>17b</sup>. Therefore, ssNMR characterization of LTY-I is important for determining the chemical species present in LTY-I, and which species are responsible for soap formation. We use model paint samples to study the reactivity of LTY-I, because only microscopic heterogeneous samples can be obtained from paintings.

## 5.2.1 Experimental Details

### 5.2.1.1 Sample Preparation

LTY-I 1010 Light was purchased from Kremer Pigments (Germany). For the paint film, 2 grams of LTY-I were mixed with 1 gram of linseed oil and 0.5 gram of palmitic acid. The wet paint film formed a thick paste that was spread on three slides and aged under laboratory conditions for 8 months (approximately 20°C and 55% relative humidity). The sample was packed in a rotor for three weeks, before obtaining the spectra, showing full consumption of the palmitic acid to within 5%. The reaction was monitored using  $^{13}\text{C}$  ssNMR spectroscopy by integrating the carboxyl peaks of palmitic acid and lead palmitate.

Powder X-ray diffraction<sup>72</sup> was used to confirm the geometry of our sample of LTY-I<sup>94, 96</sup>. Elemental analysis was performed by energy-dispersive X-ray spectrometry in the scanning electron microscope (SEM-EDS)<sup>72</sup>. The atom percentages of lead and tin are normalized to 100%. These values, along with the signal percentages from NMR spectra, were used to calculate the mole percentage of each species in the LTY-I sample.

### 5.2.1.2 Experimental NMR Methods

$^{207}\text{Pb}$ ,  $^{119}\text{Sn}$ , and  $^{13}\text{C}$  ssNMR spectra were recorded at 11.75 tesla (104.63 MHz  $^{207}\text{Pb}$  frequency, 186.50 MHz  $^{119}\text{Sn}$  frequency, and 125.76 MHz  $^{13}\text{C}$  frequency) with a standard Bruker 4-mm probe. Solid lead nitrate,  $\text{SnCl}_2$  in HCl, and glycine were used as secondary external references for the  $^{207}\text{Pb}$ ,  $^{119}\text{Sn}$ , and  $^{13}\text{C}$  spectra, respectively. A plot of spinning speed versus isotropic chemical shift of lead nitrate was obtained to compensate for the change in chemical shift that results from the temperature increase caused by friction during spinning.

$^{207}\text{Pb}$  spectra were acquired using direct excitation and high-power decoupling, with spin-temperature alternation and magic-angle spinning (STA/MAS) at 11 and 12 kHz to obtain isotropic chemical shifts.  $^{207}\text{Pb}$  WURST-CPMG spectra of the samples were recorded using the parameters of MacGregor et al varying the carrier frequencies by a multiple of the spiklet separation (981.934ppm) between spectra<sup>60</sup>. The collected WURST-CPMG spectra were superimposed to form the final spectrum.

$^{119}\text{Sn}$  spectra were acquired using direct excitation with STA/MAS at 5 and 12 kHz with 1024 and 564 scans, respectively.  $^{13}\text{C}$  spectra were acquired using cross polarization with MAS at 12 kHz.

The analysis of the  $^{207}\text{Pb}$  chemical-shift tensors was performed by fitting the WURST-CPMG envelope using the previously published tensor for minium<sup>97</sup>. The values of the isotropic chemical shifts were determined from STA/MAS spectra, with the help of DFT calculations. Fits to the WURST-CPMG envelopes were aided by simulation of the powder pattern with the program WSOLIDS<sup>98</sup>. The  $^{119}\text{Sn}$  chemical-shift tensors were determined using the isotropic chemical shifts determined by spinning at 12 kHz and fitting the sideband pattern from the spectrum at 5 kHz using HBA 3.1<sup>98</sup>. The chemical shift tensors obtained from these fits were used to determine the relative mole percentage of each species present in the mixed materials.

### 5.2.1.3 Computational Methods

All calculations in this section were performed by my colleague, Fahri Alkan.

All density functional computations were performed using the Amsterdam Density Functional (ADF v2013) program package<sup>99</sup>. The calculations were carried out at the DFT/BP86 level<sup>100</sup>. For the calculations, a molecular-cluster approach was used in which the clusters are formed from the experimental X-ray geometry. The

molecular clusters are shown in Figure 5.7. For clusters I and II, the TZ2P/all-electron (AE) basis set was used for all atoms in the cluster.

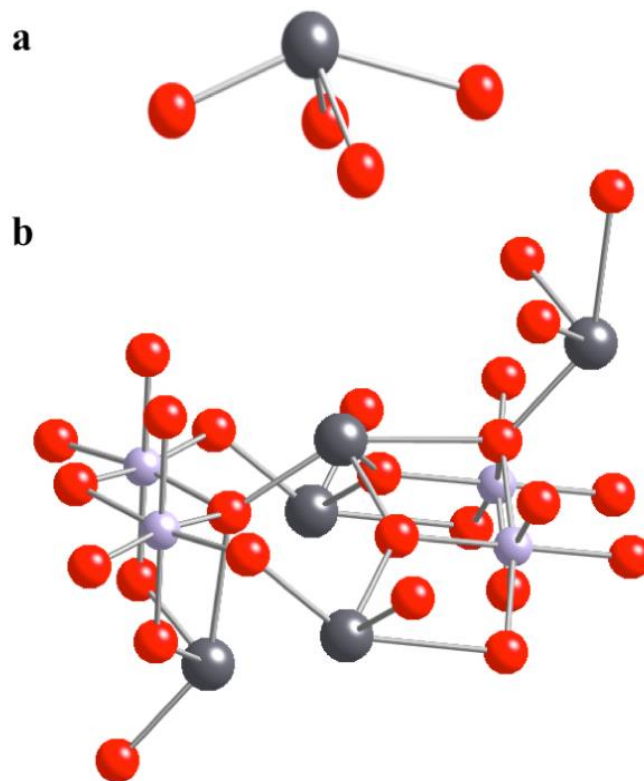


Figure 5.7 Molecular clusters of lead-tin yellow employed in the computational investigations, lead (dark gray), oxygen (red) and tin (light gray). Cluster I (a) and cluster II (b).

For all calculations, relativistic effects were included in the ZORA Hamiltonian at the spin-orbit level<sup>101</sup>. The NMR parameters were computed within the GIAO formalism<sup>102</sup>. To deal with dangling bonds and resulting self-consistent-field (SCF) convergence problems, the terminal oxygen atoms were saturated with

hydrogens. The reported chemical shifts are referenced to the extrapolated intercept of the best-fit correlation line for calculations of the principal components of the chemical shielding of clusters of  $\alpha$ - and  $\beta$ -PbO (7933 ppm).

### 5.2.2 Determination of the $^{207}\text{Pb}$ Chemical-Shift Tensors

Crystallographically,  $\text{Pb}_2\text{SnO}_4$  belongs to the  $\text{Pbam}$  space group, with two distinct lead sites (labeled Pb(1) and Pb(2)) that theoretically give rise to two distinct NMR signals<sup>95a</sup>. The local geometry of the two sites is similar, as both are coordinated to four oxygen atoms in a hemi-directed arrangement (Figure 5.8a). There are small differences in the Pb-O bond lengths and O-Pb-O angles, listed in Table 5.2.

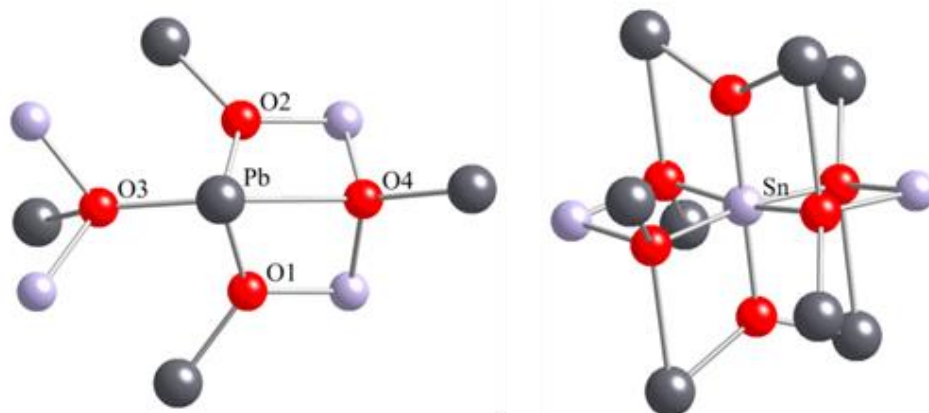


Figure 5.8 Structure of  $\text{Pb}_2\text{SnO}_4$  showing the coordination environment around the (a) lead (dark gray) and (b) tin (light gray) sites. Oxygen is shown in red. Pb(1) and Pb(2) are structurally similar, and both would have similar environments with slight differences in bond lengths and bond angles.

Table 5.2 Selected bond distances (Å) and angles (degree) for the first co-ordination shells of Pb(1) and Pb(2) in Pb<sub>2</sub>SnO<sub>4</sub>

	Pb(1)	Pb(2)
Pb-O1	2.15	2.24
Pb-O2	2.15	2.24
Pb-O3	2.33	2.29
Pb-O4	2.78	2.80
O1-Pb-O2	94.14	89.22
O1-Pb-O3	90.64	88.64
O2-Pb-O3	90.64	88.64

The <sup>207</sup>Pb STA/MAS spectrum of LTY-I, with the carrier frequency set at 1650 ppm, pointed to a broad powder pattern that was not uniformly excited and the spinning sideband pattern for the two lead sites could not be resolved. This was true for MAS spinning speeds of 11 and 12 kHz. However, when the carrier was moved to -1000 ppm, peaks for an impurity were clearly visible. The minium Pb(IV) site was identified with an isotropic chemical-shift of  $-1102 \pm 4$  ppm<sup>97, 103</sup>. Minium is a starting material for the synthesis of LTY-I as well as a photodegradation product of the pigment<sup>95c</sup>.

WURST-CPMG spectra were recorded piecewise by shifting the carrier frequency an integer multiple of the spikelet spacing to achieve uniform excitation over a region for determination of the <sup>207</sup>Pb chemical-shift tensors. Figure 5.9 shows the fit of the total spectrum, which consists of overlapping chemical-shift tensors of four lead species, two with similar chemical-shift tensors assigned to Pb<sub>2</sub>SnO<sub>4</sub> and the Pb(II) and Pb(IV) sites of the minium<sup>97</sup> impurity that have been previously reported. The two tensors arising from the dominant Pb<sub>2</sub>SnO<sub>4</sub> in LTY-I were refined by determining the possible isotropic chemical shifts from STA/MAS experiments and

DFT calculations of the skew. The experimentally determined chemical-shift tensors are reported in Table 5.3. The integrated intensities for the species in the simulated fit of the WURST-CPMG spectrum gave  $92.5 \pm 1.5$  % of the lead as  $\text{Pb}_2\text{SnO}_4$  and  $7.5 \pm 1.5$  % as minium.

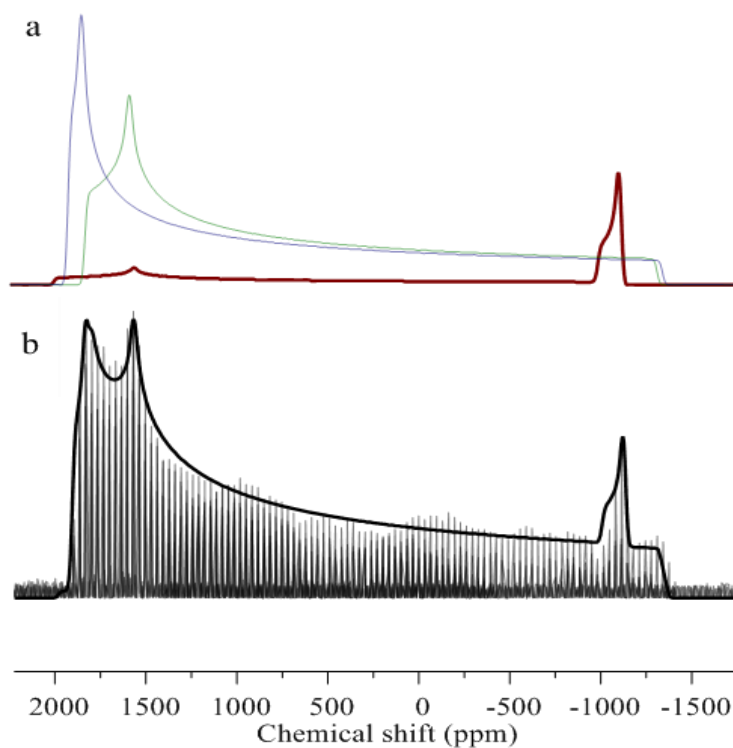


Figure 5.9 (a) Simulated spectrum for each of the individual components in the sample;  $\text{Pb}_2\text{SnO}_4$  (blue and green) and the impurity minium (red). (b)  $^{207}\text{Pb}$  spectrum of LTY-I obtained with WURST-CPMG, showing four lead species. (The low intensity,  $\text{Pb}^{4+}$ , site of minium is assumed based on the presence of the  $\text{Pb}^{2+}$  site and the previously published spectrum.)

### 5.2.3 Calculation of $^{207}\text{Pb}$ Chemical-Shift Tensors

In Table 5.3, calculated NMR parameters for different clusters that represent  $\text{Pb}_2\text{SnO}_4$  (Figure 5.7) at the all-electron (AE) level of theory are tabulated.

Calculations on the cluster that includes only the first co-ordination shell (cluster I) fail to reproduce the experimentally determined chemical-shift principal components, as expected<sup>104</sup>. The first co-ordination shell cluster is not large enough to describe the interactions necessary for an accurate calculation of the NMR parameters. Cluster II describes the effects of higher co-ordination shells, for which the calculated parameters are improved significantly over the parameters of cluster I.

Another important aspect of this investigation is the assignment of experimental NMR parameters to a lead site by using general symmetry arguments that correlate the ssNMR spectroscopy with computational results. From the experimentally resolved parameters, the most obvious difference is the resonance position of  $\delta_{22}$  relative to  $\delta_{11}$ . For the experimental tensor of lead site B,  $\delta_{11}$  and  $\delta_{22}$  are close to each other, with a difference in value of only 75 ppm. For the experimental tensor of lead site A, this difference is 250 ppm, mostly due to a shift of  $\delta_{22}$ . From a comparison of the calculated parameters of  $\text{Pb}_2\text{SnO}_4$  for both clusters, the difference between  $\delta_{11}$  and  $\delta_{22}$  is larger for the Pb(1) site than for Pb(2). The difference is particularly obvious for cluster II where  $|\delta_{11} - \delta_{22}|$  is 182 ppm for Pb(1) and 68 ppm for Pb(2). Thus, we make the assignment of Pb(1) and Pb(2) to experimental sites A and B, respectively.

Table 5.3 Calculated and experimental principal components of the  $^{207}\text{Pb}$  chemical-shift tensors of  $\text{Pb}_2\text{SnO}_4$ .

<b>Model clusters</b>	$\delta_{11}$ (ppm)	$\delta_{22}$ (ppm)	$\delta_{33}$ (ppm)	$\delta_{\text{iso}}$ (ppm)	$\Omega$ (ppm)	$\kappa$
Experiment Site A	1810 $\pm$ 7	1565 $\pm$ 10	-1335 $\pm$ 20	690 $\pm$ 23	3145 $\pm$ 21	0.84 $\pm$ 0.02
Experiment Site B	1903 $\pm$ 7	1828 $\pm$ 7	-1365 $\pm$ 25	789 $\pm$ 27	3268 $\pm$ 26	0.95 $\pm$ 0.03
<b>Cluster-I</b>						
Pb(1)	-416	-871	-2181	-1156	1765	0.48
Pb(2)	-617	-946	-2023	-1195	1445	0.53
<b>Cluster-II</b>						
Pb(1)	1987	1805	-1145	882	3132	0.88
Pb(2)	1802	1734	-1206	777	3008	0.95
Span ( $\Omega$ ) and skew ( $\kappa$ ) were calculated. $\Omega =  \delta_{33} - \delta_{11} $ and $\kappa = 3*(\delta_{\text{iso}} - \delta_{22})/\Omega$ .						

As mentioned earlier, the local X-ray-derived structures of the two lead sites are similar. The structure around Pb(1) is illustrated in Figure 5.8a. Because the differences in the two coordination environments are due to differences in the bond lengths and angles, a similar picture can be drawn for Pb(2). From the local structure of Pb(2), it is seen that O1, O2 and O3 have a quasi- $C_{3v}$  symmetry around the lead center, which is perturbed by the presence of O4. Therefore, one would expect the NMR parameters of Pb(2) to deviate slightly from the condition  $\delta_{11} = \delta_{22} > \delta_{33}$  expected for perfect  $C_{3v}$  symmetry. The symmetry perturbation is larger for Pb(1) than for Pb(2), so the deviation would be expected to be larger for Pb(1). This expectation is confirmed by the calculations, as seen for the sufficiently large cluster II.

#### 5.2.4 Determination of $^{119}\text{Sn}$ Chemical-Shift Tensors

The  $^{119}\text{Sn}$  spectrum of LTY-I was recorded with the STA/MAS sequence at 12 kHz and 5 kHz (Figure 5.10). Two tin species are present, one is the tin site of  $\text{Pb}_2\text{SnO}_4$  and the other is the tin site of  $\text{SnO}_2$ , one of the starting materials for the synthesis of LTY-I. As seen in Figure 5.8, the coordination geometry around the tin site in  $\text{Pb}_2\text{SnO}_4$  is close to spherical symmetry. This is reflected in the principal components of the chemical-shift tensor derived from a fit of the spectrum in Figure 5.10, showing a small span indicative of a nearly spherically symmetric environment. The principal components of the  $\text{Pb}_2\text{SnO}_4$  chemical-shift tensors are given in Table 5.4. They were determined by fitting the sideband pattern at 5 kHz with the STA/MAS experiment and the isotropic chemical shifts obtained at 12 kHz. The tensor determined for  $\text{SnO}_2$  is in agreement with various literature reports that the isotropic chemical shift is  $-604 \pm 1$  ppm with spans from 121-136 ppm<sup>105</sup>.

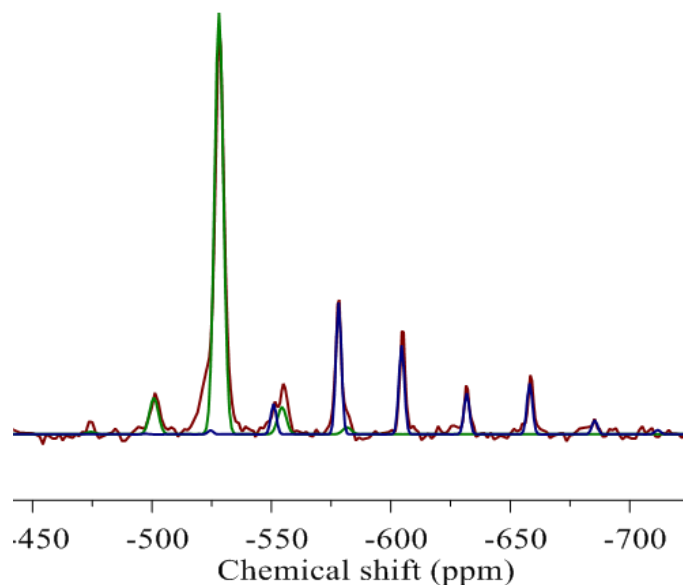


Figure 5.10 Experimental  $^{119}\text{Sn}$  STA/MAS with proton decoupling spectrum (red) of the LTY-I sample recorded on a 500 MHz magnet, showing unreacted starting material  $\text{SnO}_2$ . The percentages of the two tin species were determined using MAS simulations in WSOLIDS with  $64\pm 2\%$  for  $\text{Pb}_2\text{SnO}_4$  (green) and  $36\pm 2\%$  for  $\text{SnO}_2$  (blue).

Table 5.4 Principal components of the  $^{119}\text{Sn}$  chemical-shift tensors of species found in lead-tin yellow I.

Material	$\delta_{11}$ (ppm)	$\delta_{22}$ (ppm)	$\delta_{33}$ (ppm)	$\delta_{\text{iso}}$ (ppm)	$\Omega$ (ppm)	$\kappa$
$\text{SnO}_2$	$-558 \pm 3$	$-566 \pm 4$	$-692 \pm 5$	$-605 \pm 4$	$134 \pm 6$	$0.87 \pm 0.09$
$\text{Pb}_2\text{SnO}_4$	$-515 \pm 4$	$-517 \pm 5$	$-556 \pm 7$	$-529 \pm 5$	$41 \pm 6$	$0.88 \pm 0.14$

The integrated intensities of the two species in the simulation of the  $^{119}\text{Sn}$  STA/MAS spectrum (Figure 5.10) are  $64 \pm 2\%$  tin as  $\text{Pb}_2\text{SnO}_4$  and  $36 \pm 2\%$  as  $\text{SnO}_2$ . Using the fits of the  $^{207}\text{Pb}$  WURST-CPMG and  $^{119}\text{Sn}$  STA/MAS spectra, along with the elemental atom percentages determined by SEM-EDS, the mole percentages of the molecular species in the sample were calculated, as shown in Table 5.5. These results

indicate that for every mole of  $\text{Pb}_2\text{SnO}_4$ , there is  $0.054 \pm 0.011$  mole of  $\text{Pb}_3\text{O}_4$  present in this LTY-I sample, and that for every mole of  $\text{Pb}_2\text{SnO}_4$ , there is  $0.56 \pm 0.04$  mole of  $\text{SnO}_2$ . From NMR spectroscopy, no other species are detected.

Table 5.5 Normalized mole percentages of lead and tin as determined from SEM-EDS and NMR spectroscopy.

	Method	Lead	Tin
LTY-I	SEM-EDS	$56.3 \pm 0.3$	$43.7 \pm 0.4$
$\text{Pb}_2\text{SnO}_4$		$52.1 \pm 0.9$	$28.0 \pm 0.9$
$\text{Pb}_3\text{O}_4$	NMR calculated	$4.2 \pm 0.8$	
$\text{SnO}_2$			$15.7 \pm 0.9$

\*Calculated from the signal % in the NMR spectrum and the SEM-EDS results

### 5.2.5 Reaction of LTY-I with Palmitic Acid

The soap formation process occurs over many years in cultural heritage objects, but can be induced by addition of free fatty acid when preparing paint films to investigate the chemistry of LTY-I.  $^{13}\text{C}$  and  $^{207}\text{Pb}$  NMR show the formation of lead palmitate, (Figure 5.11) in agreement with previous measurements. The carboxyl region of Figure 5.11a indicates almost complete conversion of palmitic acid (180.4 ppm) to lead palmitate (doublet - 182.6, 183.8 ppm)<sup>18, 93</sup>. The  $^{207}\text{Pb}$  spectrum (Figure 5.11b) shows that minium is still observable, although the amount of palmitate formed (0.97 mmoles of lead) should have exhausted the minium available (0.45 mmoles of lead) if it were the only source of lead. Table 5.6 reports the  $^{207}\text{Pb}$  NMR signal percentages of  $\text{Pb}_2\text{SnO}_4$  and  $\text{Pb}_3\text{O}_4$  before and after reaction.

Table 5.6 NMR signal percentages before and after reaction.

	Before Reaction		After Reaction	
	$^{207}\text{Pb}$	$^{119}\text{Sn}$	$^{207}\text{Pb}$	$^{119}\text{Sn}$
$\text{Pb}_2\text{SnO}_4$	$92.5 \pm 1.5$	$64 \pm 2$	$86 \pm 2$	$55 \pm 2$
$\text{Pb}_3\text{O}_4$	$7.5 \pm 1.5$		$14 \pm 2$	
$\text{SnO}_2$		$36 \pm 2$		$45 \pm 2$

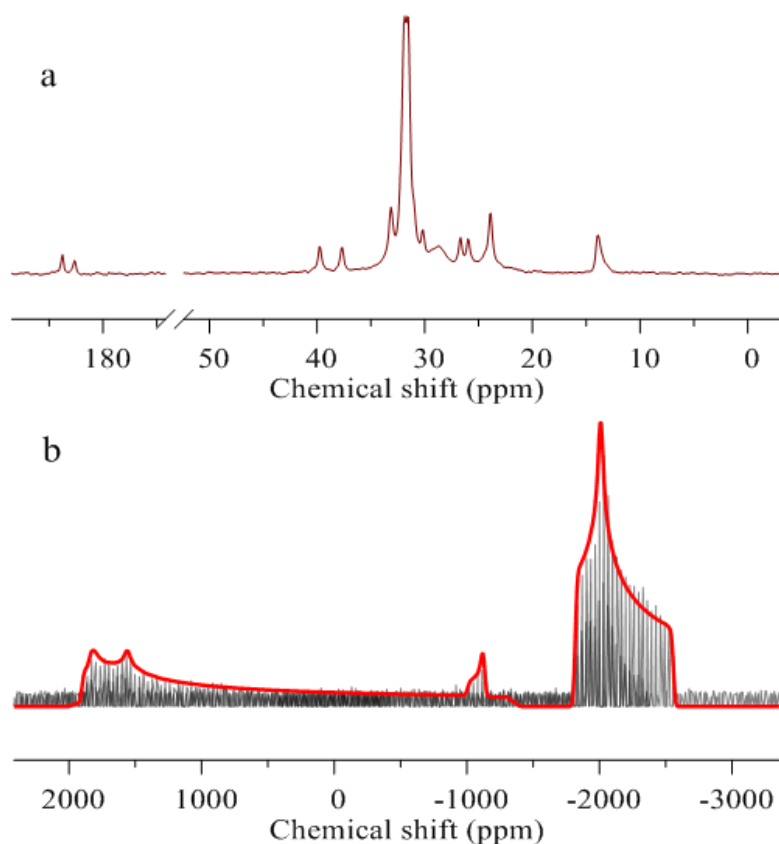


Figure 5.11 NMR spectra of the LTY-I paint film containing free palmitic acid. (a)  $^{13}\text{C}$  MAS NMR spectrum, showing lead palmitate formation by the appearance of peaks at 182.6 and 183.8 ppm. (b)  $^{207}\text{Pb}$  WURST-CPMG spectrum, showing in addition to  $\text{Pb}_2\text{SnO}_4$ , lead palmitate ( $\delta_{\text{iso}} = -2131$  ppm) and minium ( $\delta_{\text{iso}} = -1102$  ppm).

The  $^{119}\text{Sn}$  spectrum is simpler compared to the  $^{207}\text{Pb}$  spectrum of LTY-I, because the chemical-shift tensors of the tin species have smaller spans, making it easier to obtain spectra. Comparison of the relative intensities in the  $^{119}\text{Sn}$  spectrum of unreacted LTY-I with relative intensities in the  $^{119}\text{Sn}$  spectrum of the sample after reaction with palmitic acid, shows that  $\text{Pb}_2\text{SnO}_4$  is a source of lead to produce lead palmitate, Figure 5.12 and Table 5.6.

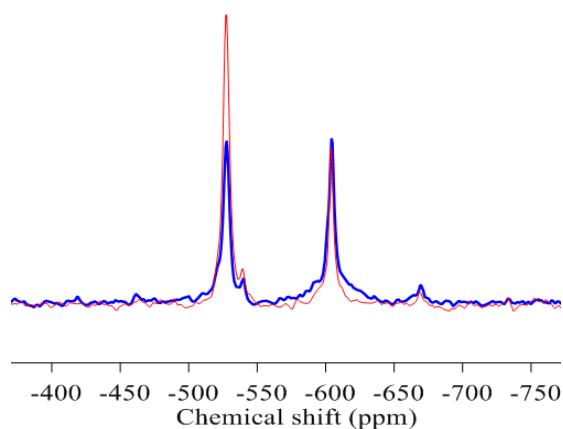


Figure 5.12  $^{119}\text{Sn}$  STA/MAS NMR spectra of LTY-I before (red) and after reaction (blue) with palmitic acid in a paint film.

### 5.2.6 Conclusions about Lead-Tin Yellow (Type I)

High-quality relativistic DFT calculations enable the assignment of the solid-state NMR spectra of crystallographically inequivalent heavy metal nuclides for  $\text{Pb}_2\text{SnO}_4$ . The calculated chemical-shift principal components for  $^{207}\text{Pb}$  deviate, at most, by 15% from the experimental ones. The combination of ssNMR and DFT molecular-cluster calculations is applicable to studies of other lead-containing materials, as well as solids containing other heavy nuclides.

In LTY-I, by ssNMR spectroscopy, only minium and  $\text{Pb}_2\text{SnO}_4$  are detectable as possible sources of lead ions for the formation of lead soaps. Other lead oxides, as proposed sources of lead reacting with the free fatty acids<sup>17b</sup>, are not detected in the unreacted pigment. Quantitative evaluation of NMR spectra of the unreacted paint versus the post-reaction material shows that  $\text{Pb}_2\text{SnO}_4$  is a source of lead in the formation of lead soaps from lead-tin yellow. Whether the  $\text{Pb}_2\text{SnO}_4$  participates directly in reaction with palmitic acid, or produces intermediates that react with the palmitic acid, cannot be determined by these experiments.

### **5.3 Investigating the Effect of Humidity on Soap Formation in Lead White and Zinc White Oil Paints**

Carbon-13 NMR spectroscopy provides a useful method for observing the reaction of palmitic acid with pigments because it is quantitative and, due to the slow reaction rate and use of  $^{13}\text{C}$  methyl-labeled palmitic acid to increase signal, the reaction can be tracked over several days. Many methods traditionally used to analyze paint materials, such as FTIR or Raman spectroscopies, suffer from the non-quantitative nature of the measurement. Although this limitation of these methods can be ameliorated by careful calibration, a separate calibration would be needed for each sample matrix used, making the process prohibitively complex. As long as the sites being used to track the progress of reaction have a similar cross-polarization efficiency (comparison between carboxylate groups, but not between carboxylate and methyl groups), NMR spectroscopy gives a quantitative measurement.

Using  $^{13}\text{C}$ -labeled palmitic acid, a high-quality spectrum can be obtained in 10 minutes. This experiment time permits collection of a spectrum every half hour, providing a large number of data points to fit a kinetic model accurately.

### 5.3.1 Experimental Details

#### 5.3.1.1 Synthesis and Preparation

Lead white oil paint was prepared by mixing linseed oil and basic lead white (22/78 wt%). The lead white paint was dried in an oven for 3 months, then left to age at ambient laboratory temperature and humidity for approximately 3 years. The paint was crushed with a mortar and pestle under liquid nitrogen and stored in a vial until use.

Zinc white oil paint was prepared by mixing linseed oil and zinc (II) oxide (20/80 wt%). The zinc white paint was dried at ambient laboratory temperature and humidity for 5 months. The paint was crushed with a mortar and pestle under liquid nitrogen and stored in a vial until use.

To prepare for each reaction sample, crushed  $^{13}\text{C}$  palmitic acid (~0.02 g) and crushed paint (~0.2 g) were weighed into separate vials, and then placed into various chambers subject to specific relative humidity. Relative humidity was controlled by a water-glycerol solution, except for 0%RH which used calcium sulfate as a desiccant. The samples were left in their respective humidity chambers for 24 hours to equilibrate before mixing and beginning measurements.

The paint and labeled acid were crushed together in a mortar and pestle and quickly packed into a NMR rotor to begin taking measurements. This procedure leaves about 20 minutes between removing the sample from the humidity chamber and sealing it and about 25 minutes total before the first spectrum is collected.

#### 5.3.1.2 Experimental NMR Methods

$^{13}\text{C}$  ssNMR spectra were recorded at 11.75 tesla (125.76 MHz  $^{13}\text{C}$  frequency) with a standard Bruker 4-mm probe. Glycine was used as a secondary external

reference at 176 ppm relative to TMS. Spectra were acquired using cross-polarization with MAS at 12 kHz, with 128 scans (10 minutes) every 30 minutes for 2-3 days. The peaks assigned to the carboxyl carbons were fit using a subprogram of the NMR-processing program, MestReNova<sup>106</sup>, developed by Mestre Research. Peak areas (example in Figure 5.13) were used to determine relative concentrations of palmitic acid and lead palmitate.

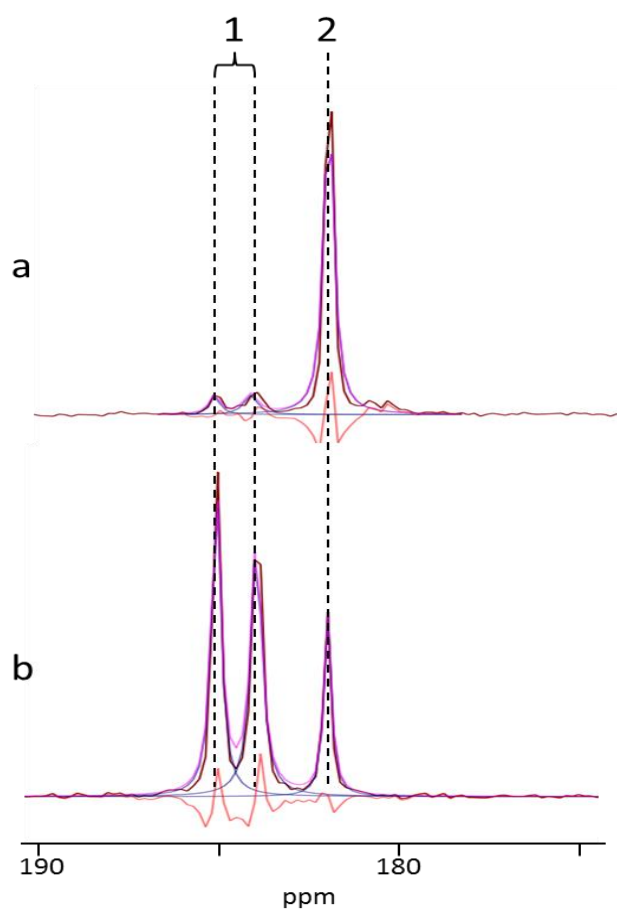


Figure 5.13 <sup>13</sup>C CPMAS spectra (red) of (1) lead palmitate and (2) palmitic acid (A) at the beginning and (B) after the reaction has progressed for one day, with fits (purple) and residuals (pink).

### 5.3.2 A Theoretical Model for Reactive Diffusion in One Dimension

The formation of lead palmitate in a paint film can be described by a diffusion controlled reaction scheme, as shown in Figure 5.14. This model consists of a mobile species (palmitic acid) initially sitting on a surface and diffusing linearly into a paint film, reacting immediately upon encountering the trapped species (lead ions).

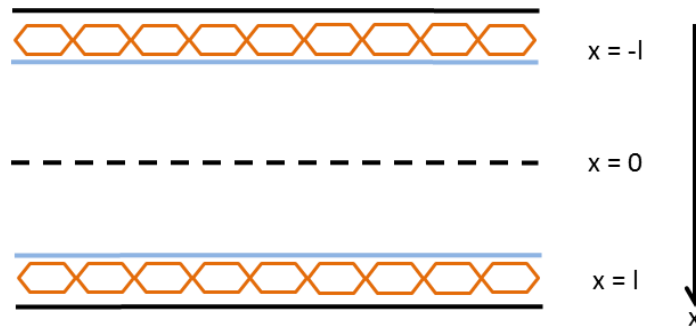


Figure 5.14 A schematic representation of the geometry assumed for the one-dimensional diffusion model. Where a mobile species (orange) sits on the surface of a paint particle or film (blue line) and must diffuse in to react.

Diffusion from two saturated surfaces can be described by:<sup>107</sup>

$$\frac{\partial C}{\partial t} = D \frac{\partial^2 C}{\partial x^2} - kC \quad (1)$$

$$C_1 = C_0(1 - \sum_{n=0}^{\infty} f_n(t)g_n(x)) \quad (2)$$

$$g_n(x) = \frac{4}{\pi} \frac{-1^n}{2n+1} \cos \frac{(2n+1)\pi x}{2l}$$

$$f_n(t) = e^{-a_n t} \quad ; \quad a_n = \frac{\pi^2 D (2n+1)^2}{4l^2} \quad (3)$$

where  $C_0$  is the concentration at time zero,  $D$  is the diffusion constant of palmitic acid,  $k$  is the reaction rate constant, and  $l$  is half the thickness of the film. Combining the

effects of diffusion with the first order reaction, one obtains an expression for the instantaneous concentration:

$$C(x, t) = k \int_0^t C_1 e^{-kt'} dt' + C_1 e^{-kt} \quad (4)$$

Integration gives:

$$C(x, t) = C_0 \left( 1 + \sum_{n=0}^{\infty} \left( 1 + \frac{1}{\frac{a_n}{k} + 1} \right) f_n(t) g_n(x) e^{-kt} - \sum_{n=0}^{\infty} \frac{1}{\frac{a_n}{k} + 1} g_n(x) \right) \quad (5)$$

as a final expression for the concentration of product as a function of time and distance from the surface.

The total reaction rate, total product produced per unit time, is defined as:

$$\begin{aligned} \frac{dn_p}{dt} &= \int_V kc dV = \int_{-l}^l kcA dx \quad (6) \\ &= kAC_0 \left( 2l + \sum_{n=0}^{\infty} \left( 1 + \frac{k}{a_n + k} \right) f_n(t) e^{-kt} \cdot \frac{16}{\pi^2} \frac{l}{(2n+1)^2} - \sum_{n=0}^{\infty} \frac{k}{a_n + k} \frac{16}{\pi^2} \frac{l}{(2n+1)^2} \right) \end{aligned}$$

where  $A$  is the cross section of the sample surface.

The final result for total product at time,  $t$ , is given by:

$$P(t) = \int_0^t \frac{dn_p(t')}{dt'} dt' = kAC_0 (d \cdot t + l \sum_{n=0}^{\infty} g_n (1 - e^{-(a_n+k)t})) \quad (7)$$

$$d = 2l - l \sum_{n=0}^{\infty} b_n \quad ; \quad b_n = \frac{16}{\pi^2} \frac{k}{a_n + k} \frac{1}{(2n+1)^2} \quad (8)$$

$$a_n = \frac{\pi^2 D (2n+1)^2}{4l^2} \quad (9)$$

$$g_n = \frac{b_n}{k} \left( 1 + \frac{k}{a_n + k} \right) \quad (10)$$

Using the approximation that  $n=0$ , produces this function, which can be used to fit the reaction profile:

$$P(t) = BA_1 t + BA_2 (1 - e^{-A_3 t}) \quad (11)$$

$$A_1 = 1 - \frac{8}{\pi^2} \frac{k}{a_0 + k} \quad (12)$$

$$A_2 = \frac{8}{\pi^2} \frac{1}{a_0+k} \left(1 + \frac{k}{a_0+k}\right) \quad (13)$$

$$A_3 = a_0 + k \quad (14)$$

$$B = kVC_0 \quad (15)$$

By defining

$$r = \frac{A_1}{A_2} \quad (16)$$

and the expressions for  $A_1$ ,  $A_2$ , and  $A_3$ , one obtains expressions for the rate constant and diffusion time constant:

$$k = \frac{A_3 \left( \frac{\pi^2}{8} A_3 - r \right)}{A_3 + r} \quad (17)$$

$$\frac{D}{l^2} = \frac{4a_0}{\pi^2} \quad (18)$$

From the parameters obtained by fitting the data to equation (11) and using equations (14, 16-18), the values for the first-order reaction parameter  $k$  and the quantity  $D/l^2$  can be calculated.

### 5.3.3 Results

The profiles of percent acid reacted versus time are shown in Figure 5.15. There is a clear difference in the rate of soap formation based on the humidity at which each experiment was conducted. At higher humidity, the reaction moves more quickly and reaches equilibrium at a higher percentage soap formation. There is a difference in the rate of soap formation between the zinc- and lead-based paints, but this difference most likely results from the difference in the age of the paints, exacerbated by lead acting as a drier causing greater crosslinking in the same time. The zinc soap was not aged as long, so it likely has a much lower degree of cross-

linking of the fatty-acid matrix and therefore has fewer obstacles to molecular diffusion.

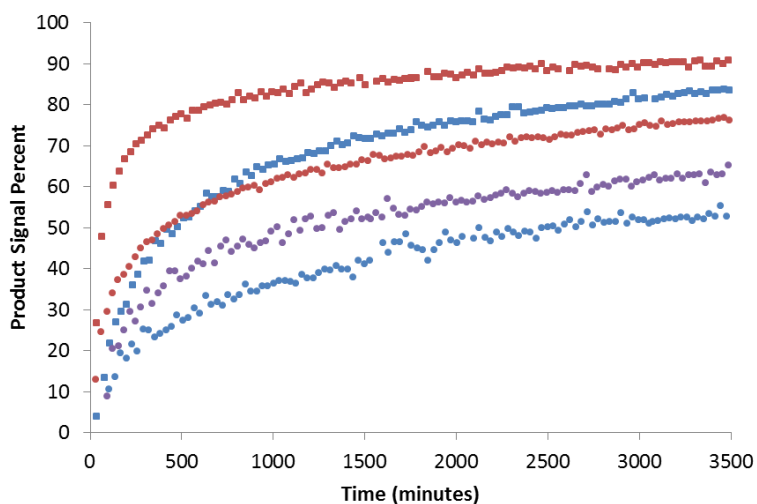


Figure 5.15 The formation of lead or zinc soaps in a sample containing lead white (circles) or zinc white (squares), when exposed to palmitic acid. Experiments were conducted at relative humidities of 90% (red), 60% (purple), and 0% (blue).

The thickness of the paint film was not controlled in these initial experiments, but the estimated size of the particles coated with a layer of palmitic acid is between 1.0 and 0.1 micron. A preliminary fit on the basic lead white sample subjected to a relative humidity of 60% is shown in Figure 5.16. This fit gives a rough estimate of the diffusion coefficient of palmitic acid in an aged, crosslinked basic lead white paint matrix, at a relative humidity of 60%, as  $3.8 \times 10^{-7}$  -  $3.8 \times 10^{-9}$  cm<sup>2</sup>/sec.

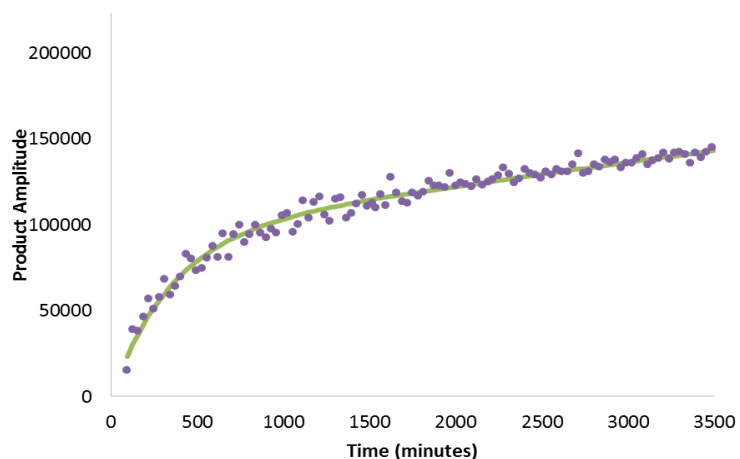


Figure 5.16 The formation of lead palmitate in a paint sample containing lead white, when exposed to palmitic acid at a relative humidity of 60%. The experimental points graphed by amplitude in arbitrary units (with the axis scaled as 100%). The green line is the theoretical dependence of amount of lead palmitate given in equation (11).

### 5.3.4 Conclusions about Soap Formation Kinetics in a Paint Film

These results are preliminary, and the value of the diffusion coefficient spans a range of two orders of magnitude. However, it is satisfying that the theoretical model fits the experimental data surprisingly well. The accuracy of the diffusion coefficient measurements can be significantly improved through more careful control of film thickness. Repeated experiments should be performed with paint films prepared more consistently between pigment types.

In future work, these measurements should be augmented by the determination of diffusion coefficients for water and organic solvents in such paint films by using pulsed-field-gradient NMR spectroscopy and unilateral NMR (NMR MOUSE®) techniques. Such measurements may also yield information on pore-size distribution and tortuosity which can be correlated with results from X-ray micro- and nanotomography.

## Chapter 6

### CONCLUSIONS AND FUTURE DIRECTIONS

Solid-state nuclear magnetic resonance (NMR) spectroscopy provides insight into the structure and dynamics of materials, making it an excellent technique for investigating the materials that compose these complex systems. Innovative modern experiments can successfully be used to overcome the inherent challenges presented by these materials. ssNMR spectroscopy's sensitivity to local structure makes it ideal for determining probable structures of materials that are hard to obtain as single crystals, as the chemical shift for lead materials is sensitive to small changes in the arrangement of bonding orbitals.

$^{13}\text{C}$ ,  $^{207}\text{Pb}$  NMR and FTIR spectra of lead soaps indicate two possible geometries for the coordination of the fatty acid chains to the lead ion. The local environment around the lead site in the long-chain carboxylates differs from the environment around the lead site in short-chain carboxylates. These experiments display the change in conformation occurring between lead octanoate and lead nonanoate. In the lower homologues (C8 and shorter), the broad line shapes appearing in the  $^{207}\text{Pb}$  NMR spectra indicate strong anisotropic magnetic-shielding interactions, whereas the NMR spectra of the higher homologues (C9 and longer) suggest a much less anisotropic electronic environment. The difference can be directly linked to single-crystal XRD results that show long-chain lead carboxylates display a holodirected arrangement and that short-chain lead carboxylates display a hemidirected arrangement of ligands.

$^{13}\text{C}$  NMR and FTIR spectra of some zinc soaps show that there may be a chain-length dependent effect in crystal formation or crystal packing, possibly similar to that of lead soaps. Zinc(II) has been found with several different coordination geometries, with some indication that the coordination number is dependent on the size of the ligand involved. A wider range of the zinc carboxylates should be studied with  $^{13}\text{C}$  NMR and FTIR spectroscopies to determine the nature of the chain-length dependence.

Modern ssNMR experiments such as DNP-enhanced  $^{207}\text{Pb}$  ssNMR allow the observation of signals that have been “hidden” in conventional techniques. It has been successfully applied here to study the pigment basic lead white, which had been challenging to measure due to its broad signals and fast relaxation times. The spectral fitting shows two lead sites in a 2:1 ratio, in agreement with crystallographic data, of lead carbonate and lead hydroxide signals. DNP enhancement of NMR spectroscopy was applied to measure an aged paint film, showing the formation of lead soaps. The soap could not be conclusively identified as lead palmitate due to low signal from the low concentration and some distortions, but it is attributed to a long-chain lead soap due to its relatively narrow signal and location.

High-quality relativistic DFT calculations enable the assignment of the solid-state NMR spectra of crystallographically inequivalent heavy metal nuclides for  $\text{Pb}_2\text{SnO}_4$ . The combination of ssNMR and DFT molecular-cluster calculations is applicable to studies of other lead-containing materials, as well as solids containing other heavy nuclides.

In LTY-I, minium and  $\text{Pb}_2\text{SnO}_4$  are detected as possible sources of lead ions for the formation of lead soaps. If other lead oxides act as a source of lead for the

reaction, as proposed by some authors, they are not detected in the unreacted pigment and could only serve as a small additional source. Quantitative evaluation of NMR spectra of a paint film, before and after reaction, show that  $\text{Pb}_2\text{SnO}_4$  is a source of lead in the formation of lead soaps from lead-tin yellow. Whether the  $\text{Pb}_2\text{SnO}_4$  participates directly in reaction, or produces intermediates that react with the palmitic acid, could not be determined here.

A diffusion-dominated, first-order reaction model provides a satisfying fit for the reaction profile of lead soap formation in a paint film with added palmitic acid. More accurate determination of the diffusion coefficient would result from careful control of film thickness and particle size used for reaction. Experiments should be performed with paint films prepared more consistently.

In the next phase of study, understanding soap formation in oil paints should be directed, primarily, towards diffusion measurements. These initial experiments, in some cases, provide information about which sample preparations are needed to understand the reaction better. Single-sided NMR and possibly pulse-field gradient NMR measurements could be used to determine diffusion constants that could be correlated with results from fitting reaction data. Differences in diffusion coefficients between paints prepared with different pigment types may be correlated with differences in the physical structure based on pigment particle size and void space. Such physical properties can be measured by synchrotron x-ray spectroscopic imaging and micro/nano-tomography. Understanding how molecules are transported through a paint film is important for fully understanding the heavy-metal soap formation process.

## REFERENCES

1. [www.nationalgallery.org.uk](http://www.nationalgallery.org.uk) (accessed 10 May 2017).
2. Bomford, D.; Leonard, M., *Issues in the Conservation of Paintings*. 1st ed.; Getty Conservation Institute: 2005.
3. Gettens, R.; Fitzhugh, E. W., *Azurite and Blue Verditer, Artists Pigments*. Oxford University Press: Oxford, 1993; Vol. 2.
4. Mattei, E.; Vivo, G. d.; Santis, A. D.; Gaetani, C.; Pelosi, C., *J. Raman Spec* **2008**, *39*, 302-306.
5. Banik, G., Discoloration of Green Copper Pigments in Manuscripts and Works of Graphic Art. *Restaurator. International Journal for the Preservation of Library and Archival Material* **2009**, *10* (2), 61.
6. Monico, L.; Janssens, K.; Cotte, M.; Sorace, L.; Vanmeert, F.; Brunetti, B. G.; Miliania, C., Chromium speciation methods and infrared spectroscopy for studying the chemical reactivity of lead chromate-based pigments in oil medium. *Microchemical Journal* **2016**, *124*, 272-282.
7. Mass, J. L.; Opila, R.; Buckley, B.; Cotte, M.; Church, J.; Mehta, A., The photodegradation of cadmium yellow paints in Henri Matisse's *Le Bonheur de vivre* (1905–1906). *Appl. Phys. A* **2013**, *111* (1), 59-68.
8. (a) Saunders, D.; Spring, M.; Higgitt, C., Colour change in red lead-containing paint films. *Proceedings of the XIIIth ICOM Triennial Meeting, Rio de Janeiro* **2002**, 455-463; (b) Aze, S.; Vallet, J.-M.; Baronnet, A.; Grauby, O., The fading of red lead pigment in wall paintings: tracking the physico-chemical transformations by means of complementary micro-analysis techniques. *Eur. J. Mineral* **2006**, *18*, 835-843.
9. Cooper, M. I.; Fowles, P. S.; Tang, C. C., Analysis of the laser-induced discoloration of lead white pigment. *Applied Surface Science* **2002**, *201*, 75-84.
10. Gettens, R. J.; Stout, G. L., *Painting Materials, A Short Encyclopaedia*. Dover Publications: New York, 1966.
11. Schoch, W.; Heller, I.; Schweingruber, F. H.; Kienast, F., Wood anatomy of central European Species: White Poplar, *Populus alba* L. **2004**.
12. Kuhn, H., *Conservation and Restoration of Works of Art and Antiquities*. Butterworths: London, 1986.
13. Museum of Fine Arts Boston. <http://cameo.mfa.org/wiki/Oak> (accessed 10 May 2017).
14. Fournier, R., *Illustrated Dictionary of Practical Pottery*. Chilton Book Company: Randor, PA, 1992.
15. Harley, R. D., *Artists' Pigments c. 1600-1835*. Butterworth Scientific: London, 1982.

16. Graaff, J. H.-d., *Natural Dyestuffs: Origin, Chemical Constitution, and Identification*. Central Research Laboratory for Objects of Art and Science: Amsterdam, 1969.
17. (a) Noble, P.; Boon, J. J.; Wadum, J., Dissolution, Aggregation and Protrusion. Lead Soap Formation in 17th Century Grounds and Paint Layers. *ArtMatters* **2003**, *1*, 46-61; (b) Keune, K. Binding Medium, Pigments and Metal Soaps Characterised and Localised in Paint Cross-Sections. PhD Thesis, University of Amsterdam, Amsterdam, 2005; (c) Spring, M.; Ricci, C.; Peggie, D.; Kazarian, S., ATR-FTIR Imaging for the Analysis of Organic Materials in Paint Cross Sections: Case Studies on Paint Samples from the National Gallery, London. *Analytical and Bioanalytical Chemistry* **2008**, *392* (1), 37-45; (d) Higgitt, C.; Spring, M.; Saunders, D., Pigment-medium Interactions in Oil Paint Films Containing Red Lead or Lead Tin Yellow. *National Gallery Techn. Bull.* **2003**, *24*, 75-91; (e) Centeno, S. A.; Mahon, D., The Chemistry of Aging in Oil Paintings: Metal Soaps and Visual Changes. *The Metropolitan Museum of Art Bulletin* **2009**, *67* (1), 12-19; (f) Hale, C.; Arslanoglu, J.; Centeno, S. A., Granacci in The Metropolitan Museum of Art: Aspects of Evolving Workshop Practice. In *Studying Old Master Paintings. Technology and Practice*, Spring, M., Ed. Archetype Publications and The National Gallery: London, 2011; pp 59-64.
18. Robinet, L.; Corbeil, M. C., The Characterization of Metal Soaps. *Stud. in Conserv.* **2003**, *48* (1), 23-40.
19. Cotte, M.; Dumas, P.; Richard, G.; Breniaux, R.; Walter, P., New Insight on Ancient Cosmetic Preparation by Synchrotron-based Infrared Microscopy. *Analytica Chimica Acta* **2005**, *553*, 105-110.
20. (a) Noble, P.; van Loon, A.; Boon, J. J. In *Chemical Changes in Old Master Paintings II: Darkening Due to Increased Transparency as a Result of Metal Soap Formation*, ICOM Committee for Conservation 14th Triennial Meeting, The Hague, 2005; James and James: The Hague, 2005; pp 496-503; (b) van Loon, A. Color Changes and Chemical Reactivity in Seventeenth-Century Oil Paintings. PhD Thesis, University of Amsterdam, Amsterdam, 2008; (c) Van der Weerd, J. Microspectroscopic Analysis of Traditional Oil Paint. PhD Thesis, University of Amsterdam, Amsterdam, 2002; (d) Cotte, M.; Checroun, E.; Susini, J.; Dumas, P.; Tchoreloff, P.; Besnard, M.; Walter, P., Kinetics of Oil Saponification by Lead Salts in Ancient Preparations of Pharmaceutical Lead Plasters and Painting Lead Mediums. *Talanta* **2006**, *70* (5), 1136-1142.
21. (a) Cotte, M.; Checroun, E.; Susini, J.; Walter, P., Micro-analytical Study of Interactions Between Oil and Lead Compounds in Paintings. *Appl. Phys. A-Mater* **2007**, *89*, 841-848; (b) Keune, K.; van Loon, A.; Boon, J. J., SEM Backscattered-Electron Images of Paint Cross Sections as Information Source for the Presence of the Lead White Pigment and Lead-Related Degradation and Migration Phenomena in Oil Paintings. *Microsc. Microanal.* **2011**, *17* (05), 696-701; (c) Catalano, J.; Murphy, A.; Yao, Y.; Alkan, F.; Zumbulyadis, N.; Centeno, S. A.; Dybowski, C., <sup>207</sup>Pb and <sup>119</sup>Sn Solid-State NMR and Relativistic DFT Studies of the Historic Pigment Lead-Tin

Yellow Type I and its Reactivity in Oil Paintings. *Journal of Physical Chemistry A* **2014**, *18*, 7952-7958.

22. (a) Suryanarayana, C.; Rao, K. C.; Kumar, D., Preparation and Characterization of Microcapsules Containing Linseed Oil and its Use in Self-healing Coatings. *Progress in Organic Coatings* **2008**, *63* (1), 72-78; (b) İşeri-Çağlar, D.; Baştürk, E.; Oktay, B.; Kahraman, M. V., Preparation and Evaluation of Linseed Oil Based Alkyd Paints. *Progress in Organic Coatings* **2014**, *77* (1), 81-86; (c) Chang, C.-W.; Lu, K.-T., Linseed-oil-based Waterborne UV/air Dual-cured Wood Coatings. *Progress in Organic Coatings* **2013**, *76* (7-8), 1024-1031.
23. (a) Mills, J. S.; White, R., *The Organic Chemistry of Museum Objects*. Butterworths: London, 1987; (b) van den Berg, J. D. J. Analytical Chemical Studies on Traditional Linseed Oil Paints. FOM-Institute for Atomic and Molecular Physics, Amsterdam, 2002.
24. (a) Porter, N.; Caldwell, S.; Mills, K., Mechanisms of Free Radical Oxidation of Unsaturated Lipids. *Lipids* **1995**, *30* (4), 277-290; (b) Muizebelt, W. J.; Nielen, M. W. F., Oxidative Crosslinking of Unsaturated Fatty Acids Studied with Mass Spectrometry. *Journal of Mass Spectrometry* **1996**, *31* (5), 545-554.
25. Tumosa, C. S.; Erhardt, D.; Mecklenburg, M. F.; Su, X. In *Linseed Oil Paint as Ionomer: Synthesis and Characterization*, Materials Issues in Art and Archaeology VII Materials Research Society: 2005; pp 25-31.
26. Jenkins, J. E.; Hibbs, M. R.; Alam, T. M., Identification of Multiple Diffusion Rates in Mixed Solvent Anion Exchange Membranes Using High Resolution MAS NMR. *ACS Macro Letters* **2012**, *1*, 910 - 914.
27. Hickner, M. A., Water-mediated Transport in Ion-containing Polymers. *Journal of Polymer Science Part B: Polymer Physics* **2012**, *50* (1), 9-20.
28. Fragiadakis, D.; Dou, S.; Colby, R. H.; Runt, J., Molecular Mobility, Ion Mobility, and Mobile Ion Concentration in Poly(ethylene oxide)-Based Polyurethane Ionomers. *Macromolecules* **2008**, *41* (15), 5723-5728.
29. Whitmore, P. M.; Colaluca, V. G.; Farrell, E., A Note on the Origin of Turbidity in Films of an Artists' Acrylic Paint Medium. *Studies in Conservation* **1996**, *41* (4), 250-255.
30. (a) Eibner, A., *Malmaterialienkunde als Grundlage der Maltechnik*. Verlag von Julius Springer: Berlin, 1909; (b) Noble, P.; van Loon, A.; Boon, J. J., Chemical Changes in Old Master Paintings II: Darkening due to Increased Transparency as a Result of Metal Soap Formation. In *ICOM Committee for Conservation 14th Triennial Meeting*, James and James: The Hague, 2005; Vol. 1, pp 496-503.
31. Boon, J. J.; van der Weerd, J.; Keune, K.; Noble, P.; Wadum, J., Mechanical and Chemical Changes in Old Master Paintings: Dissolution, Metal Soap Formation and Remineralisation Processes in Lead Pigmented Paint Layers of 17th Century Paintings. In *ICOM-CC 13th Triennial Meeting Rio de Janeiro, 2002*; Vol. 1, pp 410-406.
32. (a) Oudemans, T. F. M.; Erhardt, D., Organic residue analysis in ceramic studies: Implications for conservation treatment and collections management.

- Archaeological Conservation and its Consequence* **1996**, *IIC*, 137-142; (b) Spyros, A.; Anglos, D., Study of aging in oil paintings by 1D and 2D NMR spectroscopy. *Analytical Chemistry* **2004**, *17* (76), 4929-4936; (c) Spyros, A.; Anglos, D., Studies of organic paint binders by NMR spectroscopy. *Appl Phys A Mater Sci Process* **2006**, *4* (83), 705-708; (d) Sfakianaki, S.; Kouloumpi, E.; Anglos, D.; Spyros, A., Egg yolk identification and aging in mixed paint binding media by NMR spectroscopy. *Magn Reson Chem* **2015**, *1* (53), 22-26.
33. (a) Reger, D. L.; Collins, J. E.; Rheingold, A. L.; Liable-Sands, L. M.; Yap, G. P. A., Syntheses of Cationic Lead(II) and Tin(II) Complexes Containing Tris(pyrazolyl) methane Ligands . Control of Stereochemistry by Variation in Ligand Substitution. *Inorg. Chem.* **1997**, *36*, 345-351; (b) Reger, D. L.; Huff, M. F.; Rheingold, A. L.; Haggerty, B. S., Control of Structure in Lead(II) Complexes Using Poly (pyrazolyl) borate Ligands . Stereochemically Inactive Lone Pair in Octahedral [HB(3,5-Me<sub>2</sub>pz)<sub>3</sub>]<sub>2</sub>Pb (pz = Pyrazolyl Ring). *J. Am. Chem. Soc.* **1992**, *114*, 579-584; (c) Danieli, E.; Blümich, B., Single-sided Magnetic Resonance Profiling in Biological and Materials Science. *Journal of Magnetic Resonance* **2013**, *229*, 142-54; (d) Ulrich, K.; Centeno, S. A.; Arslanoglu, J.; Del Federico, E., Absorption and Diffusion Measurements of Water in Acrylic Paint Films by Single-sided NMR. *Progress in Organic Coatings* **2011**, *71* (3), 283-289.
34. Blümich, B.; Blumler, P.; Eidmann, G.; Guthausen, A.; Haken, R.; Schmitz, U.; Saito, K.; Zimmer, G., The NMR-mouse: Construction, excitation, and applications. *Magnetic resonance imaging* **1998**, *16* (5-6), 479-484.
35. (a) Blümich, B.; Casanova, F.; Perlo, J.; Anferova, S.; Anferov, V.; Kremer, K.; Goga, N.; Kupferschlager, K.; Adams, M., Advances of Unilateral Mobile NMR in Nondestructive Materials Testing. *Magnetic resonance imaging* **2005**, *23* (2), 197-201; (b) Blümich, B.; Perlo, J.; Casanova, F., Mobile Single-sided NMR. *Progress in Nuclear Magnetic Resonance Spectroscopy* **2008**, *52* (4), 197-269; (c) Casanova, F.; Perlo, J.; Blümich, B., Depth Profiling by Single-sided NMR. In *NMR Imaging in Chemical Engineering.*, Stapf, S.; Han, S., Eds. Wiley-VCH: Weinheim, 2006; pp 107-122.
36. Smith, B., *Infrared Spectral Interpretation: A Systematic Approach*. CRC Press: New York, 1999.
37. van der Waals, J. H., Gorter's footprints on the trail that led to magnetic resonance. In *Encyclopedia of Nuclear Magnetic Resonance*, Wiley: 1996; Vol. 1, p 667.
38. Rabi, I. I.; Zacharias, J. R.; Millman, S.; Kusch, P., A New Method of Measuring Nuclear Magnetic Moment. *Physical Review* **1938**, *4* (53), 318-327.
39. The Nobel Prize in Physics 1944.  
[http://www.nobelprize.org/nobel\\_prizes/physics/laureates/1944/](http://www.nobelprize.org/nobel_prizes/physics/laureates/1944/) (accessed 17 Apr 2017).
40. Purcell, E. M.; Torrey, H. C.; Pound, R. V., *Phys Review* **1946**, *69*, 37.
41. Bloch, F.; Hansen, W. W.; Packard, M., *Phys Review* **1946**, *69*, 127.

42. The Nobel Prize in Physics 1952.  
[http://www.nobelprize.org/nobel\\_prizes/physics/laureates/1952/](http://www.nobelprize.org/nobel_prizes/physics/laureates/1952/) (accessed 17 Apr 2017).
43. Rothwell, W. P.; Waugh, J. S., TRANSVERSE RELAXATION OF DIPOLAR COUPLED SPIN SYSTEMS UNDER RF-IRRADIATION - DETECTING MOTIONS IN SOLIDS. *Journal of Chemical Physics* **1981**, *74* (5), 2721-2732.
44. Hartmann, S. R.; Hahn, E. L., Nuclear Double Resonance in the Rotating Frame. *Physical Review* **1962**, *128*, 2042.
45. Parella, T. eNMR: NMR Periodic Table.
46. Neue, G.; Dybowski, C.; Smith, M. L.; Hepp, M. A.; Perry, D. L., Determination of Pb-207(2+) chemical shift tensors from precise powder lineshape analysis. *Solid State Nuclear Magnetic Resonance* **1996**, *6* (3), 241-250.
47. MacGregor, A. W.; O'Dell, L. A.; Schurko, R. W., New Methods for the Acquisition of Ultra-Wideline Solid-State NMR Spectra of Spin-1/2 Nuclides. *J. Magn. Reson* **2011**, *208* (1), 103-13.
48. Eichele, K. *HBA 3.1 and WSOLIDS*, University of Tübingen: Tübingen, 2013.
49. Schurko, R. W., Ultra-Wideline Solid-State NMR Spectroscopy. *Acc. Chem. Res.* **2013**, *9* (46), 1985-1995.
50. Larsen, F. H.; Jakobsen, H. J.; Ellis, P. D.; Nielsen, N. C., Sensitivity-enhanced quadrupolar-echo NMR of half-integer quadrupolar nuclei. Magnitudes and relative orientation of chemical shielding and quadrupolar coupling tensors. *Journal of Physical Chemistry* **1997**, *101*, 8597-8606.
51. Kupce, E.; Freeman, R., ADIABATIC PULSES FOR WIDE-BAND INVERSION AND BROAD-BAND DECOUPLING. *Journal of Magnetic Resonance Series A* **1995**, *115* (2), 273-276.
52. Harris, K. J.; Lupulescu, A.; Lucier, B. E. G.; Frydman, L.; Schurko, R. W., Broadband adiabatic inversion pulses for cross polarization in wideline solid-state NMR spectroscopy. *Journal of Magnetic Resonance* **2012**, *224*, 38-47.
53. Aussenac, F.; Sergeev, I.; Pawsey, S. Introduction to Solid State DNP NMR: A Free Nuclear Magnetic Resonance Educational Webinar.  
<https://www.bruker.com/service/education-training/webinars/nmr-webinars/introduction-to-solid-state-dnp-nmr.html>.
54. Kobayashi, T.; Perras, F. A.; Goh, T. W.; Metz, T. L.; Huang, W.; Pruski, M., DNP-Enhanced Ultrawideline Solid-State NMR Spectroscopy: Studies of Platinum in Metal-Organic Frameworks. *Journal of Physical Chemistry Letters* **2016**, *7* (13), 2322-2327.
55. Hirsh, D. A.; Rossini, A. J.; Emsley, L.; Schurko, R. W., <sup>35</sup>Cl dynamic nuclear polarization solid-state NMR of active pharmaceutical ingredients. *Phys. Chem. Chem. Phys.* **2016**.
56. Kennedy, J. D.; McFarlane, W., Multinuclear NMR. Mason, J., Ed. Plenum Press: New York 1987; pp 305-333.
57. (a) Catalano, J.; Yao, Y.; Murphy, A.; Zumbulyadis, N.; Centeno, S. A.; Dybowski, C., NMR Spectra and <sup>207</sup>Pb Chemical-Shift Tensors of Lead Carboxylates

- Relevant to Soap Formation in Oil Paintings. *Appl. Spectrosc.* **2014**, *68* (3), 280-286;
- (b) Katz, M. J.; Aguiar, P. M.; Batchelor, R. J.; Bokov, A. A.; Ye, Z. G.; Kroeker, S.; Leznoff, D. B., Structure and Multinuclear Solid-state NMR of a Highly Birefringent Lead-gold Cyanide Coordination Polymer. *J. Am. Chem. Soc.* **2006**, *128* (11), 3669-76.
58. Lacouture, F.; Francois, M.; Didierjean, C.; Rivera, J.-P.; Rocca, E.; Steinmetz, J., Anhydrous lead(II) heptanoate. *Acta Crystallographica Section C* **2001**, *C57*, 530-531.
59. Feio, G.; Burrows, H. D.; Geraldés, C. F. G. C.; Pinheiro, T. J. T., Multinuclear NMR studies of Lead (II) Soaps. <sup>13</sup>C and <sup>1</sup>H Studies of Solid and Liquid-Crystalline Phases. *Liq. Cryst.* **1991**, *9* (3), 417-432.
60. MacGregor, A. W.; O'Dell, L. A.; Schurko, R. W., New Methods for the Acquisition of Ultra-Wideline Solid-State NMR Spectra of Spin-1/2 Nuclides. *Journal of Magnetic Resonance* **2011**, *1* (208), 103-113.
61. Briand, G. G.; Smith, A. D.; Schatte, G.; Rossini, A. J.; Schurko, R. W., Probing Lead(II) Bonding Environments in 4-substituted Pyridine Adducts of (2,6-Me<sub>2</sub>C<sub>6</sub>H<sub>3</sub>S)<sub>2</sub>Pb: an X-ray Structural and Solid-state <sup>207</sup>Pb NMR Study. *Inorg. Chem.* **2007**, *46* (21), 8625-37.
62. Lomer, T. R.; Perera, K., Anhydrous Copper(II) Decanoate. *Acta Crystallogr. B* **1974**, *30*, 2912-2913.
63. Ellis, H. A.; White, N. A. S.; Taylor, R. A.; Maragh, P. T., Infrared, X-ray and Microscopic Studies on the Room Temperature Structure of Anhydrous Lead(II) n-Alkanoates. *J. Mol. Struct.* **2005**, *738* (1-3), 205-210.
64. Adeosun, S. O.; Sime, S., Properties of Molten Carboxylates. *Thermochim. Acta* **1976**, *17*, 351.
65. Arenas, A. S.; Garcia, M. V.; Redondo, M. I.; Cheda, J. A. R.; Roux, M. V.; Turrion, C., Thermophysical Study of Lead(II) N-Alkanoates by DSC, Optical Microscopy, FTIR and Raman-spectroscopy. *Liq. Cryst.* **1995**, *18* (3), 431-441.
66. Mesubi, M. A., An Infrared Study of Zinc, Cadmium, and Lead Salts of Some Fatty-acids. *J. Mol. Struct.* **1982**, *81* (1-2), 61-71.
67. Harrison, P. G.; Steel, A. T., Lead(II) carboxylate structures. *J. Organomet. Chem.* **1982**, *239* (1), 105-113.
68. Rajaram, R. K.; Rao, J. K. M., Crystal Structure of lead acetate trihydrate. *Crystalline Materials* **1982**, *160* (1-4), 225-234.
69. Martinez-Casado, F. J.; Ramos-Riesco, M.; Rodriguez-Cheda, J. A.; Cucinotta, F.; Fernandez-Martinez, A.; Garrido, L.; Matesanz, E.; Marchese, L., Short lead(II) soaps: from weakly fluorescent crystals to strongly phosphorescent and structurally varied vitreous phases. A thermal, structural and spectroscopic study. *Journal of Materials Chemistry C* **2014**, *2*, 9489-9496.
70. Casado, F. J. M.; Riesco, M. R.; da Silva, I.; Yelamos, M. I.; Labrador, A.; Cheda, J. A. R., Lithium and Lead(II) Butyrate Binary System. Pure Compounds and an Intermediate Salt: For 2D to 3D Coordination Polymers. *Cryst. Growth Des.* **2011**, *11* (3), 759-767.

71. Lacouture, F.; François, M.; Didierjean, C.; Rivera, J.-P.; Rocca, E.; Steinmetz, J., Anhydrous lead(II) Heptanoate. *Acta Crystallogr. C* **2001**, *57*, 530-531.
72. Catalano, J.; Murphy, A.; Yao, Y.; Yap, G. P. A.; Zumbulyadis, N.; Centeno, S.; Dybowski, C., Coordination Geometry of Lead Carboxylates - Spectroscopic and Crystallographic Evidence. *J. Chem. Soc. Dalton Trans.* **2015**, *44*, 2340-2347.
73. Shimoni-Livny, L.; Glusker, J. P.; Bock, C. W., Lone Pair Functionality in Divalent Lead Compounds. *Inorg. Chem.* **1998**, *37* (8), 1853-1867.
74. Murphy, A.; Yao, Y.; Yap, G. P. A.; Zumbulyadis, N.; Centeno, S. A.; Dybowski, C., Hemidirection in lead octanoate. *Acta Crystallogr.* **2017**, Submitted.
75. Osmond, G., Zinc white: a review of zinc oxide pigment properties and implications for stability in oil-based paintings. *AICCM Bulletin* **2012**, *1* (33), 20-29.
76. (a) Carlyle, L., *The artist's assistant: oil painting instruction manuals and handbooks in Britain 1800-1900 with reference to selected eighteenth-century sources*. Archetype Publications: London, 2001; (b) O'Hanlon, G. Zinc white: problems in oil paint. [www.naturalpigments.com/education/article.asp?ArticleID=127](http://www.naturalpigments.com/education/article.asp?ArticleID=127) (accessed 24 Oct 2007).
77. (a) Boitelle, R.; van den Berg, K., A technical examination of Odilon Redon's paintings from the Bongor Collection, Van Gogh Museum. *ArtMatters: Netherlands technical studies in art* **2005**, *3*, 66-81; (b) Osmond, G.; Keune, K.; Boon, J., A study of zinc soap aggregates in a late 19th century painting by RG Rivers at the Queensland Art Gallery. *AICCM Bulletin* **2005**, *29*, 37-46; (c) O'Donoghue, E.; Johnson, A.; Mazurek, J.; Preusser, F.; Schilling, M.; Walton, M., Dictated by media: conservation and technical analysis of a 1938 Joan Miro canvas painting. *The object in context: Crossing Conservation Boundaries: Contributions to the Munich Congress* **2006**, *28*; (d) Shimadzu, Y.; van den Berg, K. In *On metal soap related colour and transparency changes in a 19th century painting by Millais*, Netherlands Organisation for Scientific Research (NWO) The Hague, Boon, J.; Ferreira, E., Eds. The Hague, 2006; pp 43-52; (e) Zümbuhl, S. a. F., O In *The formation of protrusions in the later works of Alexej von Jawlensky*, Munich, Munich, 2006; p 309.
78. Jabłońska-Wawrzycka; A. Rogala, P.; Czerwonka, G.; Hodoroxicz, M.; Stadnicka, K., Zinc(II) complexes with heterocyclic ether, acid and amide. Crystal structure, spectral, thermal and antibacterial activity studies. *J. Mol. Struct.* **2016**, *1105*, 357-369
79. Kremer-Aach, A.; Klaui, W.; Bell, R.; Strerath, A.; Wunderlich, H.; Mootz, D., Cobalt as a Probe for Zinc in Metalloenzyme Model Compounds? A Comparison of Spectroscopic Features and Coordination Geometry of Four- and Five-Coordinate complexes. Crystal and Molecular Structures of [Co( $\eta^3$ -TpPh)( $\eta^2$ -TpPh)], [( $\eta^3$ -TpPh)Zn(anthranilate)], and [( $\eta^3$ -TpPh)M( $\eta^2$ -acac)] (TpPh = Hydrotris(3-phenylpyrazol-1-yl)borate, acac = Pentane-2,4-dionate, and M = Zn, Co). *Inorg. Chem.* **1997**, *36* (1552-1563).
80. Caley, E. R.; Richards, J. C., *Theophrastus on Stones*. The Ohio State University Press: Columbus, 2016.

81. Martinetto, P.; Anne, M.; Dooryhee, E.; Walter, P.; Tsoucaris, G., Synthetic hydrocerussite,  $2\text{PbCO}_3 \cdot \text{Pb}(\text{OH})_2$ , by X-ray powder diffraction. *Acta Crystallographica Section C-Crystal Structure Communications* **2002**, *58*, I82-I84.
82. Verhoeven, M. A.; Carlyle, L.; Reedijk, J.; Haasnoot, J. G., In *Reporting Highlights of the De Mayerne Programme*, Boon, J. J.; Frereira, E. S. B., Eds. NWO: 2006; pp 33-42.
83. (a) Becerra, L. R.; Gerfen, G. J.; Bellew, B. F.; Bryant, J. A.; Hall, D. A.; Inati, S. J.; Weber, R. T.; Un, S.; Prisner, T. F.; McDermott, A. E.; Fishbein, K. W.; Kreisler, K. E.; Temkin, R. J.; Singel, D. J.; Griffin, R. G., A SPECTROMETER FOR DYNAMIC NUCLEAR-POLARIZATION AND ELECTRON-PARAMAGNETIC-RESONANCE AT HIGH-FREQUENCIES. *Journal of Magnetic Resonance Series A* **1995**, *117* (1), 28-40; (b) Joye, C. D.; Griffin, R. G.; Hornstein, M. K.; Hu, K. N.; Kreisler, K. E.; Rosay, M.; Shapiro, M. A.; Sirigiri, J. R.; Temkin, R. J.; Woskov, P. P., Operational characteristics of a 14-W 140-GHz gyrotron for dynamic nuclear polarization. *Ieee Transactions on Plasma Science* **2006**, *34* (3), 518-523; (c) Barnes, A. B.; Mak-Jurkauskas, M. L.; Matsuki, Y.; Bajaj, V. S.; van der Wel, P. C. A.; DeRocher, R.; Bryant, J.; Sirigiri, J. R.; Temkin, R. J.; Lugtenburg, J.; Herzfeld, J.; Griffin, R. G., Cryogenic sample exchange NMR probe for magic angle spinning dynamic nuclear polarization. *Journal of Magnetic Resonance* **2009**, *198* (2), 261-270; (d) Rosay, M.; Lansing, J. C.; Haddad, K. C.; Bachovchin, W. W.; Herzfeld, J.; Temkin, R. J.; Griffin, R. G., High-frequency dynamic nuclear polarization in MAS spectra of membrane and soluble proteins. *Journal of the American Chemical Society* **2003**, *125* (45), 13626-13627.
84. (a) Zagdoun, A.; Casano, G.; Ouari, O.; Schwarzwald, M.; Rossini, A. J.; Aussenac, F.; Yulikov, M.; Jeschke, G.; Coperet, C.; Lesage, A.; Tordo, P.; Emsley, L., Large Molecular Weight Nitroxide Biradicals Providing Efficient Dynamic Nuclear Polarization at Temperatures up to 200 K. *Journal of the American Chemical Society* **2013**, *135* (34), 12790-12797; (b) Sauvee, C.; Rosay, M.; Casano, G.; Aussenac, F.; Weber, R. T.; Ouari, O.; Tordo, P., Highly Efficient, Water-Soluble Polarizing Agents for Dynamic Nuclear Polarization at High Frequency. *Angewandte Chemie-International Edition* **2013**, *52* (41), 10858-10861; (c) Song, C. S.; Hu, K. N.; Joo, C. G.; Swager, T. M.; Griffin, R. G., TOTAPOL: A biradical polarizing agent for dynamic nuclear polarization experiments in aqueous media. *Journal of the American Chemical Society* **2006**, *128* (35), 11385-11390; (d) Hu, K. N.; Yu, H. H.; Swager, T. M.; Griffin, R. G., Dynamic nuclear polarization with biradicals. *Journal of the American Chemical Society* **2004**, *126* (35), 10844-10845.
85. (a) Maly, T.; Debelouchina, G. T.; Bajaj, V. S.; Hu, K.-N.; Joo, C.-G.; Mak-Jurkauskas, M. L.; Sirigiri, J. R.; van der Wel, P. C. A.; Herzfeld, J.; Temkin, R. J.; Griffin, R. G., Dynamic nuclear polarization at high magnetic fields. *Journal of Chemical Physics* **2008**, *128* (5), 052211; (b) Thurber, K. R.; Tycko, R., Theory for cross effect dynamic nuclear polarization under magic-angle spinning in solid state nuclear magnetic resonance: The importance of level crossings. *Journal of Chemical Physics* **2012**, *137* (8).

86. (a) Michaelis, V. K.; Markhasin, E.; Daviso, E.; Herzfeld, J.; Griffin, R. G., Dynamic Nuclear Polarization of Oxygen-17. *Journal of Physical Chemistry Letters* **2012**, *3* (15), 2030-2034; (b) Ouari, O.; Trang, P.; Ziarelli, F.; Casano, G.; Aussenac, F.; Thureau, P.; Gigmes, D.; Tordo, P.; Viel, S., Improved Structural Elucidation of Synthetic Polymers by Dynamic Nuclear Polarization Solid-State NMR Spectroscopy. *Acs Macro Letters* **2013**, *2* (8), 715-719; (c) Rossini, A. J.; Zaghdoun, A.; Lelli, M.; Lesage, A.; Coperet, C.; Emsley, L., Dynamic Nuclear Polarization Surface Enhanced NMR Spectroscopy. *Accounts of Chemical Research* **2013**, *46* (9), 1942-1951; (d) Perras, F. A.; Kobayashi, T.; Pruski, M., Natural Abundance O-17 DNP Two-Dimensional and Surface-Enhanced NMR Spectroscopy. *Journal of the American Chemical Society* **2015**, *137* (26), 8336-8339; (e) Kobayashi, T.; Perras, F. A.; Slowing, I. I.; Sadow, A. D.; Pruski, M., Dynamic Nuclear Polarization Solid-State NMR in Heterogeneous Catalysis Research. *Acs Catalysis* **2015**, *5* (12), 7055-7062; (f) Mouat, A. R.; George, C.; Kobayashi, T.; Pruski, M.; van Duyne, R. P.; Marks, T. J.; Stair, P. C., Highly Dispersed SiO<sub>x</sub>/Al<sub>2</sub>O<sub>3</sub> Catalysts Illuminate the Reactivity of Isolated Silanol Sites. *Angewandte Chemie-International Edition* **2015**, *54* (45), 13346-13351.
87. Kobayashi, T.; Perras, F. A.; Murphy, A.; Yao, Y.; Catalano, J.; Centeno, S. A.; Dybowski, C.; Zumbulyadis, N.; Pruski, M., DNP-Enhanced Ultrawideline 207Pb Solid-State NMR Spectroscopy: An Application to Cultural Heritage Science. *J. Chem. Soc., Dalton Trans.* **2017**, *46*, 3535-3540.
88. Harris, R. K.; Becker, E. D.; De Menezes, S. M. C.; Granger, P.; Hoffman, R. E.; Zilm, K. W., Further conventions for NMR shielding and chemical shifts IUPAC recommendations 2008 (Reprinted from Pure Appl Chem, vol 80, pg 59, 2008). *Solid State Nuclear Magnetic Resonance* **2008**, *33* (3), 41-56.
89. Massiot, D.; Farnan, I.; Gautier, N.; Trumeau, D.; Trokiner, A.; Coutures, J. P., GA-71 AND GA-69 NUCLEAR-MAGNETIC-RESONANCE STUDY OF BETA-GA<sub>2</sub>O<sub>3</sub> - RESOLUTION OF 4-FOLD AND 6-FOLD COORDINATED GA SITES IN STATIC CONDITIONS. *Solid State Nuclear Magnetic Resonance* **1995**, *4* (4), 241-248.
90. (a) van der Wel, P. C. A.; Hu, K.-N.; Lewandowski, J.; Griffin, R. G., Dynamic nuclear polarization of amyloidogenic peptide nanocrystals: GNNQQNY, a core segment of the yeast prion protein Sup35p. *Journal of the American Chemical Society* **2006**, *128* (33), 10840-10846; (b) Lafon, O.; Thankamony, A. S. L.; Kobayashi, T.; Carnevale, D.; Vitzthum, V.; Slowing, I. I.; Kandel, K.; Vezin, H.; Amoureux, J.-P.; Bodenhausen, G.; Pruski, M., Mesoporous Silica Nanoparticles Loaded with Surfactant: Low Temperature Magic Angle Spinning C-13 and Si-29 NMR Enhanced by Dynamic Nuclear Polarization. *Journal of Physical Chemistry C* **2013**, *117* (3), 1375-1382; (c) Rossini, A. J.; Widdifield, C. M.; Zaghdoun, A.; Lelli, M.; Schwarzwald, M.; Coperet, C.; Lesage, A.; Emsley, L., Dynamic Nuclear Polarization Enhanced NMR Spectroscopy for Pharmaceutical Formulations. *Journal of the American Chemical Society* **2014**, *136* (6), 2324-2334.

91. Catalano, J.; Murphy, A.; Yao, Y.; Yap, G. P. A.; Zumbulyadis, N.; Centeno, S. A.; Dybowski, C., Coordination geometry of lead carboxylates - spectroscopic and crystallographic evidence. *Dalton Transactions* **2015**, 44 (5), 2340-2347.
92. (a) Eastaugh, N., Walsh V., Chaplin, T., Siddall, R. , *Pigment Compendium. A Dictionary of Historical Pigments*. Elsevier Butterworth-Heinemann: Amsterdam, 2004; (b) Martin, E.; Duval, A. R., Les Deux Varietes de Jaune de Plomb et d'etaïn: Etude Chronologique. *Stud. Conserv.* **1990**, 35 (3), 117-136.
93. Boon, J. J.; Gore, E.; Keune, K.; Burnstock, A., Image Analytical Studies of Lead Soap Aggregates and thier Relationship to Lead and Tin in 15th Century Lead Tin Yellow Paints from the S Herbourne Triptych. In *Infrared and Raman User Group (IRUG) meeting*, Picollo, M., Ed. Florence, Italy, 2004; pp 66-74.
94. Wanklyn, B. M.; Wondre, F. R.; Davison, W., Flux Growth of Crystals of Some Complex Oxides. *J. Mater. Sci. Lett.* **1984**, 3 (6), 539-543.
95. (a) Pelosi, C.; Agresti, G.; Santamaria, U.; Mattei, E., Artificial Yellow Pigments: Production and Characterization Through Spectroscopic Methods of Analysis. *e-Preservation Science* **2010**, 7, 108-115; (b) Tite, M.; Pradell, T.; Shortland, A., Discovery, Production and Use of Tin-based Opacifiers in Glasses, Enamels and Glazes from the Late Iron Age Onwards: A Reassessment. *Archaeometry* **2008**, 50 (1), 67-84; (c) Clark, R. J. H.; Cridland, L.; Kariuki, B. M.; Harris, K. D. M.; Withnall, R., Synthesis, Structural Characterisation and Raman Spectroscopy of the Inorganic Pigments Lead Tin Yellow Types I and II and Lead Antimonate Yellow: their Identification on Medieval Paintings and Manuscripts. *J. Chem. Soc. Dalton* **1995**, (16), 2577-2582; (d) Hashemi, T.; Brinkman, A. W.; Wilson, M. J., Preparation, Sintering and Electrical Behavior of Di-lead Stannate. *J. Mater. Sci. Lett.* **1992**, 11 (10), 666-668.
96. Gavarrı, J. R.; Vigouroux, J. P.; Calvarin, G.; Hewat, A. W., Structure of  $\text{SnPb}_2\text{O}_4$  at 4 Temperatures - the Relation between Thermal-Expansion and Thermal Agitation. *J Solid State Chem* **1981**, 36 (1), 81-90.
97. Gabuda, S. P.; Kozlova, S. G.; Terskikh, V. V.; Dybowski, C.; Neue, G.; Perry, D. L., Pb-207 NMR of Minium,  $\text{Pb}_3\text{O}_4$ : Evidence for the Pb-2 (4+) Ion and Possible Relativistic Effects in the Pb-Pb Bond. *Solid State Nucl. Magn. Reson.* **1999**, 15 (2), 103-107.
98. Eichele, K. *HBA 3.1 and WSOLIDS*; University of Tübingen: Tübingen, 2013.
99. (a) ADF2013, *SCM, Theoretical Chemistry, Vrije Universiteit, Amsterdam, The Netherlands*, <http://www.scm.com>; (b) Guerra, C. F.; Snijders, J. G.; te Velde, G.; Baerends, E. J., Towards an Order-N DFT Method. *Theor. Chem. Acc.* **1998**, 99 (6), 391-403; (c) te Velde, G.; Bickelhaupt, F. M.; Baerends, E. J.; Guerra, C. F.; Van Gisbergen, S. J. A.; Snijders, J. G.; Ziegler, T., Chemistry with ADF. *J. Comput. Chem.* **2001**, 22 (9), 931-967.
100. (a) Perdew, J. P., Density-Functional Approximation for the Correlation-Energy of the Inhomogeneous Electron-Gas. *Phys. Rev. B* **1986**, 33 (12), 8822-8824; (b) Becke, A. D., Density-Functional Exchange-Energy Approximation with Correct Asymptotic-Behavior. *Phys. Rev. A* **1988**, 38 (6), 3098-3100.

101. (a) van Lenthe, E.; Baerends, E. J.; Snijders, J. G., Relativistic Regular 2-Component Hamiltonians. *J. Chem. Phys.* **1993**, *99* (6), 4597-4610; (b) van Lenthe, E.; van Leeuwen, R.; Baerends, E. J.; Snijders, J. G., Relativistic Regular Two-component Hamiltonians. *Int. J. Quantum Chem.* **1996**, *57* (3), 281-293; (c) Lenthe, E. v.; Snijders, J. G.; Baerends, E. J., The Zero-order Regular Approximation for Relativistic Effects: The Effect of Spin-Orbit Coupling in Closed Shell Molecules. AIP: 1996; Vol. 105, pp 6505-6516; (d) Wolff, S. K.; Ziegler, T.; van Lenthe, E.; Baerends, E. J., Density Functional Calculations of Nuclear Magnetic Shieldings Using the Zeroth-order Regular Approximation (ZORA) for Relativistic Effects: ZORA Nuclear Magnetic Resonance. *J. Chem. Phys.* **1999**, *110* (16), 7689-7698.
102. (a) Ditchfield, R., Self-Consistent Perturbation-Theory of Diamagnetism .1. Gauge-Invariant Lcao Method for NMR Chemical-Shifts. *Mol. Phys.* **1974**, *27* (4), 789-807; (b) Schreckenbach, G.; Ziegler, T., Calculation of NMR Shielding Tensors Using Gauge-Including Atomic Orbitals and Modern Density-Functional Theory. *J. Phys. Chem.* **1995**, *99* (2), 606-611; (c) Schreckenbach, G.; Ziegler, T., The Calculation of NMR Shielding Tensors Based on Density Functional Theory and the Frozen-core Approximation. *Int. J. Quantum Chem.* **1996**, *60* (3), 753-766.
103. Fayon, F.; Farnan, I.; Bessada, C.; Coutures, J.; Massiot, D.; Coutures, J. P., Empirical Correlations Between Pb-207 NMR Chemical Shifts and Structure in Solids. *J. Amer. Chem. Soc.* **1997**, *119* (29), 6837-6843.
104. Alkan, F.; Dybowski, C., Calculation of Chemical-Shift Tensors of Heavy Nuclei: A DFT/ZORA Investigation of 199Hg Chemical-Shift Tensors in Solids, and the Effects of Cluster Size and Electronic-State Approximations. *Phys. Chem. Chem. Phys.* **2014**, *16* (27), 14298-14308.
105. (a) Sebal, A.; Merwin, L. H.; Dollase, W. A.; Seifert, F., A Multinuclear, High-resolution Solid-state NMR-study of Sorensenite (Na<sub>4</sub>SnBe<sub>2</sub>(Si<sub>3</sub>O<sub>9</sub>.2H<sub>2</sub>O) and Comparison with Wollastonite and Pectolite. *Phys. Chem. Miner.* **1990**, *17* (1), 9-16; (b) Clayden, N. J.; Dobson, C. M.; Fern, A., High-Resolution Solid-State Sn-119 Nuclear Magnetic-Resonance Spectroscopy of Ternary Tin Oxides. *J. Chem. Soc. Dalton* **1989**, (5), 843-847; (c) Cossement, C.; Darville, J.; Gilles, J. M.; Nagy, J. B.; Fernandez, C.; Amoureux, J. P., Chemical-shift Anisotropy and Indirect Coupling in SnO<sub>2</sub> and SnO. *Magn. Reson. Chem.* **1992**, *30* (3), 263-270; (d) Kulshreshtha, S. K.; Sasikala, R.; Sudarsan, V., Non-random Distribution of Cations in Sn<sub>1-x</sub>Ti<sub>x</sub>O<sub>2</sub> (0.0 ≤ x ≤ 1.0): a Sn-119 MAS NMR Study. *J. Mater. Chem.* **2001**, *11* (3), 930-935.
106. *MestReNova*, Mestre Research: Santiago de Compostela, Spain.
107. (a) Danckwerts, P. V., Absorption by Simultaneous Diffusion and Chemical Reaction into Particles of Various Shapes and into Falling Drops. *Trans Faraday Society* **47**, 1014-1023; (b) Carslaw, H. S.; Jaeger, J. C., *Conduction of Heat in Solids*. 2nd ed.; Clarendon Press: Oxford, 1959; (c) Crank, J., *The Mathematics of Diffusion*. 2nd ed.; Clarendon Press: Oxford, 1975.

## Appendix A

### PERMISSIONS AND COPYRIGHT

This dissertation incorporates portions of my previously published work.

Chapter 3 contains material from “Coordination geometry of lead carboxylates – spectroscopic and crystallographic evidence” adapted with permission from *Dalton Transaction*, **2015**, *44*, 2340. DOI: 10.1039/C4DT03075C, as well as material from “Hemidirection in lead octanoate” reprinted with permission from *Journal of Chemical Crystallography* **2017** (submitted).

Chapter 5 contains material from “DNP-enhanced ultrawideline  $^{207}\text{Pb}$  solid-state NMR spectroscopy: an application to cultural heritage science” *Dalton Trans.*, **2017**, *46*, 3535. DOI: 10.1039/C7DT00182G with permission from The Royal Society of Chemistry and material reprinted with permission from “ $^{207}\text{Pb}$  and  $^{119}\text{Sn}$  Solid-State NMR and Relativistic Density Functional Theory Studies of the Historic Pigment Lead–Tin Yellow Type I and Its Reactivity in Oil Paintings” *J. Phys. Chem. A*, **2014**, *118* (36), pp 7952–7958. DOI: 10.1021/jp505908j Copyright (2014) American Chemical Society.



**Title:** 207Pb and 119Sn Solid-State NMR and Relativistic Density Functional Theory Studies of the Historic Pigment Lead-Tin Yellow Type I and Its Reactivity in Oil Paintings

**Author:** Jaclyn Catalano, Anna Murphy, Yao Yao, et al

**Publication:** The Journal of Physical Chemistry A

**Publisher:** American Chemical Society

**Date:** Sep 1, 2014

Copyright © 2014, American Chemical Society

[LOGIN](#)

If you're a [copyright.com](#) user, you can login to RightsLink using your [copyright.com](#) credentials. Already a [RightsLink user](#) or want to [learn more?](#)

#### PERMISSION/LICENSE IS GRANTED FOR YOUR ORDER AT NO CHARGE

This type of permission/license, instead of the standard Terms & Conditions, is sent to you because no fee is being charged for your order. Please note the following:

- Permission is granted for your request in both print and electronic formats, and translations.
- If figures and/or tables were requested, they may be adapted or used in part.
- Please print this page for your records and send a copy of it to your publisher/graduate school.
- Appropriate credit for the requested material should be given as follows: "Reprinted (adapted) with permission from (COMPLETE REFERENCE CITATION). Copyright (YEAR) American Chemical Society." Insert appropriate information in place of the capitalized words.
- One-time permission is granted only for the use specified in your request. No additional uses are granted (such as derivative works or other editions). For any other uses, please submit a new request.

[BACK](#)[CLOSE WINDOW](#)